UNIVERSITY OF CALIFORNIA, SAN DIEGO

Self-adaptive methods for acoustic focusing and mode extraction in a shallow ocean waveguide

A dissertation submitted in partial satisfaction of the
requirements for the degree Doctor of Philosophy
in Physics

by

Shane C. Walker

Committee in charge:

William A. Kuperman, co-Chair
Henry D. I. Abarbanel, co-Chair
Daniel P. Arovas
William S. Hodgkiss
Barbara Jones
Philippe Roux

2005

The dissertation of Shane C. Walker is approved, and it is acceptable in quality and form for publication on microfilm:

_____

_____

_____

_____

_____

co-Chair

_____

co-Chair

University of California, San Diego

2005

To Pam

TABLE OF CONTENTS

LIST OF FIGURES

LIST OF TABLES

ACKNOWLEDGEMENTS

I wish to thank W. A. Kuperman, Philippe Roux, and Barbara Jones for their infinite patience, visionary guidance, and unwaivering support.
I wish to thank the quantum apsara whose high regard and belief in my abilities inspire me to be a better person in all facets of life.

And I wish to thank my mother for the gifts of wonder, curiosity, self-confidence, and perseverance that flow from the eternal spring of all the love in the world.

Chapters 2 through 6 of this thesis have been published, have been submitted for publication, or will be submitted for publication as listed below:

S. C. Walker, P. Roux, and W. A. Kuperman, "Data-based mode extraction with a partial water column spanning array," J. Acoust. Soc. Am. **118** (3), 1518-1525 (2005). Reprinted with permission from S. C. Walker, P. Roux, and W. A. Kuperman, "Data-based mode extraction with a partial water column spanning array," J. Acoust. Soc. Am. **118** (3), 1518-1525 (2005). Copyright 2005. Acoustical Society of America.

S. C. Walker, P. Roux, and W. A. Kuperman, "Focal depth shifting of a time reversal mirror in a range-independent waveguide," J. Acoust. Soc. Am. **118** (3), 1341-1347 (2005). Reprinted with permission from S. C. Walker, P. Roux, and W. A. Kuperman, "Focal depth shifting of a time reversal mirror in a range-independent waveguide," J. Acoust. Soc. Am. **118** (3), 1518-1525 (2005). Copyright 2005. Acoustical Society of America.

S. C. Walker, P. Roux, and W. A. Kuperman, "Mode extraction from an accelerating narrowband source in shallow water," J. Acoust. Soc. Am., submitted for publication 2005. Reprinted with permission from S. C. Walker, Philippe Roux,

and W. A. Kuperman, "Mode extraction from an accelerating narrow band source in shallow water," J. Acoust. Soc. Am., submitted for publication. Copyright 2005. Acoustical Society of America.

S. C. Walker, P. Roux, and W. A. Kuperman, "Focusing at an arbitrary waveguide location using time-reversal," J. Acoust. Soc. Am., in preparation for submission.

S. C. Walker, P. Roux, and W. A. Kuperman, "An analysis of self-adaptive mode extraction from scattered fields," J. Acoust. Soc. Am., in preparation for submission.

VITA

	Born, Miami, FL
1995	B.S. Florida Atlantic University
1997	M.S. Florida Atlantic University
2000–2003	Teaching and Research Assistant, University of California, San Diego
2003–2005	Research Assistant, Scripps Institution of Oceanography
2005	Ph.D, University of California, San Diego

PUBLICATIONS

S. C. Walker, Philippe Roux, and W. A. Kuperman, Focal depth shifting of a time reversal mirror in a range-independent waveguide, J. Acoust. Soc. Am 118 (3), 1341-1347 (2005).

S. C. Walker, Philippe Roux, and W. A. Kuperman, Focal depth shifting of a time reversal mirror in a range-independent waveguide, J. Acoust. Soc. Am 118 (3), 1518-1525 (2005).

S. C. Walker, Philippe Roux, and W. A. Kuperman, Mode extraction from an accelerating narrowband source in shallow water, J. Acoust. Soc., submitted Aug. 2005.

S. C. Walker, Philippe Roux, and W. A. Kuperman, Focusing at an arbitrary waveguide location using time-reversal, J. Acoust. Soc., in preparation.

S. C. Walker, Philippe Roux, and W. A. Kuperman, An analysis of self-adaptive mode extraction from scattered fields, J. Acoust. Soc., in preparation.

S. C. Walker, E. J Moreau, Daniel H. E. Dubin, and C. F. Driscoll, A Study of the Influence of Dynamics on Two-Dimensional Turbulent Relaxation Through Numerical Simulation, Phys. Fluids, in preparation.

S. C. Walker, and L. T. Wille, Parallel computer simulation of spatially explict epidemic models, Comp. Bio., in preparation.

FIELDS OF STUDY

Major Field: Physics

Studies in Ocean Acoustics.
Professor William A. Kuperman and Dr. Philippe Roux

Studies in Theoretical and Computational Acoustics.
Professor William A. Kuperman and Dr. Philippe Roux

Studies in Digital Signal Processing.
Professors William S. Hodgkiss, William A. Kuperman, and Philippe Roux

Studies in Marine Mammal Acoustics.
Dr. Aaron Thode

Studies in Physics Pedagogy.
Professor Barbara Jones

Studies in Nonlinear Systems.
Professor Henry D. I. Abarbanel

Studies in General Relativity and Field Theory.
Professors George M. Fuller, and Julius Kuti

Studies in Plasma Physics.
Professors Daniel H. E. Dubin, C. F. Driscoll, Thomas M. O'Neil, and Vitali Shapiro

Studies in Mathematical Methods.
Professors Raj K. Pathria and Luc T. Wille

Studies in Computational Biophysics.
Professor Luc T. Wille

ABSTRACT OF THE DISSERTATION

Self-adaptive methods for acoustic focusing and mode extraction
in a shallow ocean waveguide

by

Shane C. Walker
Doctor of Philosophy in Physics
University of California, San Diego, 2005
William A. Kuperman, co-Chair
Henry D. I. Abarbanel, co-Chair

Acoustic propagation in shallow water environments is dominated by interactions with the air/water and water/sediment interfaces, leading to complicated spatio-temporal behavior of the acoustic field. This complexity has proven challenging to the development of shallow ocean acoustic detection, communication, and tomographic applications. One approach to shallow ocean acoustics has been to combine the physics of waveguides with thorough measurement and characterization of the propagation environment to generate accurate acoustic models. However, the costs of characterizing the environment often prove prohibitive. This dissertation develops self-adaptive methods for use in shallow ocean acoustic applications that require no a-priori knowledge of the environment. In contrast to past trends that viewed the complexity of the shallow ocean as a burden, these self-adaptive techniques capitalize on the diversity of the propagation medium. Methods are developed for using vertical geometry acoustic transducer arrays to extract information from the sampled acoustic fields in a range-independent environment. In one scenario, the acoustic response sampled between a pair of arrays is iterated to generate an estimate for the response at longer ranges. In another scenario, a single array is used to extract the modes of acoustic propagation in a range-independent waveguide using

a single, partial water column spanning vertical array of acoustic transducers. The mode extraction method is applied to both an ensemble of stationary broadband sources as well as a moving narrowband source subject to arbitrary accelerations. These methods are combined with existing time-reversal techniques to produce a high resolution acoustic focus at an arbitrary location in the shallow ocean waveguide. Simulation, laboratory and at sea experiments support the theory. Though acoustic imaging applications are emphasized in this work, these methods may prove useful for both communications and tomography applications as well.

Chapter 1

Introduction

During the cold war, oceanographic research was dominated by a preoccupation with locating nuclear-capable submarines in the deep ocean. More recently, conflicts between coastal nations, both military and social, have precipitated renewed emphasis on research in the shallow ocean environment spanning the continental shelf. In particular, the rapid proliferation of computational technologies has opened the door to a wide new range of acoustic-based environmental diagnostics. Consequently, in addition to maintaining its indispensable role in submarine detection, the field of shallow ocean acoustics has assumed a new relevance and priority in areas such as communications, sea-floor mapping, mine location, tomography, and ocean biology.

Similar to a wide range of fields such as nondestructive testing, medical ultrasonics, multi-channel communications, seismic processing, adaptive optics, and radio astronomy, shallow water acoustics problems involve propagating waves that carry information to the boundaries of a minimally accessible, poorly known, complex, noisy medium where they are detected [1]. Extracting a signal from noise can be complicated, especially along a coastline filled with marine life, shipping lanes, undersea waves, shelves, and fronts that scatter sound.

In order to develop an appreciation for the challenges and opportunities posed by the shallow water acoustics, it is instructive to draw an analogy between the fields of ocean acoustics (OA) and electromagnetism (EM) applied to source detection and

communications where propagating waves transport information between a source and a receiver. Source detection applications fall under the acronyms RADAR (RAdio Detection and Ranging) and SONAR (SOund Navigation and Ranging) in EM and OA respectively.

Table 1.1 presents a list of quantities fundamental to source detection and communications in EM and OA. In both cases the working wavelengths are dictated by human scales: ships, planes, transducers, and antennae are all on the order of a meter. On the one hand, the wavelengths must be small enough to interact efficiently with the transmitting, receiving, and reflecting devices. On the other hand, longer wavelengths propagate farther than shorter wavelengths. As a result, the working wavelengths are on the order of fractions of a meter. More importantly, they are comparable in scale.

The propagation media, however, are quite different. While the EM case is mainly concerned with electromagnetic waves propagating through the rarified gas of the atmosphere, OA involves acoustic waves that propagate through salt water. The disparity between the propagation speeds of these media require vastly disparate working frequencies: GHz for EM and kHz for OA. One result of this disparity is that while EM applications are often limited to incoherent methods, both coherent and incoherent methods can be applied in OA. Furthermore, the ocean tends to exhibit markedly greater complexity than the atmosphere. Scattering and reflection from the boundaries of the shallow ocean present added challenges that must be addressed. Additionally, variations of the refractive index tend to be much more pronounced in the ocean, leading to greater refraction of the wavefronts over the working range. Transmission times are also quite different between EM and OA applications. In the EM case, the transmission time is so small that the atmosphere can always be considered static. In the OA case, dynamic macroscopic changes occur slowly enough, typically on the order of minutes to hours, that the ocean is considered to be a static medium over the transmission time, which is limited to seconds. Surface ocean waves, on the other hand, propagate quickly enough that

their effect cannot generally be considered static. Because the scale of wave amplitudes is generally small compared to the scale of the shallow ocean environment, wave effects are often treated stochastically as dynamic perturbations resulting in noise.

In any communications application, it is always important to consider bandwidth effects. The normalized bandwidth of OA applications is orders of magnitude greater than that of EM applications. Indeed, OA bandwidths can be considered extreme by EM standards. As technology has progressed, EM communications has expanded into ever more broadband regimes. With the trend toward increasingly broadband EM applications expected to continue, the ultrabroadband methods of OA may prove useful for adaptation to broadband EM applications.

Another important consideration is the Doppler shift resulting from relative motion of the source and receiver. For relative velocities small compared to the propagation speed of the medium, Doppler frequency shifts are proportional to the Mach number, v/c, where v is the relative velocity between the source and receiver, and c is the propagation velocity of the medium. Though relatively small, the acoustic Mach number characterizing OA applications is much much larger than the electromagnetic Mach number typical of EM applications. However, in OA, even small Mach numbers lead to non-negligible Doppler complications.

At frequencies and intensities characterizing ocean acoustic SONAR and communications applications, the acoustic pressure field is modeled with the linearized fluid wave equation for a static medium,

$$\left(\rho(\vec{r})\nabla\cdot\left(\frac{1}{\rho(\vec{r})}\nabla\right)-\frac{1}{c(\vec{r})}\frac{\partial^2}{\partial t^2}\right)p(\vec{r},t)=S(\vec{r},t), \tag{1.1}$$

where $S(\vec{r},t)$ represents a source term. The sound speed, $c(\vec{r})$, and density, $\rho(\vec{r})$, of the medium are considered functions of position. The boundary conditions dictate the specificity and in turn the complexity of the model.

The accuracy and effectiveness of the model depend on the degree to which the sound speed and density of the medium are known. Typically, the shallow ocean environment is treated as a waveguide; the water column is modeled as a

horizontally stratified medium bounded above by a pressure release surface and below by a high impedance, high sound speed bottom whose depth may or may not depend on range. The resulting acoustic field is complicated, comprising refracted, and reflected components. Because they are nearly incompressible, the density of the water and the various sediment layers are often considered constant. Whereas its range variation is often negligible, the sound speed in water, being a function of temperature and salinity, generally varies appreciably as a function of depth. Measuring the sound speed of the water is a relatively simple undertaking, requiring tens of temperature and salinity sensors spanning the depth of the water column. Typical shallow ocean environments of interest range in depth from 20 to 300 meters.

More difficult to measure, and even more crucial, are the geo-acoustic properties of the marine sediment. It is impractical and often impossible to comprehensively probe the sediment. The costs associated with measuring the environment sufficiently accurately to generate a useful acoustic propagation model have proven prohibitive. One alternative to measuring the environment is to optimize for it. Using this approach, measured acoustic fields are matched to a guess generated from a set of environmental parameters. However, this method is computationally limited to a small number of parameters, making it impractical for all but the simplest cases.

These limitations have motivated recent attempts to circumvent the need for environmental knowledge, either through measurement or optimization, by extracting an acoustic model directly from the measured acoustic signals themselves. This self-adaptive approach to acoustics applications derives from the premise that the acoustic field accumulates information about the medium as it propagates. Stated mathematically, as an acoustic signal propagates it is convolved by the medium though which it travels. By connecting the signal processing to the basic physics of waveguide propagation, the goal has been to develop measurement and signal processing techniques that facilitate the extraction of the environmental components from measured acoustic signals. This dissertation discusses, develops, and

expands on self-adaptive shallow ocean acoustic methods and applications to acoustic imaging. These self-adaptive techniques are directly applicable to the fields of communication, and geo-acoustic inversion.

1.1 Time-reversal in the shallow ocean

One powerful and proven self-adaptive technique is time-reversal (TR). The time symmetry of the wave equation in a static medium guarantees that for every solution, $p(\vec{r}, t)$, there exists a corresponding time conjugated solution, $p(\vec{r}, t_0 - t)$. Because the medium is reciprocal, the point-to-point acoustic field traverses the same path in either direction so that the field measured at one point due to an acoustic source at the other is the same in either direction. By sampling the field due to a spatially compact (point-like) acoustic source, termed a probe source (PS), with transducers at many points and simultaneously rebroadcasting the time-reversed signals, it is possible to reconstruct a spatially compact acoustic focus back at the probe source location. The resolution of the focus approaches the diffraction limit. It is applicable to all static environments, even those that are not azimuthally symmetric or range independent. TR has been proven in shallow ocean applications and is quite robust. Active research on TR is being conducted for detection and communications applications [2].

In the shallow ocean, reflection and refraction by the surface and sediment boundaries effectively trap high angle components of the acoustic field in the water column so that they propagate out in range. As demonstrated in Figure 1.1, reflection and refraction at the boundaries results in a multi-path structure of the acoustic field. Acoustic propagation in the shallow ocean can be thought of as arising from many image sources covering a large virtual aperture. The virtual aperture effectively samples a larger spectrum of the wavenumbers than would be sampled between sensors in free space. The increased wavenumber diversity leads to high resolution in the time-reversed field. At ranges long compared to the depth of the waveguide,

the wavenumber content of the field is limited by the critical angle criterion of total internal reflection, $cos(\theta_c) = \frac{c_w}{c_b}$, where θ_c is the critical angle, and c_w and c_b are sound speeds characterizing the water column and bottom sediment respectively. With slight modifications, the concept of an effective aperture applies more generally to environments in which the bathymetry and sound speed profile may be mildly range dependent.

Typically, shallow ocean TR applications utilize linear vertical and/or horizontal geometry transducer arrays to sample the wavenumber diversity. In the shallow ocean, a vertical line array (VLA) is useful as it samples a large cross-section of the acoustic field. Figure 1.2(a) depicts an experimental TR scenario. A VLA measures the field from the probe source. The time domain field recorded over the VLA resulting from a single broadband pulse is shown in Fig. 1.2(c). The complex temporal structure of the measured field results from the refracted and reflected components of the propagating field. Time-reversing the measured field and rebroadcasting produces an acoustic focus back at the probe source location. The focus, measured in this case by a second VLA at the source range, is displayed in Fig. 1.2(b).

The ability to focus acoustic energy at a specific location in the water column is what motivates the development of TR based applications. Because the time-reversed signal is disperse in time, it possible to achieve very high SNR gains using low intensity sources. Not only are low intensity sources more practical, their use also reduces the impact on marine mammals and other marine wildlife associated with high-intensity active SONAR. The ability to produce ensonify spatially compact regions may prove useful in both directed SONAR and communications applications. For example, a TR based SONAR system that has the ability to selectively scan for targets would drastically reduce the effects of acoustic clutter. As a communications application, the high resolution of TR could permit different messages, encoded in the TR field, to be focused, with high SNR, simultaneously to different locations of an underwater antenna, thereby increasing the data transfer rate.

For all of their promise, current TR applications suffer from one major limitation: the need for a probe source to broadcast from the desired focal spot. This requirement limits TR in the shallow ocean to highly controlled experimental applications. The self-adaptive techniques developed in this dissertation, though applicable to areas other than TR, have at their heart and as their main motivation, the aim of expanding the situations to which TR can be applied.

1.2 Normal mode description of the acoustic field

To establish a foundation for the development of self-adaptive methods, an acoustic model is introduced. The theory is restricted to the case of linear phenomena under the assumption of a static environment, so that linear wave equation in the form of Eq. (1.1) defines the cannon. The static environment assumption does not impose much of a restriction considering the disparity between the relevant time scales. Whereas changes in oceanographic quantities, such as the sound speed and density, occur on the order of several minutes to several hours, because of the high value of the sound speed in water, acoustic propagation covers distances of kilometers in a matter of a few seconds.

The theory is further restricted to the case of horizontally stratified propagation media in which the sound speed and density are independent of range. By limiting the scope to range-independent media, substantial analytic progress can be made resulting in a model which predicts emergent range-invariant properties that motivate the development of the self-adaptive techniques that are the subject of this dissertation. The obvious disadvantage is that range-dependent phenomena cannot be modeled with this approach. Oceanographic observations show that the temperature distribution, and hence the sound speed profile, of the shallow ocean tend to be horizontally stratified, often remaining stable over many kilometers. Because of the strong impedance mismatch at the water bottom interface, the assumption of range-independence of the depth of the interface is much more critical. In sit-

uations where the working range is much greater than the nominal depth of the interface, the reflected components of the acoustic field assume added significance. A particular component may experience many interactions with the interface over the working range. The interface is well approximated as range-independent when the variation of the interface depth over the working range is small compared to the acoustic wavelength.

The following theoretical development is based on the normal mode derivation presented in Chapter 5 of Ref. [3]. Though it considers the point-to-point acoustic field between a single acoustic point source and a single receiver located in the water column, the results are easily extended to collections of stationary point sources and receivers. The added time component associated with a moving source complicates matters considerably and is treated in Chapter 5. The prevailing geometry of point sources and receivers in a horizontally stratified environment is most conveniently addressed in cylindrical coordinates as azimuthal symmetry can be invoked to reduce the analysis to 2 coordinates: range, r, and depth, z. Writing Eq. (1.1) for a point source at (r_s, z_s) in cylindrical coordinates

$$\frac{1}{r}\frac{\partial}{\partial r}\left(r\frac{\partial p}{\partial r}\right)+\rho(z)\frac{\partial}{\partial z}\left(\frac{1}{\rho(z)}\frac{\partial p}{\partial z}\right)-\frac{1}{c^2(z)}\frac{\partial^2 p}{\partial t^2}=-\frac{\delta(r-r_s)\delta(z-z_s)}{2\pi(r-r_s)}S(t). \quad (1.2)$$

Applying the Fourier transform pair,

$$\begin{aligned}\widetilde{f}(\omega) &= \frac{1}{2\pi}\int_{-\infty}^{\infty} f(t)e^{-i\omega t}dt, \quad (1.3)\\ f(t) &= \int_{-\infty}^{\infty}\widetilde{f}(\omega)e^{i\omega t}d\omega,\end{aligned}$$

where $f(t)$ is an arbitrary function of time and its tranform, $\widetilde{f}(\omega)$, is a function of angular frequency, yields the Helmholtz equation in cylindrical coordinates,

$$\frac{1}{r}\frac{\partial}{\partial r}\left(r\frac{\partial \widetilde{p}}{\partial r}\right)+\rho(z)\frac{\partial}{\partial z}\left(\frac{1}{\rho(z)}\frac{\partial \widetilde{p}}{\partial z}\right)+k^2(z)\widetilde{p}=-\frac{\delta(r-r_s)\delta(z-z_s)}{2\pi(r-r_s)}\widetilde{S}(\omega). \quad (1.4)$$

$k(z)\equiv\frac{\omega}{c(z)}$ is the magnitude of the acoustic wavenumber at depth z. Because it has invoked transform (1.3), the solution of Eq. (1.4) is only rigorously valid at a single frequency. Therefore, the resulting acoustic model is implicitely narrow band.

Assuming a solution for the pressure field of the form $\widetilde{p} = \chi(r)\phi(z)$ and using the separation of variables technique yields

$$\frac{1}{\chi(r)}\left(\frac{1}{r}\frac{\partial}{\partial r}\left(r\frac{\partial\chi(r)}{\partial r}\right)\right) + \frac{1}{\phi(z)}\left(\rho(z)\frac{\partial}{\partial z}\left(\frac{1}{\rho(z)}\frac{\partial\phi(z)}{\partial z}\right) + k^2(z)\phi(z)\right) = -\frac{\delta(r-r_s)\delta(z-z_s)}{2\pi(r-r_s)}\widetilde{S}(\omega). \tag{1.5}$$

Defining k_r as the separation constant, the solution to the associated homogenous equation is given by the following pair of equations,

$$\rho(z)\frac{\partial}{\partial z}\left(\frac{1}{\rho(z)}\frac{\partial\phi(z)}{\partial z}\right) + \left(k^2(z) - k_r^2\right)\phi(z) = 0, \tag{1.6}$$

$$\frac{1}{r}\frac{\partial}{\partial r}\left(r\frac{\partial\chi(r)}{\partial r}\right) + k_r^2\chi(r) = 0. \tag{1.7}$$

Eq. (1.6) is called the modal equation because it yields a discrete set of depth dependent orthogonal mode functions. For the special cases of impenetrable boundaries, i.e. pressure release at the surface interface and either a pressure release (zero impedance) or rigid (infinite impedance) bottom, the modal equation reduces to a classical Sturm-Liouville eigenvalue problem. In this case the solutions form a complete set of orthogonal eigenfunctions associated with a discrete set of real, nondegenerate eigenvalues. The eigenvalues have the dimensions of wavenumber and represent the radial component of the wavenumber of the pressure field. Each eigenfunction and its associated eigenvalue characterize an acoustic mode. Physically, propagation at a discrete set of specific angles with respect to the air/water and water/bottom interface surfaces results in constructive interference among the reflected components. Propagation angles which support standing waves in the vertical direction with respect to the boundaries lead to constructive interference phenomena with an associated set of radial wavenumbers. These interference phenomena are the modes. Each mode, then, has an associated propagation angle and is characterized a vertical amplitude dependence (eigenfunction) and an associated radial wavenumber (eigenvalue).

Impenetrable boundaries, however, are an idealization that may or may not be a good approximation to the physical ocean. Due to the extreme impedance mismatch at the air-water interface, the ocean surface is well modeled as an impenetrable boundary. The impedance mismatch at the water-sediment interface, on the other hand, though large, is generally not so drastic that it can be modeled as an impenetrable surface. In the case of a penetrable bottom, Eq. (1.6) may have solutions over a continuum of complex eigenvalues in addition to the set of discrete, nondegenerate, real eigenvalues pertaining to the modal solutions. In this case, the wavenumber spectrum of the eigenvalues comprises a continuous region and a discrete region. As the sound speed profile characterizing typical marine sediments is everywhere greater than the maximum sound speed of the water column, the continuous region of the spectrum is significant for $k_r < \frac{\omega}{c_{bmin}}$ where c_{bmin} is the minimum sound speed characterizing the marine sediment. The discrete region of the wavenumber spectrum falls in the range $\frac{\omega}{c_{bmin}} \lessapprox k_r < \frac{\omega}{c_{wmin}}$ where c_{wmin} is the minimum sound speed characterizing the water column. The solutions associated with the discrete region of eigenvalues form an incomplete set of orthogonal eigenfunctions. The discrete set of eigenvalues and their associated eigenfunctions, labeled k_n and $\phi_n(z)$ ($\{n = 1, 2, \ldots, N\}$) respectively, define the modes of acoustic propagation. As in the impenetrable boundary case, the discrete set of modes result from constructive interference at a discrete set of angles. The labels are applied such that $k_1 > k_2 \cdots > k_N$. This ordering results in eigenfunction $\phi_n(z)$ having $m - 1$ zero crossings. The modes are normalized such that

$$\int_0^\infty \frac{\phi_n^2(z)dz}{\rho(z)} = 1. \tag{1.8}$$

Figure 1.3 shows a schematic representation of the modal components. As the top panel demonstrates the, the modes are characterized by a discrete set of propagation angles between the horizontal and a critical angle, $\theta_c \approx \arccos(c_{wmin}/c_{bmin})$. Field components propagating at angles steeper than the critical angle are partially transmitted into the sediment. The bottom panel shows the modal depth dependence. The modes are characteristically oscillatory in the water column and decay

exponentially in the sediment. Also indicated are the wavenumbers associated with each mode.

Returning to the inhomogenous problem, the full solution for the pressure field can be written as a discrete sum over the modal solutions and an integration over the continuum solutions, $\widetilde{p} = \sum_{m=1}^{N} \chi_n(r)\phi_n(z) + \int_{continuum}$. The continuum dominates the near-field and becomes insignificant in the far field. Neglecting the continuum, the pressure field at (r, z) due to an acoustic point source at (r_s, z_s) is written in the far-field limit

$$\widetilde{p}(R, z, \omega) \simeq \frac{e^{\frac{-i\pi}{4}}}{8\pi\rho(z_s)} \sum_{n=1}^{M} \phi_n(z, \omega)\phi_n(z_s, \omega) \frac{e^{-ik_n(\omega)R}}{\sqrt{k_n(\omega)R}} \widetilde{S}(\omega), \tag{1.9}$$

where $R \equiv |r_s - r|$ is the absolute range separation. The frequency dependence has been made explicit to facilitate the broadband considerations,

$$p(R, z, t - t_0) = \int_{-\infty}^{\infty} \widetilde{p}(R, z, \omega) e^{i\omega(t-t_0)} d\omega. \tag{1.10}$$

Whereas in the narrowband limit the time domain acoustic field can be thought of as a superposition of modal components that are spatially and temporally unlocalized, in broadband applications, modal propagation manifests as a superposition of spatio-temporally localized modal group components. Over a finite bandwidth, constructive interference about a given propagation angle results in a spatially localized coherent modal group of acoustic energy that propagates dispersively at a constant velocity (the group velocity, v_g). The full time domain pressure field due to a broadband point source can be conceptualized as a synthesis of modal group components. Indeed, modal groups are observed experimentally. For limited bandwidth, the modal depth dependence is nearly constant so that the narrowband modal depth dependence at the carrier frequency of the source signal, $\phi_n(z, \omega_c)$ (ω_c is the source signal carrier frequency) is well approximated by the depth dependence of the corresponding modal group. Figure 1.4(a) shows a simulated example of finite bandwidth modal propagation. Depicted is the envelope of the sampled time domain field due a finite bandwidth point-source at a given range from the VLA. The depth dependencies of the modal groups are evident. Notice both the intermodal and intramodal

dispersion increase with mode number. Figure 1.4(b) shows an example of typical modal group and phase velocity behavior as a function of frequency.

Revisiting TR focusing in a range-independent waveguide, the expected resolution of the focal spot can be elegantly estimated using normal mode theory. Figure 1.5 illustrates the physical basis underlying the focal resolution. Shown are schematic representations of modal propagation both into the VLA (top panel) and the TR field modal propagation away from the VLA (bottom panel). The vertical extent of the source signal and the resulting focal spot are depicted on the right. The spatial resolution of the focal spot depends on the number of modes arriving back at the source location. The loss of the near-field contributions along with the range attenuation of the propagating modes result in a reduction in resolution of the focal spot compared to the initial source resolution. The depth and range extents of the focal spot are approximately given by $\Delta_z \approx D/N$ and $\Delta_R \approx 2\pi/(k_1 - k_N)$ respectively.

Thus from normal mode analysis under the assumption of range-independence of the propagation medium emerges a set of robust, measurable field quantities that offer the potential for the development of self-adaptive techniques for modeling the acoustic field. This approach is particularly powerful in regimes supporting a small number of modes where the acoustic field can be synthesized from a relatively small number of modal components.

1.3 Applying self-adaptive acoustic modeling to matched field signal processing

Modal based self-adaptive techniques provide opportunities for improving the effectiveness of acoustic matched field signal processing applications. Matched field processing (MFP) [4] encompasses a class of signal processing methods wherein a measured acoustic field is matched to an acoustic model generated from a set of parameters. Typically, the model is a function of one to many parameters that

characterize the propagation medium and boundary conditions. A realization of a particular parameter combination is called an acoustic replica. Fitting the measured field to the acoustic model as a function of the input parameters (one point for each replica) yields an M-dimensional ambiguity function where M is the number of input parameters. The parameter realization that minimizes the ambiguity defines the optimal replica.

There are numerous methods for generating acoustic replicas. Ray methods [5, 6, 7] and parabolic equation (PE) methods [8, 9, 10] are commonly used. Ray methods based on the Eikonal equation [11] are valid in the high frequency limit. PE methods based on the parabolic equation [12, 13] are valid in the far field limit under the paraxial approximation. Both are numerical forward, or integration, methods. That is they are numerical methods that proceed from a set of initial conditions to a final configuration. Typically the initial conditions are a guess of the target location at a given time and the final configuration is the replica field on an array of sensors. Both methods require extensive characterization of the propagation medium to produce accurate results. Accurate modeling of an environment as complex as the shallow ocean generally requires a large number of parameters. This combined with the computational load imposed by the integration implementation makes simultaneous inversion for the source location and environmental parameters computationally prohibitive. As a result, traditional model based MFP has proven ineffectual for large dimensionality problems. MFP has met with limited success in shallow ocean applications where most of the environmental inputs are known a-priori and treated as constants so that the dimensionality of the problem can be drastically reduced.

While ray and PE methods may be the alternatives for generating replica fields for range dependent propagation media, modal modeling provides an attractive alternative for replica generation in range independent environments. Because modal theory is founded on an analytic basis, it does not incur the computational cost associated with the numerical integrations of the ray and PE methods. As shown in Sec. 1.2, accurate characterization of the modal components requires a knowledge of

the sound speed and density profiles in the water column and the bottom sediment. Realistic profiles are generally sufficiently complex as to require a large number of environmental inputs. As with the ray and PE methods, the computational cost associated with generating an accurate multi-dimensional ambiguity function limits the applicability of mode-based MFP to shallow ocean applications where most of the environmental inputs are known a-priori. Thus, when applied in the traditional manner, ray-based, PE-based, and mode-based MFP require extensive measurement of the propagation media to determine as many of the a-priori model parameters as possible. As mentioned, directly measuring the environment, the sediment in particular, is very expensive and often not possible.

However, the self-adaptive methods developed in this work present a promising opportunity for accurate mode-based MFP replica generation in range-independent propagation media without the need for extensive environmental measurement. In fact, the self-adaptive methods can be applied to the same collection of sensors used to measure the matching field. As previously discussed, range-independence of the media leads to the emergence of a tractable number of robust, experimentally measurable modal field components. Each component individually is manifestly consistent with the propagation medium, however complicated it may be. By combining signal processing with the physics of modal propagation to extract the modal components, it is possible to generate a self consistent ensemble of replica fields as a function of initial conditions alone, i.e. source depth and range.

Self-adaptive techniques may also find applications in tomography. For example, application of self-adaptive methods to matched mode processing (MMP) techniques may lead to improved bottom parameter inversion. MMP is a variation on traditional MFP where the connection between the propagation medium and/or the source location proceeds entirely through modal analysis [15, 16]. It is possible to extract information about the propagation medium by making a comparison of the the measured modal components to a modal model. Typically, the analysis is rendered tractable by assuming a knowledge of the sound speed profile of the water

column and solving for a simplified bottom model (perhaps 4 parameters).

This thesis introduces self-adaptive methods for manipulating TR imaging without any a-priori knowledge of the shallow ocean environment under the assumption of range-independence. In Chapter 2, a method is introduced for producing TR foci at arbitrary locations (of both range and depth) using the frequency response sampled between a pair of vertical arrays. The method is based on an iterative method analagous to Huygens principle. Chapters 3 and 5 address self-adaptive mode extraction. As discussed, an accurate knowledge of the modes provides opportunities for TR, MFP, and tomography. Though recently introduced methods for extracting the modal depth functions over a full-spanning VLA (one that covers the entire water column) have shown promise, difficulties associated with deploying full-spanning VLAs make them difficult to implement. Chapter 3 develops a method for extracting the modal depth functions over a partial spanning VLA. The technique requires from stationary broadband sources distributed in range. In Chapter 5 a similar method is applied to extract the modes from a moving narrowband source. The method is particularly relevant to at sea applications because it incorporates a technique for self-adaptively compensating for Doppler effects caused by arbitrary accelerations. Chapter 4 applies a knowledge of the extracted modal depth functions to the task of shifting the TR focus in depth from the original source location. Finally Chapter 6 presents an analysis of the prospects for extracting modes self-adaptively from the acoustic field scattered from features along water/sediment interface.

The following chapters present results from experiments conducted under controlled conditions in a laboratory waveguide. For reference, Appendix A describes in detail the experimental set up used in these experiments. In addition, the connection is made between the laboratory set up and at sea applications.

Bibliography

[1] William A. Kuperman and James F. Lynch, "Shallow Water Ocean Acoustics," Physics Today, pp. 55-61, October 2004.

[2] W. A. Kuperman, W. S. Hodgkiss, and H. C. Song, "Phase-conjugation in the ocean: Experimental demonstration of an acoustic time-reversal mirror," J. Acoust. Soc. Am **103**, 25-40 (1998).

[3] F. B. Jensen, W. A. Kuperman, M. B. Porter, and H. Schmidt, *Computational Ocean Acoustics*, (AIP New York, 1994).

[4] Arthur B. Baggeroer, W. A. Kuperman, and Peter Mikhalevsky, "An overview of matched field methods in ocean acoustics", IEEE J. of Oceanic Engineering, **1** (4) 401-424, 1993.

[5] V. Cervený, "Ray tracing algorithms in three-dimensional laterally varying layered structures," in *Seismic Tomography*, edited by G. Nolet (Reidel, Boston, MA, 1987).

[6] V. Cervený, M. M. Popov, and I. Psencik, "Computation of wave fields in inhomogeneous media - Gaussian beam approach," Geophys. J. R. Astr. Soc. **70** 109-128 (1982).

[7] M. B. Porter, and H. P. Bucker, "Gaussian beam tracing for computing ocean acoustic fields," J. Acoust. Soc. Am. **82**, 1349-1359 (1987).

[8] D. Lee and S. T. McDaniel, *Ocean Acoustic Propagation by FInite Difference Methods* (Pergamon, New York, 1988).

[9] J. S. Perkins and R. N. Baer, "An approximation to the three-dimensional parabolic equation method for acoustic propagation," J. Acoust. Soc. Am. **72**, 515-522 (1982).

[10] W. L. Siegmann, G. A. Kriegsmann, and D. Lee, "A wide-angle three-dimensional parabolic wave equation," J. Acoust. Soc. Am. **78**, 659-664 (1985).

[11] J. B. Bleistein, *Mathematical Methods for Wave Phenomena* (Academic, Orlando, FL, 1984).

[12] M. A. Leontovich and V. A. Fock, Zh. Eksp. Teor. Fiz. *16* 557-573 (1946) [Engl. transl.: J. Phys. USSR *10* 13-24 (1946)].

[13] F. D. Tappert, "The parabolic approximation method," in *Wave Propagation in Underwater Acoustics*, edited by J. B. Keller and J. S. Papadakis (Springer-Verlag, New York, 1977) pp 224-287.

[14] P. Hursky, W. S. Hodgkiss, and W. A. Kuperman, "Matched field processing with data-derived modes," J. Acoust. Soc. Am. **109** (4), 1355-1366 (2001).

[15] E. C. Shang, "Source depth estimation in waveguides," J. Acoust. Soc. Am. **77**, 1413-1418 (1985).

[16] T. C. Yang, "A method of range and depth estimation by modal decomposition," J. Acoust. Soc. Am. **82** (5), 1736-1745 (1987).

Quantity	Electromagnetism (EM)	Ocean acoustics (OA)
Wavelength (λ)	0.3 m	0.5 m
Propagation speed (c)	3×10^6 km/s	1.5 km/s
Carrier frequency (f_c)	10^9 Hz	3×10^3 Hz
Working range (R)	100 km	10 km
Round trip time ($2R/c$)	6.6×10^{-4} s	13.3 s
Bandwidth (Δf)	10^6 Hz	10^3 Hz
Normalized ($\Delta f / f_c$) bandwidth	0.001 (narrowband)	0.33 (ultrabroadband)
Source speed (v)	100 m/s	10 m/s
Mach number (v/c)	3×10^{-7}	7×10^{-3}

Table 1.1: Comparison of physical quantities characterizing electromagnetic RADAR and communications applications versus ocean acoustic SONAR and communications applications.

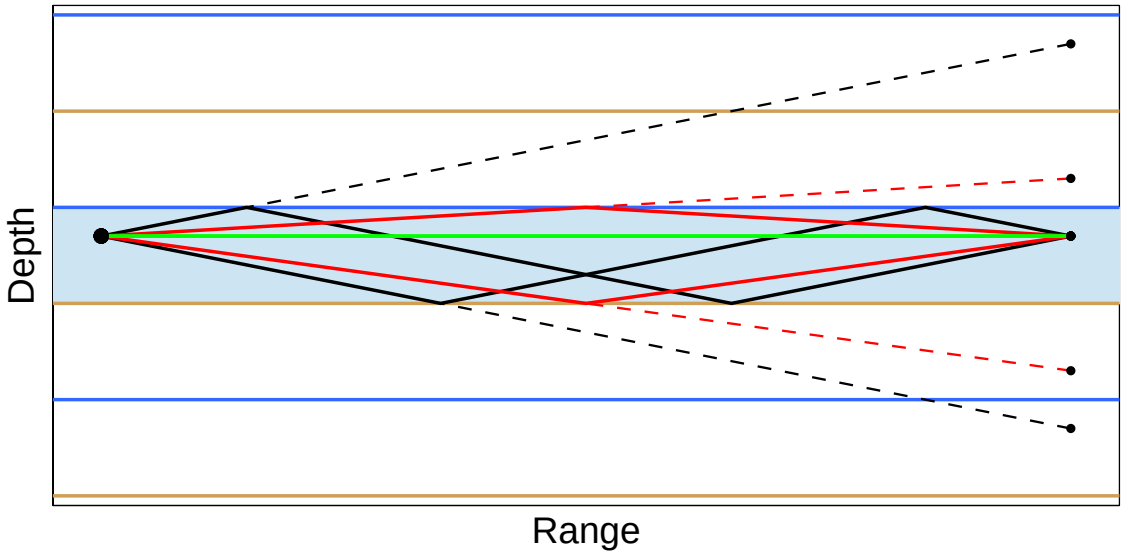

Figure 1.1: Virtual aperture of a shallow ocean waveguide. Multi-path propagation due to reflection at the boundaries of the waveguide result in virtual acoustic image sources. The vertical extent of the virtual images comprises a large virtual aperture. Solid lines indicate multi-path within the waveguide. Dashed lines indicate the free path to the corresponding virtual images. The shaded region represents the waveguide.

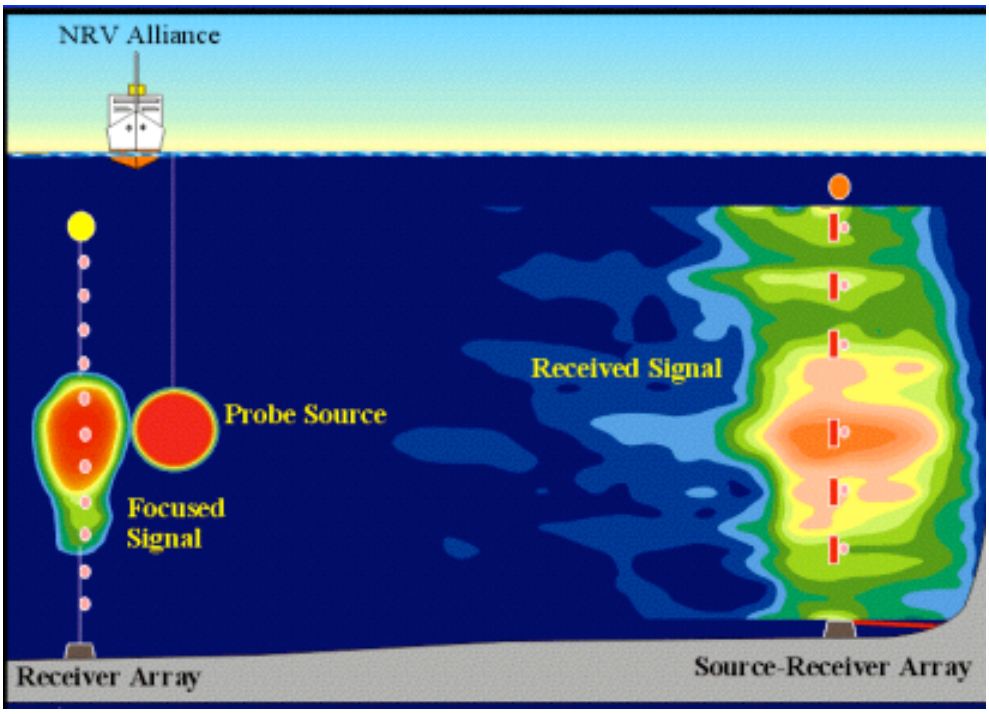
NRV Alliance
Probe Source
Focused
Signal
Received Signal
Receiver Array
Source-Receiver Array

(a)

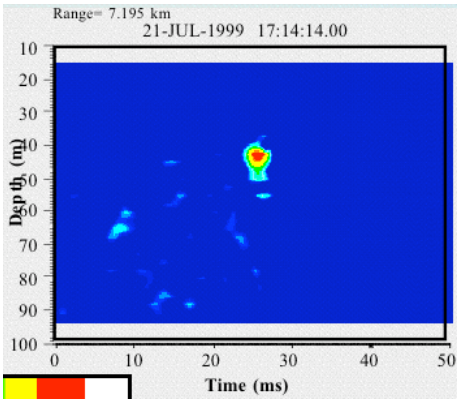
Range= 7.195 km
21-JUL-1999 17:14:14.00
Depth (m)
Time (ms)

(b)

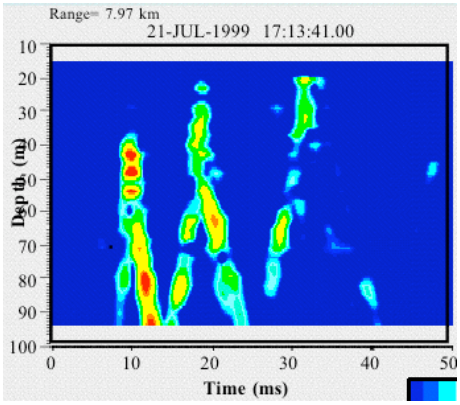
Range= 7.97 km
21-JUL-1999 17:13:41.00
Depth (m)
Time (ms)

(c)

Figure 1.2: Schematic of TR in the shallow ocean. Shown in (a) is a typical experimental scenario. The field due to a point source is sampled by, time-reversed and rebroadcast by a VLA (indicated as dashes above Source-Receiver Array title) resulting in an acoustic focus back at the probe source location. The TR focus is measured with another VLA (indicated by dots above Receiver Array title). Panel (b) shows an example of an experimentally measured time domain field sampled over the Source-Receive Array while panel (c) shows the resulting experimental TR focus measured at the Receiver Array. Panels (b) and (c) show the envelopes of the respective time domain fields.

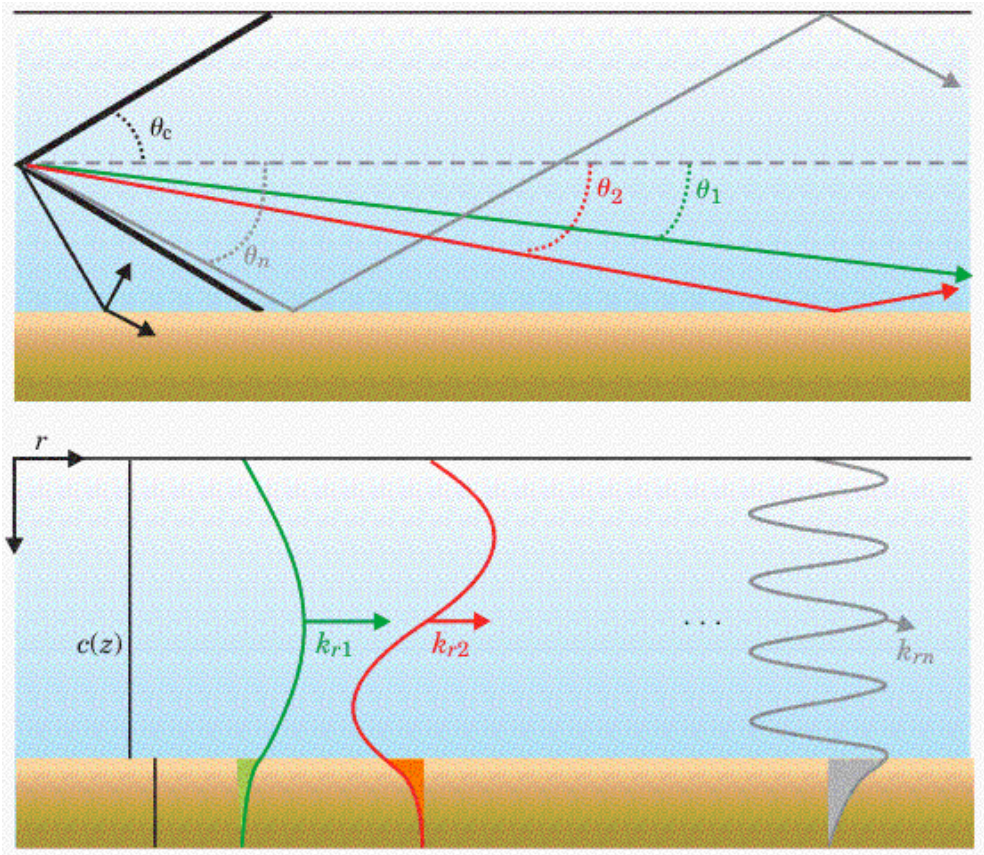

Figure 1.3: Schematic representation of the relation between modal propagation and the modal depth functions. The top panel shows the discrete set of modal propagation angles. The modal angles are all less than the critical angle, θ_c, of total internal reflection at the water/sediment interface, $\theta_1, \theta_2, \ldots, \theta_n < \theta_c$. The bottom panel displays the modal depth functions typical of shallow ocean propagation. The modes are characteristically oscillatory in the water column and decay exponentially in the sediment. The wavenumbers associated with each mode, $k_{r1}, k_{r2}, \ldots, k_{rn}$, are represented by arrows. The sound speed profile for this example is depicted by $c(z)$. In both panels, the light shaded region is the water and the dark shaded region is the sediment.

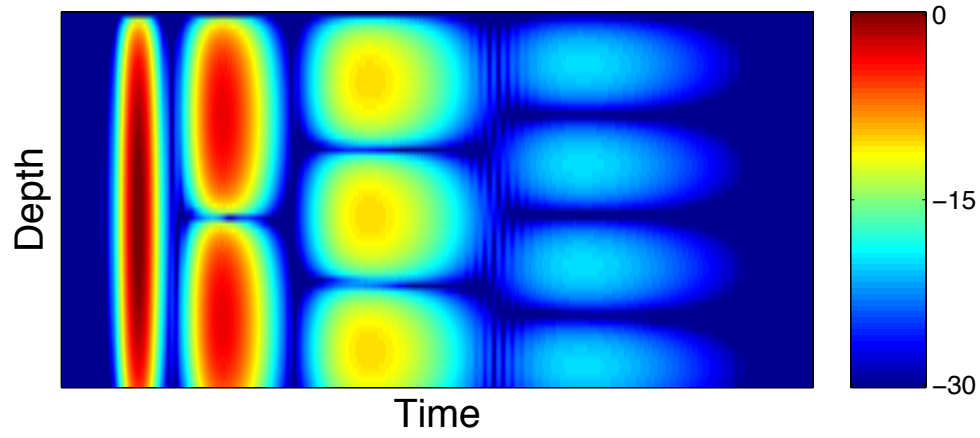

(a)

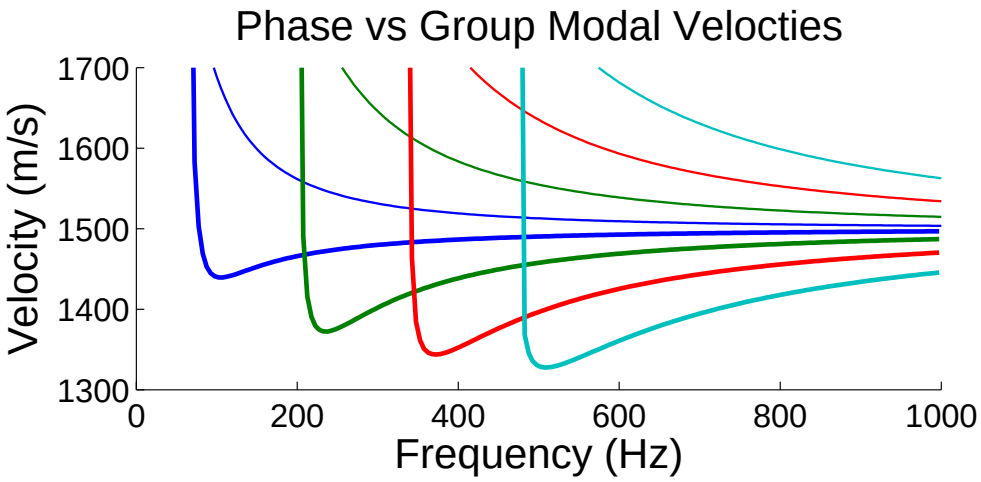

(b)

Figure 1.4: Simulated finite bandwidth modal propagation. Panel (a) depicts is the envelope of the sampled time domain field due a finite bandwidth point-source at a given range from the VLA. Panel (b) shows an example of typical modal group and phase velocity behavior as a function of frequency.

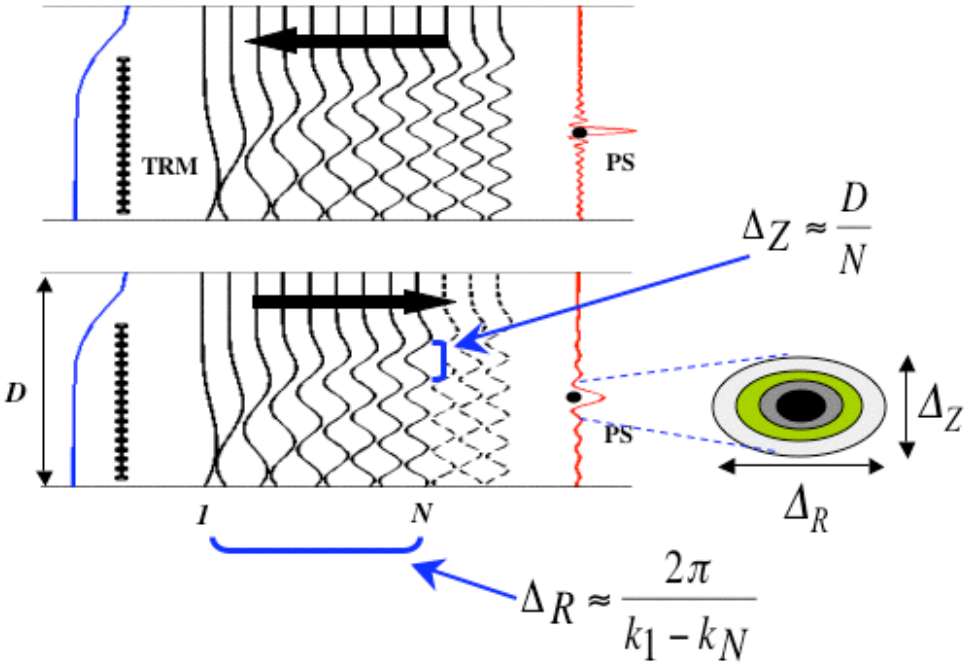

Figure 1.5: Schematic of TR focal resolution. The top panel shows a schematic representation of modal propagation from the source to the VLA (dark broken line indicated as TRM). The modal depth functions are depicted as black curves, one for each mode. The modes are ordered from lowest to highest left to right. The vertical extent of the source field is indicated on the right. The curve to the left of the VLA indicates the sound speed profile. The bottom panel depicts time-reversed propagation from the VLA to the source location. The dashed curves indicate modes that are attenuated from the signal. The vertical extent of the TR focus is indicated on the right. Δ_R and Δ_z are the range and vertical extents of the focal spot respectively. The focal resolution is a function of the number of modes, N, composing the acoustic field reaching the source location.

Chapter 2

Focusing at an arbitrary waveguide location using time-reversal

abstract

Recent experiments have demonstrated the ability of time-reversal (TR) methods to selectively ensonify spatially compact regions of the water column in shallow ocean environments [1]. The major limitation of current TR methods is that they require an acoustic probe source at the desired focal location. This work introduces a method for using a pair of vertical line transducer arrays (VLAs) to produce TR foci at any location in a range-independent shallow ocean waveguide without the need for a probe source. Modal theory suggests that the acoustic response sampled between a pair of VLAs separated by a range R can be repeatedly iterated to estimate the acoustic response at ranges that are integer multiples of R. The process results in a virtual sampling of the acoustic response over long distances that can applied to both passive and active shallow ocean acoustic imaging applications. Array geometry effects are explored and theoretical and experimental results are presented.

2.1 Introduction

The evolution of technology and computation has opened new avenues of research in underwater target acquisition and communications. Contrary to the traditional view that reverberation from the surface and sediment boundaries of the shallow ocean are a nuisance to be minimized, advances in recent research have suggested that reverberation from complex propagation media can be exploited to improve the performance of sonar and communications applications. In particular, recent experiments have demonstrated the ability of time-reversal (TR) methods to selectively ensonify spatially compact regions of the water column in shallow ocean environments [1]. Such high resolution acoustic focusing capabilities could have a direct impact on active and passive sonar and communications applications as well as matched field processing techniques [2, 3]. The major limitation of current TR methods is that they require an acoustic probe source at the desired focal location. This work discusses a method for using a pair of vertical line transducer arrays (VLAs) to produce TR foci at distant ranges at any depth in the water column without the need for a probe source.

By Green's theorem, the acoustic response over a closed surface completely determines the response throughout the enclosed volume. In an experimental context, a dense sampling of the point-to-point acoustic response between a pair of vertical transducer arrays separated in range, can be used to uniquely determine the response throughout the intervening volume. In the special case of a horizontally stratified range-independent propagation medium, the point-to-point acoustic response is independent of absolute range, depending only the source and receiver depths and on their relative range separation (throughout the remainder of this paper, the relative range separation between the VLAs is referred to as the iteration-range). Modal theory suggests that the point-to-point acoustic response between a pair of VLAs can be iterated to estimate the acoustic response at integer multiples of the iteration-range. According to Huygens principle, the response on one array due

to the other can be decomposed into wavelets that govern the phase evolution of the field over the iteration-range. In a range-independent medium, iterating the response function is equivalent to evolving the response phase over integer multiples of the iteration-range. The iterated response estimates can be used to generate a TR focus at integer multiples of the iteration-range at any sampled depth. The iteration process is applied as a cross-convolution of measured fields summed over the array elements. As the convolution is a multiplicative process, repeated iteration can lead to undesirable frequency spectrum modulation effects in the time-reversed signal which must be considered. Applying the theory of acoustic field invariants in a range-independent waveguide [4], the iteration process, termed sampled response iteration (SRI), can be combined with variable range time-reversal [5] to extend the method to intervening ranges, i.e. non-integral multiples of the iteration-range.

Section 2.2 presents a development of the theory of the iteration method and accompanying simulation results. The experimental set up is described in Sec. 2.2.1 followed in Sec. 2.2.2 by a brief outline of the theory of time-reversal in a range-independent waveguide. A treatment of the basic theory of the iteration method is given in Sec. 2.2.2. The theoretical discussion addresses bandwidth equalization and array geometry effects. In Sec. 2.2.2 the iteration method is extended to the entire waveguide in combination with variable range TR. Results from ultrasonic experiments in a laboratory are presented in Sec. 2.3. Section 2.4 gives a summary and concluding remarks.

2.2 Theory and simulation of the sampled response iteration procedure

2.2.1 Experimental set up

The experimental geometry for which the SRI procedure is designed is schematically represented in Fig. 2.1. A pair of parallel, vertical geometry transducer element

arrays, labeled V^α and V^β, are located a distance R apart. R is defined to be the iteration-range. A cylindrical coordinate system is chosen such that V^α defines the axis of azimuthal progression at $r = 0$. Because SRI is only rigorously applicable to range-independent media, analysis is restricted to situations where the vertical plane passing through V^α and V^β is horizontally stratified, i.e. characterized by constant bathymetry and sound speed profile as a function of range. It is assumed that any azimuthal dependence in the vicinity of the plane is sufficiently small that acoustic refraction and reflection into and out of the plane is negligible.

The point-to-point acoustic response, sampled between all transducer elements of the array pair, is iterated to generate response function estimates at successive intervals of the iteration-range. The net result is that the point-to-point response is virtually sampled in range with R as the range sampling interval. The gray dots of Fig. 2.1 represent points at which the field is virtually sampled. By applying a frequency shift to the iterated fields, it is possible to extend the virtual sampling to intervening ranges. For the purposes of time-reversal, the set of virtual samples represents an ensemble of fields from virtual sources. Time-reversal (phase conjugation) and transmission of a chosen virtual source field results in an acoustic focus at the location of the virtual source. In order to simplify the analysis, the arrays are always labeled such that V^α corresponds to the transmission array. As seen in Fig. 2.1, a third array, labeled V^γ, is used to sample the resulting TR field.

2.2.2 Theoretical discussion

This section begins with an analytical summary of the basics of time-reversal in a range-independent propagation medium. The discussion then progresses to a development of the theoretical aspects of the range iteration method. Array geometry and bandwidth effects are addressed. Finally, the SRI method is combined with the variable range TR method of Ref. [5]. The theoretical analysis is supplemented with simulation results. For simplicity, the analysis is carried out for an azimuthally symmetric medium.

Time-reversal in a range-independent propagation medium

For the purposes of this discussion it is convenient to write the acoustic pressure field in terms of the frequency response between the transducer elements composing the vertical sensor arrays V^α and V^β. The elements of the respective arrays are labeled by the indices a and b respectively. The a^{th} element of array V^α is at depth $z = z_a$ and likewise for V^β. The arrays are separated by a distance R with V^α at $r = 0$ and V^β at $r = R$. Array V^α comprises a total of A elements while array V^β comprises B elements. The ω angular frequency component of the pressure response is then written

$$\widetilde{P}_{ab}(R,\omega) = \widetilde{G}_{ab}(R,\omega)\widetilde{S}(\omega), \tag{2.1}$$

where $\widetilde{G}_{ab}(R,\omega)$ denotes the ω component of the acoustic response between elements a and b and $\widetilde{S}(\omega)$ represents the ω component of the Fourier decomposition of the time domain source signal. The Fourier transform pair is defined

$$\begin{aligned} \widetilde{F}(\omega) &= \frac{1}{2\pi}\int_{-\infty}^{\infty} F(t)e^{-i\omega t}dt, \\ F(t) &= \int_{-\infty}^{\infty} \widetilde{F}(\omega)e^{i\omega t}d\omega. \end{aligned} \tag{2.2}$$

Equation (2.1) is an array specific projection, or discrete sampling, of the acoustic field. In its more general, continuous form, Eq. (2.1) is written without subscripts as a function of continuous varibles,

$$\widetilde{P}(r,z,z',\omega) = \widetilde{G}(r,z,z'\omega)\widetilde{S}(\omega). \tag{2.3}$$

The two forms of the acoustic response will be employed interchangeably depending on the context of the discussion. For the remainder of the paper, any appearance of subscripts is to be interpreted as an array specific projection, with a or any variation thereof always referring to the elements of V^α and any variants of b referring to V^β.

According to the Helmholtz equation, the ω component of the acoustic response can be written as a superposition of modal components that are orthogonal over depth,

$$\widetilde{G}_{ab}(R,\omega) = \frac{e^{-i\frac{\pi}{4}}}{\rho(z_b)\sqrt{8\pi R}}\sum_{m=1}^{M}\frac{\phi_m(z_a,\omega)\phi_m(z_b,\omega)}{\sqrt{k_m(\omega)}}e^{-ik_m(\omega)R}. \tag{2.4}$$

The normal mode functions, $\phi_m(z,\omega)$, and their associated modal wavenumbers, $k_m(\omega)$ (also referred to as propagating wavenumbers), are solutions to the modal eigenvalue equation (at each value of ω),

$$\left[\frac{d^2}{dz^2} + \left(\left(\frac{\omega}{c(z)}\right)^2 - k_m^2(\omega)\right)\right]\phi_m(z,\omega) = 0, \tag{2.5}$$

for horizontally stratified media (no r dependence) and appropriate boundary conditions [6]. In general, the normal modes comprise only a subset of the range of solutions to Eq. 2.5 corresponding to real eigenvalue solutions. Depending on the boundary conditions, there may be a continuum of complex eigenvalue solutions. The normal modes solutions become evanescent in the sediment so that they are confined to the water column. Because they do not propagate into the sediment, the normal modes are weakly attenuated and may travel, or propagate, long distances in the water column. The continuum of complex eigenvalue solutions of Eq. (2.5), on the other hand, are oscillatory in the sediment and correspond components of the acoustic field that strongly attenuated with range. Because the aim is to model long range behavior, the attenuated components are neglected in Equation (2.4).

For convenience the following pair of equations are introduced,

$$\sum_{m=1}^{M} \frac{\phi_m(z,\omega)\phi_m(z',\omega)}{\rho(z')} = \mathcal{C}_M(z,\omega) \tag{2.6}$$

$$\int_{z_1}^{z_2} \frac{\phi_m(z,\omega)\phi_n(z,\omega)}{\rho(z)} dz = \mathcal{L}_{mn}(z_1,z_2). \tag{2.7}$$

Equation (2.6) is a generalization of the statement of closure relating the modes. Equation (2.6) becomes a strict statement of closure and completeness in the limit that the number of propagating modes approaches infinity,

$$\lim_{M\to\infty} \mathcal{C}_M(z,\omega) \to \delta(z-z'). \tag{2.8}$$

Neglecting the continuum of highly attenuated solutions and near field components of the field guarantees that closure will only be approximate. The number of propagating modes is a function of the frequency and the medium. As a general rule,

M increases as both the depth of the water/sediment boundary and the frequency increase.

Equation (2.7) is a generalization of the orthogonality conditions relating the modes. This generalization is useful as a tool for describing array geometries that do not sample the entire span of the modes. Identifying the limits of integration, z_1 and z_2, with the depths of the shallowest and deepest elements, respectively, of a linear geometry array, the right hand side of Eq. (2.7) becomes a Kroneker delta function when the integration limits span the entire space over which the modes exist,

$$\lim_{z_1 \to 0, z_2 \to \infty} \mathcal{L}_{mn}(z_1, z_2) \to \delta_{mn}. \tag{2.9}$$

In the realistic case of a finite impedance sediment layer (or layers), the modes penetrate into the sediment making it impossible to completely sample the modes with a water bound array. However, because the modal amplitudes decay exponentially with depth in the sediment layer, orthogonality can be achieved to high accuracy over the interval $\{z_1 = 0, z_2 = D\}$ where D is defined to be the depth of the water/sediment boundary. An array that spans the entire water column is referred to as full-spanning.

To apply time-reversal focusing, the pressure field from an acoustic point source at the location (r', z') is first sampled by the elements of array V^α. $\widetilde{P}_a(r', z', \omega)$ represents the pressure response sampled over the array. Time-reversal in the time domain is applied as phase conjugation in the frequency domain. Propagating the phase conjugated sampled field through the medium is described by the following sum over the elements of V^α,

$$\begin{aligned}
\widetilde{P}^{TR}(r, z, \omega) &= \sum_{a=1}^{A} \widetilde{G}_a(r, z, \omega) \widetilde{P}_a^*(r', z', \omega) \\
&= \sum_{a=1}^{A} \widetilde{G}_a(r, z, \omega) \widetilde{G}_a^*(r', z', \omega) \widetilde{S}^*(\omega) \qquad (2.10) \\
&\approx \frac{\widetilde{S}^*(\omega)}{8\pi\rho(z')\sqrt{rr'}} \sum_{m=1}^{M} \left(\frac{\phi_m(z, \omega)\phi_m(z', \omega)}{k_m(\omega)} \right) e^{-ik_m(\omega)(r-r')}.
\end{aligned}$$

The hybridization of the discrete and continuous notation among the various quantities of Eqs. (2.10) results from a combination of Eqs. (2.1) and (2.3). In order to arrive at this expression, the response function, $\widetilde{G}_a(r, z, \omega)$, must be reciprocal in the coordinate r. As well, the discretized form of the modal orthogonality relation of Eq. (2.7) is invoked in summing over the elements of the array. This is valid in the limit that the array densely samples most of the water column. Orthogonality can be applied to every mode for which the array geometry samples the mode at 2 points per period (in depth) over the entire effective span of the mode. Typically, an array sampling interval equal to or less than half the characteristic acoustic wavelength of the water column is sufficient to adequately sample all the modes.

For all ranges $r \neq r'$, most or all of the modes are out of phase and interfere more or less destructively. At $r = r'$ however, all the modes arrive in phase. Applying the closure relation of Eq. (2.6) leads to a focusing of the time-reversed pressure field at the source depth,

$$\widetilde{P}^{TR}(r', z, \omega) \approx \frac{\widetilde{S}^*(\omega)\delta(z - z')}{8\pi\rho(z')\sqrt{rr'}} \tag{2.11}$$

In light of the discussion of Equations (2.6)-(2.9), obviously the focal resolution is not infinite as predicted by Eq. (2.11). It has been shown that the resolution of the focus in both range and depth depends directly on the number of propagating modes, increasing with M [1]. Array geometry plays an important role as well. Though full-spanning densely-sampling arrays yield the best results, good results have been achieved with less than full-spanning arrays that sample at intervals greater than half the acoustic wavelength. The high order modal components of the field most affected by under sampling are also the most attenuated with range, thereby reducing the impact of the resulting aliasing of under-sampled high order modal components. Of course, range dependent attenuation also reduces the resolution of the TR focus. Overall, TR has proven to be robust [1].

Sampled response iteration

As outlined in the last section, time-reversal in the time domain is applied as phase conjugation in the frequency domain. Introduction of another factor of the acoustic response and summation over the array elements defines the propagation operation. In the case of a full-spanning array that densely samples the modes, summation over the array elements introduces an essential simplification; specifically mode orthogonality suppresses phase coupling between the modal components. Analagously, applying the propagation operation to the unconjugated field and invoking the range reciprocity of the response and orthogonality of the modes results in a virtual propagation of the field further down range. To demonstrate this, we define the ω component of the virtually propagated field, $\widetilde{P}^{VP}(\omega)$, and apply the propagation operation,

$$\begin{aligned}
\widetilde{P}^{VP}(\omega) &= \sum_{a=1}^{A} \widetilde{G}_a(r,z,\omega)\widetilde{G}_a(r',z',\omega)\widetilde{S}(\omega) \\
&\approx \frac{e^{-i\pi/2}\widetilde{S}(\omega)}{8\pi\rho(z')\sqrt{rr'}} \sum_{m=1}^{M} \left(\frac{\phi_m(z,\omega)\phi_m(z',\omega)}{k_m(\omega)} \right) e^{-ik_m(\omega)(r+r')} \\
&\approx \frac{e^{-i\pi/4}\widetilde{S}(\omega)}{\sqrt{8\pi}} \sqrt{\frac{r+r'}{rr'}} \widetilde{G}(r+r',z,z',\omega) \\
&\approx \left(\sqrt{\frac{r+r'}{8\pi rr'}} e^{-i\pi/4} \right) \widetilde{P}(r+r',z,z',\omega).
\end{aligned} \tag{2.12}$$

In proceeding from the second line above to the third line, a factor of $\frac{1}{\sqrt{k_m(\omega)}}$ has been neglected for each modal component. For the present, this is justified by the argument that the modal wavenumbers typically don't differ significantly, so the error in the relative modal modulation is negligible. For example, under realistic shallow ocean conditions, the modal wavenumbers differ at most by a factor of 2 between the highest and lowest order modes. Most importantly, the operation has preserved the relative phases of the modal components. Thus, except for a cylindrical spreading error, the virtual propagation result closely approximates the

frequency response between the array and a source at range $r + r'$. The procedure has propagated the field an additional range increment, r'. Like time-reversal, this exercise has potential for application to the shallow ocean waveguide.

We return to the case of sampling the acoustic pressure, $\widetilde{P}_{ab}(R,\omega)$, between the array pair, V^α/V^β. Noting that the point-to-point acoustic response function is embedded in the sampled pressure in the field, it is possible to construct the virtual propagation operation in terms of the sampled field. Choosing element b' of array V^β as the source, virtual propagation using the sampled pressure field yields,

$$\begin{aligned}
\widetilde{P}^{VP}_{bb'}(\omega) &= \sum_{a=1}^{A} \widetilde{P}_{ab}(R,\omega)\widetilde{P}_{ab'}(R,\omega) \\
&= \sum_{a=1}^{A} \widetilde{G}_{ab}(R,\omega)\widetilde{G}_{ab'}(R,\omega)\widetilde{S}^2(\omega) \qquad (2.13)\\
&\approx e^{-i\pi/4}\widetilde{S}(\omega)\left(\sqrt{\frac{1}{4\pi R}}\right)\widetilde{P}_{bb'}(2R,\omega).
\end{aligned}$$

Ignoring for the moment the practical considerations involved with deploying a pair of parallel, full-spanning, densely-sampling arrays, this result is compelling because it implies that the field can be virtually sampled over long ranges without any knowledge of the environment by simply iterating this procedure. In order to demonstrate this, it is convenient to identify the indexed quantities as matrices and vectors:

$$\begin{aligned}
\widetilde{\mathbf{P}}^{\mathbf{VP}}_{\omega} &\equiv [\widetilde{P}^{VP}_{ab}], \\
\widetilde{\mathbf{P}}_{\omega} &\equiv [\widetilde{P}_{ab}(R,\omega)], \qquad (2.14)\\
\widetilde{\mathbf{G}}_{\omega} &\equiv [\widetilde{G}_{ab}(R,\omega)], \\
\phi_{\mathbf{m}}(\omega) &\equiv [\phi_m(z_a,\omega)].
\end{aligned}$$

For simplicity, the explicit dependence on R is suppressed.

In order to be as general as possible, the iteration method is developed for the case of arrays comprised of differing numbers of elements ($A \neq B$) in which case $\widetilde{\mathbf{P}}_{\omega}$ is not a square matrix. As a practical issue, it is likely not desirable to deploy

a pair of identical fixed arrays, but rather to have one fixed array at $r = 0$ (V^α) and a second more mobile and easily deployable array at $r = R$ (V^β) with the fixed array designated as the array from which all TR signal shall ultimately originate. To facilitate time-reversal from V^α, the iteration is applied so that the virtually sampled field $\widetilde{\mathbf{P}}_\omega^{\mathbf{VP}}$ always has A components. The following algorithm facilitates such an implementation. The iterated virtually propagated field is given as

$$\left(\widetilde{\mathbf{P}}_\omega^{\mathbf{VP}}\right)^N \equiv \mathbf{Q}_\omega^{\mathbf{N}}\mathbf{Q}_\omega^{\mathbf{0}}, \tag{2.15}$$

where N is the number of applied iterations and $\mathbf{Q}_\omega^{\mathbf{N}}$ is defined to be the matrix inner product

$$\mathbf{Q}_\omega^{\mathbf{N}} \equiv \left[\prod_{n=1}^{N} \mathbf{T}_\omega^{(-\mathbf{1^n})}(\mathbf{\Gamma}_\omega)\right]. \tag{2.16}$$

Here $\mathbf{T}$ is a transpose operation that operates on its argument such that

$$\mathbf{T}_\omega^{-\mathbf{1}}(\mathbf{\Gamma}_\omega) = \mathbf{\Gamma}_\omega^{\mathbf{T}}, \quad \mathbf{T}_\omega^{\mathbf{1}}(\mathbf{\Gamma}_\omega) = \mathbf{\Gamma}_\omega.$$

The starter field, $\mathbf{Q}_\omega^{\mathbf{0}}$, is defined

$$\mathbf{Q}_\omega^{\mathbf{0}} = \begin{cases} [\widetilde{P}_{a'b}(\omega)]^T & N = \{1,3,5,\dots\} \\ [\widetilde{P}_{ab'}(\omega)] & N = \{2,4,6,\dots\}, \end{cases} \tag{2.17}$$

where a' and b' denote the virtual source depth on V^α or V^β respectively, depending on which array is appropriate. Similarly $\mathbf{\Gamma}_\omega$ is chosen such that

$$\mathbf{\Gamma}_\omega = \begin{cases} A(\omega)\widetilde{\mathbf{P}}_\omega & N = \{1,3,5,\dots\} \\ A(\omega)\widetilde{\mathbf{P}}_\omega^{\mathbf{T}} & N = \{2,4,6,\dots\}. \end{cases} \tag{2.18}$$

Equation (2.19) has been generalized to include a normalization factor, $A(\omega)$ whose meaning will become clear shortly. At this point it is instructive to consider an example. Using Eqs. (2.15)-(2.19) to explicitly expand the iteration algorithm for $N = 2$ yields

$$\begin{aligned} \left(\widetilde{\mathbf{P}}_\omega^{\mathbf{VP}}\right)^2 &= \mathbf{Q}_\omega^{\mathbf{2}}\mathbf{Q}_\omega^{\mathbf{0}} \\ &= A^2(\omega)\left(\widetilde{S}(\omega)\right)^2\left[\widetilde{\mathbf{G}}_\omega\widetilde{\mathbf{G}}_\omega^{\mathbf{T}}\right][\widetilde{P}_{ab'}(\omega)] \\ &\approx A^2(\omega)\left(\widetilde{S}(\omega)\sqrt{\frac{1}{4\pi R}}\right)^2\left[\widetilde{P}_{ab'}(3R,\omega)\right]. \end{aligned} \tag{2.19}$$

The process is shown schematically in Fig. 2.2. As with Eqs. (2.12) and (2.13), a factor of $\frac{1}{\sqrt{k_m(\omega)}}$ has been neglected for each modal component in writing the third line above. This is justified in the case of multiple iterations due to the presence of modal attenuation in any realistic waveguide. With each iteration the effect of the cylindrical spreading error, through the $\frac{1}{\sqrt{k_m(\omega)R}}$ factor, is counteracted by the effect of the exponential decrease resulting from modal attenuation. The net result is that with each iteration the high order modes tend to attenuate more strongly than the low order modes.

Bandwidth equalization

Because the source signal is embedded in the sampled pressure field, any structure in the frequency power spectrum will tend to compound with each iteration. For example, consider a sampled pressure response resulting from a source signal characterized by a Gaussian distribution of its frequency content (as results from a Gaussian modulated time domain pulse). The frequency spectrum of the resulting virtually sampled field will narrow with each iteration leading to a significant loss of bandwidth after just a few iterations. Figure 2.3 shows a schematic of the effects of such a narrowing for 8 iterations. Assuming the source signal is known, such a loss of bandwidth can be overcome by defining the normalization constant of Eqs. (2.19) in accordance with the source signal spectrum,

$$A(\omega) = \frac{\sqrt{4\pi R}}{|\widetilde{S}(\omega)|}. \tag{2.20}$$

Including the term in the numerator, this frequency equalization scheme simultaneously compensates for the cylindrical spreading. However, due to the term in the denominator, this equalization scheme may prove problematic for the case of a complicated source signal spectra that approaches zero within the bandwidth.

Array geometry effects

How well the iteratively generated virtual sampled field can be expected to approximate the true pressure response depends sensitively on array geometry. Errors

introduced through insufficient array sampling compound with each iteration. It has already been shown that for a full-spanning, densely-sampling array (one for which Eq. (2.9) holds true), iteration results in an accurate approximation of the true pressure response at an equivalent range, particularly with respect to the phase. This is verified in Fig. 2.4. As the goal is to perform TR focusing, Fig. 2.4 shows a simulated comparison of TR focusing between a simulated iteration result and the standard modal model for the case of full-spanning, densely-sampling arrays. The top panel shows the spatial component of the time-reversed virtual pressure field resulting from 8 iterations of the simulated pressure field between the array pair. Eight iterations of the iteration-range, $R = 500\ m$, corresponds to a virtual source at 4.5 km. The simulation is for a narrowband source at a depth of 45 m. The lower panel shows the TR focus over the same range achieved using the standard modal model for a true source at the same location. Even after 8 iterations, there is good agreement between the results. It is noted here that all simulation results presented in this paper are carried out for identical simulated Pekeris waveguide propagation media for which the modal components are calculated using the KRAKEN mode model including modal attenuation [7]. The water depth is 100 m, with bottom parameters of sound speed and density given by $c_b = 1800\ \frac{m}{s}$ and $\rho_b = 1800\ \frac{kg}{m^3}$ respectively.

Due to the difficulties and impracticalities associated with the deployment of full-spanning, densely-sampling arrays, particularly in the case of deep water, high frequency applications, it is relevant to consider the effects of other array geometries on the iteration procedure. The effects of array geometry on straightforward TR focusing in an ocean waveguide have been demonstrated [1]. Namely, under-sampling in depth, both in terms of the sampling interval and the total aperture, leads to reduced focal resolution performance. Because the effects of under-sampling compound with each iteration, TR imaging using the iterated virtually sampled fields is even more sensitive to array geometry. There are three elements of array geometry that affect the imaging performance of the SRI method in different ways; total

array aperture, array depth sampling rate, and array tilt. Each element is considered separately in order to isolate their individual effects. We consider the cases of (1) partial-spanning, densely-sampling arrays, (2) full-spanning, sparsely-sampling arrays, and (3) full-spanning, densely sampling tilted arrays.

Figure 2.5 shows a comparison of simulated time domain fields for various array geometries. The fields correspond to 8 iterations of the SRI method for a virtual broadband source at 4.5 km. All iterated simulation results are frequency equalized in accordance with the normalization introduced in Eqs. (2.19) and (2.20) in order to suppress iterative bandwidth effects. As a benchmark for comparison, the modal model result is displayed in Figure 2.5(a). That is, the field in Fig. 2.5(a) is the field from a true source, sampled over a full-spanning, densely-sampling array, to which the iteration results should be compared. The iteration result for a pair of full-spanning, densely-sampling arrays shown in Fig. 2.5(b) is in good agreement with the true field, particularly with respect to the low order modal components (the early arrivals). In accordance with the increasing difference in propagating wavenumber among the higher order modes, the relative weightings of the high order modal components (late arrivals) are more sensitive to the extra factor of $\frac{1}{\sqrt{k_m(\omega)}}$. Compounding this error over many iterations has resulted in the slight, but observable, difference among the high order modal components of the iterated field as compared to the benchmark. This effect is moderated by the inclusion attenuation in the simulation. Without range dependent attenuation, the error resulting from the extra factor of $\frac{1}{\sqrt{k_m(\omega)}}$ would lead to severe over excitation of the high order modes after many iterations.

The time domain TR results for the iterated full-spanning, densely-sampling case, shown in Fig. 2.6(b), are also in good agreement with the benchmark TR result of Fig. 2.6(a). To clarify, time-reversal is applied by multiplying the phase conjugated iterated (or benchmark) field by the modal model response from a given range. All time domain TR results consist of 3 panels. Each panel is to be regarded as the time domain pressure field measured over a receive array (V^{γ} of Fig.2.1) at

the specified range. The center panel corresponds to the expected focal range.

The case of partial-spanning, densely-sampling arrays is addressed in Fig. 2.5(c) and Fig. 2.6(c). Figure 2.5(c) shows the time domain virtually sampled pressure field after 8 iterations generated using a 90% spanning array for V^{α} and an 80% spanning array for V^{β}. Deviation from the benchmark result (Fig. 2.5(a)) is apparent over all modal components. This result is expected as partial coverage of the water column results in deviations from orthogonality between all modal components. The resulting TR field in Fig. 2.6(c) exhibits significant degradation of the temporal resolution.

In the case of full-spanning, sparsely-sampling arrays, it is possible that orthogonality may exist differentially among the modal components. While the low order modes may be well sampled in depth and be orthogonal, the high order modes may not. Figure 2.5(d) shows the compounded effects arising from iterating a sparsely sampled field. The sampling interval of both arrays is equivalent to the wavelength at the carrier frequency, $dz = 5\ m$. While there is good agreement between the low order modal components in comparison to the benchmark, there is an obvious deviation between the high order modal components. The TR result of Fig. 2.6(d) displays the characteristic aliasing errors associated with under-sampling. One solution for dealing with under-sampling errors is to clean the high order components from the signal prior to time-reversal. Due to the temporal dispersion of the modes, as shown in Fig. 2.5(e), the high order components are easily isolated and removed in the time domain. As demonstrated in Fig. 2.6(e), cleaning the sparsely-sampled signal results in a significant improvement in TR focal resolution.

The final aspect of array geometry considered is array tilt. It has been demonstrated that array tilt has no performance effect on straightforward TR imaging. In contrast, even small deviations from perpendicularity among the arrays turn out to have a drastic effect on the SRI method. The appearance of the transpose operation in the iteration method implicitly assumes reciprocity of the sampled point-to-point pressure response between the arrays. However, tilt on either or both of the arrays

destroys the reciprocity of the sampled pressure response. Because tilt results in phase differences, even a small tilt can prove disastrous after only a few iterations.

Array tilt is typically remedied by utilizing the measured mutual range offset among the array elements to apply a plane wave time delay, $\Delta t_{a/b}$, to the elements,

$$\widetilde{P}_{ab}(R,\omega) \rightarrow \widetilde{P}_{ab}(R,\omega)e^{i\omega(\Delta t_a + \Delta t_b)}. \tag{2.21}$$

Denoting as Δr_a (Δr_b) the measured range offset of element a (b) with respect to a given reference element, the time delay compensation on element a (b) is given as $\Delta t_a = \frac{\Delta r_a}{c_s}$ ($\Delta t_b = \frac{\Delta r_b}{c_s}$) where c_s is a sound speed characterizing acoustic propagation in the waveguide. Applied in this manner, this form for the time delay can be thought of as an angular beam form operation. Because the arrival angles of the low order modes are more densely packed than those of the higher order modes, choosing an angle from among the low order modes (or equivalently choosing a sound speed from among the group speeds of the lowest modes) results in the best compensation for the greatest number of modes. Additionally, due to attenuation, high order modal contributions tend to be less significant because they carry less energy. As a result, though the choice for c_s is somewhat arbitrary, it is advantageous to choose it to be among the group speeds of the lowest order modes. To good approximation the mode 1 group speed can be estimated by the sound speed of the water column. If the sound speed varies with depth, it is useful to average the sound speed over depth. If nothing is known about the sound speed profile, as is the case in the experimental results presented in the next section, a good guess should suffice.

Array tilt simulation results are presented in Figs. 2.5(f) and 2.6(f). While array V^{α} remains vertical, the initial tilt profile of array V^{β} is depicted in Fig. 2.7. This profile exhibits a realistic curvature that might result from strong currents along the ocean bottom. As well, the tilt profile is rather severe, having a maximum element range offset of nearly 10 m, or 2 acoustic wavelengths. Iterating the sampled field in this geometry quickly leads to large errors and is not shown. However, applying the tilt compensation method outlined above (for $c_s = 1500\ \frac{m}{s}$) to the sampled field under the assumption that the relative array positions (Δr_b) are perfectly known

leads to the result shown in Fig 2.5(f). As expected, there is good agreement between the low order modal components of the iterated and benchmark fields with small, but observable, accumulated errors appearing among the higher order modal components. The time-reversal result is seen in Fig. 2.6(f). To make the analysis more realistic, applying a random uncertainty between -30 cm and 30 cm to each element range offset (of the tilted array) leads to little observable difference in the iterated time-reversed field (not shown), indicating that small random deviations from perpendicularity are tolerable.

Combining SRI with variable range TR

It is known that the interference structure of a shallow ocean waveguide exhibits a regular pattern of striations of the acoustic intensity as a function of frequency and range, $I(\omega, r)$ [4, 8, 9]. The striations, resulting from interference among a group of modal components, are characterized by invariant slope β,

$$\beta \equiv \frac{r}{\omega}\left(\frac{\Delta\omega}{\Delta r}\right) = -\frac{d(1/v_\phi)}{d(1/v_g)}, \tag{2.22}$$

where v_ϕ and v_g represent average phase and group velocities characterizing the group of modes contributing to the observed interference pattern of the waveguide. The invariant β, then, is a function of the physical properties of the propagation medium itself, independent of source and receiver locations and the source signal. In Ref. [5] the theory of acoustic field invariants is applied to TR imaging as a method for shifting the TR focus in range from the initial source location. As demonstrated, time-reversing the frequency domain acoustic field sampled on a vertical array from an acoustic point source at range r_0 to which a frequency shift, $\Delta\omega$, has been applied leads to a range shift of the TR focus,

$$r' \approx r_0\left(1 + \frac{1}{\beta}\frac{\Delta\omega}{\omega}\right), \tag{2.23}$$

where r' denotes the range shifted focal range. Due to the frequency dependence of the depth dependent amplitudes of the modal components of the acoustic field,

the focal resolution of variable range TR is expected to degrade for large absolute values of the fractional frequency shift, $|\Delta\omega/\omega|$. Empirical evidence suggests that variable range TR focusing is effective for fractional frequency shifts in the range $-0.1 < \Delta\omega/\omega < 0.1$.

Applying variable range TR to the virtually sampled iterated field, it is possible to extend the TR focusing capability of the SRI technique to include all points of the waveguide. Recall that iteration of the sampled point-to-point acoustic pressure response leads to an ensemble of virtual sources at integer multiples of the iteration-range. Placing a conservative restriction on the fractional frequency shift of the carrier frequency, $|\Delta\omega/\omega|_{max} = 0.05$, it is possible to generate a high resolution TR focus at all ranges and depths of the waveguide after 8 iterations of the sampled field (assuming $\beta \approx 1$). This can be seen by substituting $|\Delta\omega/\omega|_{max} = 0.05$ and $\beta = 1$ into Eq. (2.23) for positive and negative range shifts of ranges corresponding to 8 and 9 iterations respectively,

$$9R(1 + 0.05) \approx 10R(0.95).$$

The imaging capability of variable range TR applied to SRI is schematically presented in Fig. 2.8. The diagram has been generalized to the case of arrays of differing geometry. Using the iterated virtually sampled field alone, TR foci can be generated at the ensemble of points indicated by the open and closed circles. The open and closed circles correspond to the array element depths of V^{α} and V^{β} respectively. Notice the points span the array depths at multiple integer intervals of the iteration-range. Combining SRI with variable range TR, TR focusing is possible at all ranges within the shaded regions within the depth spans of the corresponding arrays.

Figure 2.9 shows a simulated variable range TR result for the case of full-spanning, densely-sampling arrays. The top panel shows the spatial component of the time-reversed virtual pressure field resulting from 8 iterations. A +5% fractional frequency shift has been applied resulting in a positive range shift of the TR focus. For the purposes of comparison, the variable range TR iteration result is

accompanied by the the variable range TR result for the standard modal model for the same range and fractional frequency shift (bottom panel). The initial range of the source in both cases (virtual source in the former and real source in the latter) is 4.5 km. The expected range shift indicated in the figures, $\Delta r = 225\ m$, is for an ideal waveguide, $\beta = 1$. However, the actual range shift of the TR focus is about $\Delta r \approx 350\ m$, indicating that $\beta < 1$ for this waveguide. This is indeed the case for the simulated Pekeris waveguide. Figure 2.10 shows the time domain range shifted TR focus corresponding to the simulation of Fig. 2.10. The resolution of the iterated result (Fig. 2.9(a)) is comparable to the standard model benchmark result (Fig. 2.10(b)).

2.3 Experimental results

This section presents results of an experimental study of the SRI method. The experiment was conducted under controlled laboratory conditions in a small scale range-independent waveguide at ultrasonic frequencies. As illustrated in Fig. 2.1, the point-to-point acoustic response sampled between a pair of VLAs, V^{α} and V^{β}, separated by iteration-range R, was iterated to generate a virtual sampling of the point-to-point response at successive integer multiples of the iteration-range. The virtually sampled response was then applied to TR imaging with the aim of generating TR foci at the virtually sampled points. A third VLA, V^{γ}, was positioned down range to measure the time-reversed fields.

2.3.1 Set up

The experiment was designed to model the shallow ocean at small scales. The waveguide comprised well mixed fresh water over a uniform steel bottom maintained at a constant depth over the extent of the waveguide. The working length of the waveguide, was roughly a meter. In order to far-field scaling of working length to water depth, $R/D \gg 1$, the steel bottom was maintained at a depth of $D =$

26.5 mm. All point-to-point pressure response measurements were sampled using a $\Delta f = 1.5\ MHz$ bandwidth Gaussian modulated signal at carrier frequency of $f_c = 1.5\ MHz$. Hence, the acoustic wavelength, λ_w, characterizing propagation in the water was $\lambda_w \approx 1\ mm$.

Each VLA, V^α and V^β, consisted of 50 evenly spaced linearly arranged transducer elements spanning 24.5 mm. The element spacing was 0.5 mm ($\approx \lambda_w/2$). Due to the small scale of the set up, it was not possible to determine the array tilt a-priori. Rather the tilt was deduced from the performance of the TR results. It was determined that a tilt of 0° for V_α and 0.5° for V_α yielded the optimal TR imaging performance. It is emphasized that the optimization for array tilt is a by-product of the small experimental dimensions. At the larger scales characterizing shallow ocean applications, the tilt is directly measurable. The iteration-range separating the VLAs were separated by a distance $R = 82.8\ mm$. The VLA used to measure the TR fields, V^γ has similar geometry to V^α.

2.3.2 Results

Figure 2.11 shows the measured SRI TR foci generated from several virtually sampled fields. Panels (a) and (b) are the fields for 2 different virtual source depths at a range of $r = 5R = 414\ mm$ corresponding to 4 iterations of the sampled response function. In each case, The dashed lines indicate the expected focal depths. For comparison, the measured TR focus due to a real source at the same range, $r = 414\ mm$, is included in panel (c). Similarly, panels (d) and (e) show SRI TR focus results due to virtual sources at $r = 10R = 828\ mm$ (9 iterations). Again, the measured TR focus due to a real source at the same range is presented in panel (f) for comparison. The experimental SRI TR result in panel (g) resulted from application of the iteration procedure without accounting for array tilt. The tilt was relatively small, accounting for a total maximum absolute inter-element range displacement of $|\Delta r_b|_{max} = .2\ mm \approx \lambda_w/5$. After 9 iterations, however, even such a small tilt results in a significant degradation of imaging performance.

Figures 2.12(a) and 2.12(b) present a comparison of the time domain pressure fields used to generate the TR focus results of Figs. 2.11(e) and 2.11(f), respectively. In comparison with the direct sampled field due to a real source shown in panel (b), the iteration procedure has resulted in an observable attenuation of the late arrivals of the virtual field shown in panel (a). The attenuation of the high order modal components increases with each iteration, resulting in a cumulative reduction in the imaging resolution. Noting that the temporal extent of the TR foci remained constant over many iterations, it is encouraging that the frequency equalization scheme of the iteration procedure resulted no iterative bandwidth loss. In experimental applications, it is important to consider the frequency response of the transducer devices. As it is embedded in the sampled point-to-point pressure response, the transducer response will be propagated with each iteration[10]. Ideally, it should be measured and accounted for in the equalization scheme.

Similar experimental results were achieved at all depths spanned by the VLAs out to 9 iterations. The experiment could not be continued beyond 9 iterations due to the limitations imposed by the working range of the experimental waveguide. Judging from the results, it is conceivable that doing so would have yielded favorable results out to at least a few more iterations. It is noted that 8 iterations are sufficient to cover all ranges in conjunction with the variable range TR method of Ref. [5] assuming a conservative 5% range shift maximum. The experimental design did not allow for combination with variable range, however.

2.4 Summary and discussion

A method for using a pair of vertical transducer arrays to ensonify a spatially compact region at any location of a shallow ocean waveguide has been presented. The method is fully self-adaptive, requiring no a-priori knowledge of the environment other than that the medium is nearly range-independent. Denoting the initial sampling range separating the arrays as the iteration-range, the sampled point-to-

point acoustic pressure response between the arrays can be multiply iterated to generate accurate estimates of the point-to-point acoustic response projected over the arrays at integer multiples of the iteration-range. The procedure results in a virtually sampled acoustic field that can be time-reversed to produce high intensity, high resolution acoustic focusing at any of the virtually sampled locations. The method has been combined with the variable range time-reversal (TR) technique proposed by H. C. Song *et. al.* [5] to demonstrate the potential to produce TR foci at ranges other than the virtually sampled ranges.

As the process is iterative, array geometry effects assume great importance. Any deficiencies in the sampling geometry of the arrays compound with each iteration. The method has proven effective over many iterations for full water column spanning geometries, even in the case of sparse intra-array sampling. In the case that one or both of the arrays are partially spanning, the effectiveness of the iteration procedure is limited to fewer iterations, with the limit depending on the extent of the array coverage. Of particular importance is the issue of array tilt. For the iteration procedure to be effective, array tilt must be compensated for, requiring that the arrays be equipped with tilt measurement devices. So long as the arrays can be rendered vertical on average, small uncertainties in tilt compensation are tolerable. The method is proven effective experimentally under controlled laboratory conditions out to 9 iterations.

Because the iteration invokes range invariance, the analysis presented in this paper has been limited to range-independent applications. However, there is reason to suspect that the method may be extendable to weakly range dependent environments, suggesting a possible avenue of future study. The sampled range iteration (SRI) method has potential as both a passive and active sonar application. As a passive sonar application, SRI is a natural candidate for matched field signal processing (MFP) methods. As demonstrated by [11], cross-correlation of the ambient noise acoustic field over the array elements leads to the array pressure response between the elements. The signal from any source, then, could be cross-correlated

and iterated to determine the source location. As an active sonar application, the demonstrated ability of SRI, when combined with time-reversal, to ensonify spatially compact regions of the shallow ocean make an it a promising candidate for directed sonar. Additionally, as as it is a method for generating a large virtual range aperture, the iteration method may prove useful as a mode extraction application. Of particular interest is the potential for extracting the lowest order modes requiring the greatest range aperture.

2.5 Acknowledgements

This chapter, in full, will be submitted for publication with authors S. C. Walker, Philippe Roux, and W. A. Kuperman.

Bibliography

[1] W. A. Kuperman, W. S. Hodgkiss, and H. C. Song, "Phase-conjugation in the ocean: Experimental demonstration of an acoustic time-reversal mirror," J. Acoust. Soc. Am **103**, 25-40 (1998).

[2] S. N. Wolf, D. K. Cooper, and B. J. Orchard, "Environmentally adaptive signal processing in shallow water," Oceans '93, Engineering in Harmony with Ocean Proceedings, **1**, 99-104, 1993.

[3] Arthur B. Baggeroer, W. A. Kuperman, and Peter Mikhalevsky, "An overview of matched field methods in ocean acoustics", IEEE J. of Oceanic Engineering, **1** (4) 401-424, 1993.

[4] G. A. Grachev, "Theory of acoustic field invariants in layered waveguides," Acoust. Phys. **39** (1), 748756 (1993).

[5] H. C. Song, W. A. Kuperman, and W. S. Hodgkiss ,"A time-reversal mirror with variable range focusing," J. Acoust. Soc. Am **103**, 3224-3240 (1998).

[6] F. B. Jensen, W. A. Kuperman, M. B. Porter, and H. Schmidt, *Computational Ocean Acoustics*, (AIP New York, 1994).

[7] M. B. Porter, "The KRAKEN normal mode program," SACLANT Undersea Research Center, La Spezia, Italy, 1991.

[8] L. M. Brekhovskikh and Yu. Lysanov, *Fundamentals of Ocean Acoustics* (Springer Verlag, Berlin, 1991), pp. 139-145.

[9] S. D. Chuprov, "Interference structure of a sound field in a layered ocean," *Acoustics of the Ocean: Current Status* (in Russian), edited by L. M. Brekhovskikh and I. B. Andreevoi (Nauka, Moscow, 1982), pp. 71-91.

[10] W. J. Higley, Private correspondance.

[11] Philipp Roux, Karim Sabra, and W. A. Kuperman, " Ambient noise cross correlation in free space: Theoretical Approach," J. Acoust. Soc. Am **117**, 79-84 (2005).

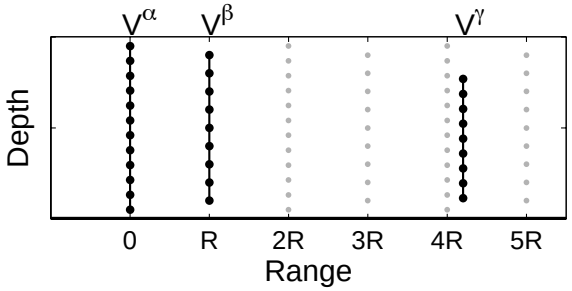

Figure 2.1: Experimental set up. The point-to-point acoustic pressure response sampled between arrays V^α and V^β (indicated by the corresponding dotted black lines) is propagated to generate virtual sampling at integer multiples of the array separation, R. The virtual sampling locations are marked with gray dots. Time-reversing the virtual field corresponding to one of the virtual samples results in a TR focus that is measured by a third array, V^γ.

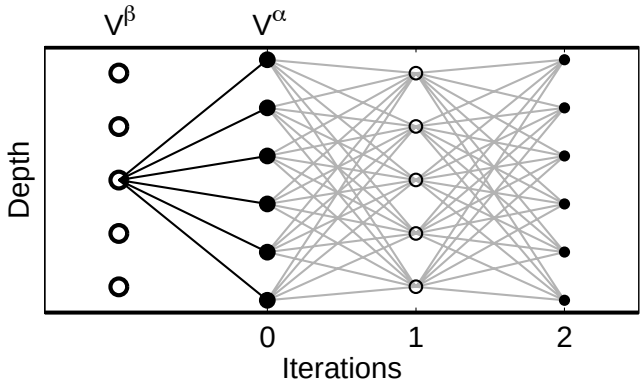

Figure 2.2: Schematic of the iteration procedure for 2 iterations generalized to arrays of differing geometry. Elements of V^α and V^β are indicated by closed and open circles respectively. Larger circles denote actual array elements while smaller circles mark virtual sample locations. The pressure field sampled by V^α due to a source at a chosen element depth on V^β (indicated by the black lines) is chosen as the starter field. Two iterations of the point-to-point array pressure response (gray lines) are applied to propagate the starter field in range.

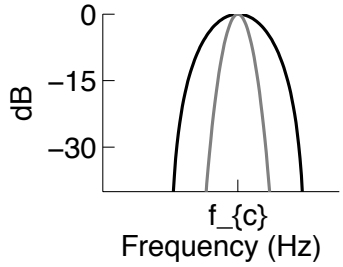

Figure 2.3: Iterative bandwidth narrowing. The black curve marks the Gaussian frequency spectrum of the source signal. The gray line is the bandwidth of the virtual field after 8 iterations. The carrier frequency is indicated by f_c.

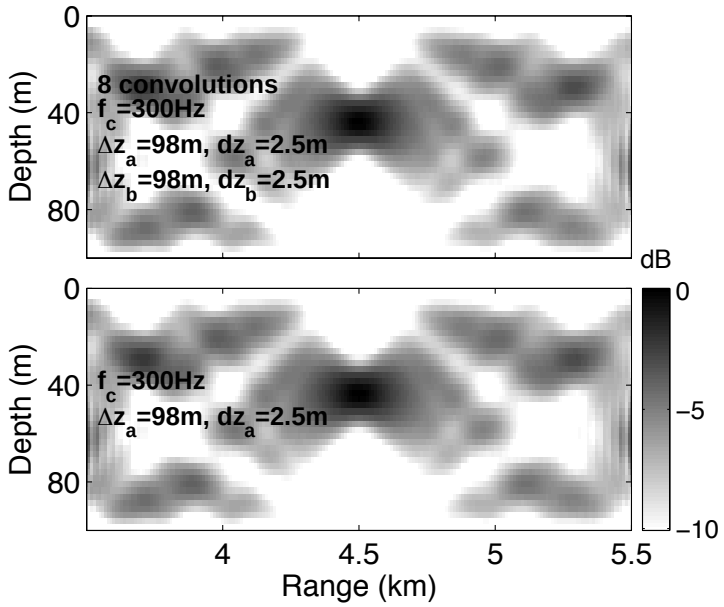

Figure 2.4: Comparison of the spatial components of simulated iterated and modal model benchmark time-reversed fields for the case of full-spanning, densely-sampling arrays. The top panel shows the result after 8 iterations of the field while the bottom panel is the benchmark result for the modeled field for a source at 4.5 km. The water depth is 100 m and the source depth is 45 m. The depth aperture and element spacing interval of array $V^{\alpha}(V^{\beta})$ are given by $\Delta z_{\alpha}(\Delta z_{\beta})$ and $dz_{\alpha}(dz_{\beta})$ respectively. The source signal carrier frequency is given by f_c.

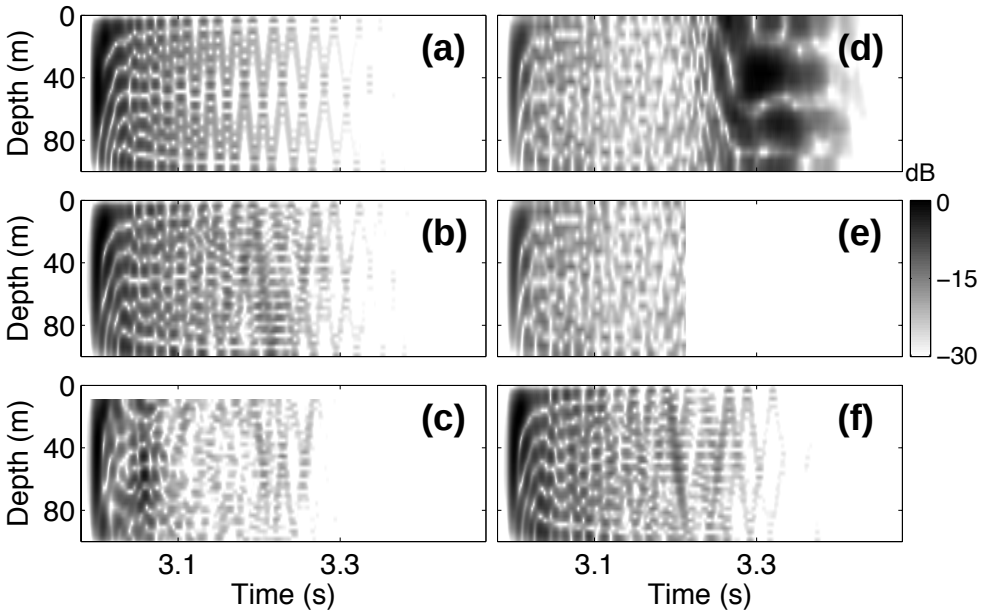

Figure 2.5: Simulated time domain pressure fields for various array geometries. All iteration results are for 8 iterations of the sampled point-to-point pressure response between arrays separated by 500 m. The source signal is characterized by a Gaussian modulated 200 Hz bandwidth at a carrier frequency of $f_c = 300\ Hz$. (a) Benchmark result generated from the modal model for a source at 4.5 km from full-spanning, densely-sampling array. (b) Iteration result for a pair of full-spanning, densely-sampling arrays. (c) Iteration result for the case of partial-spanning, densely-sampling arrays. Arrays V^{α} and V^{β} spanned 90% and 80% of the water column respectively. (d) Iteration result for full-spanning, sparsely-sampling arrays. The sampling interval of the arrays is equivalent to the acoustic wavelength at the carrier frequency in water, $dz = 5\ m$. (e) Iteration result for full-spanning, sparsely-sampling arrays, cleaned to remove aliased high order modal components. (f) Iterative result for tilted full-spanning, densely-sampling arrays compensated to remove the tilt.

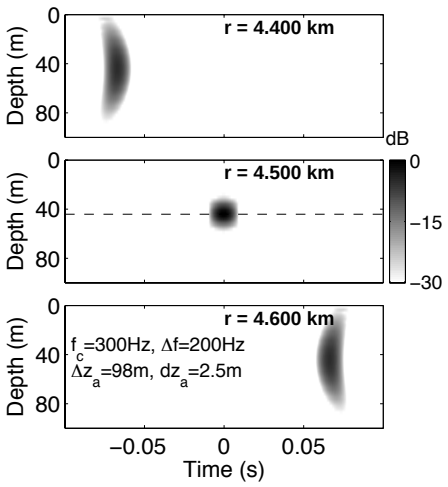
r = 4.400 km
r = 4.500 km
r = 4.600 km
Depth (m)
dB
0
−15
−30
f_c=300Hz, Δf=200Hz
$Δz_a$=98m, dz_a=2.5m
Time (s)

(a)

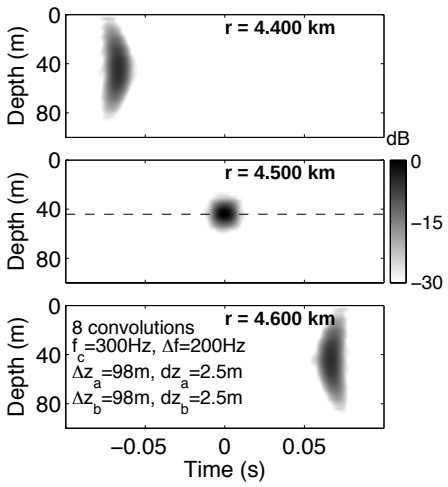
r = 4.400 km
r = 4.500 km
r = 4.600 km
Depth (m)
dB
0
−15
−30
8 convolutions
f_c=300Hz, Δf=200Hz
$Δz_a$=98m, dz_a=2.5m
$Δz_b$=98m, dz_b=2.5m
Time (s)

(b)

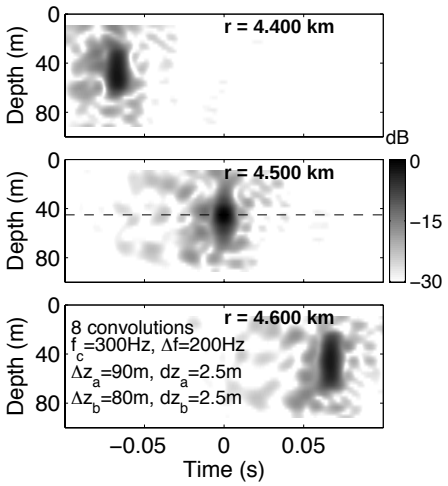
r = 4.400 km
r = 4.500 km
r = 4.600 km
Depth (m)
dB
0
−15
−30
8 convolutions
f_c=300Hz, Δf=200Hz
$Δz_a$=90m, dz_a=2.5m
$Δz_b$=80m, dz_b=2.5m
Time (s)

(c)

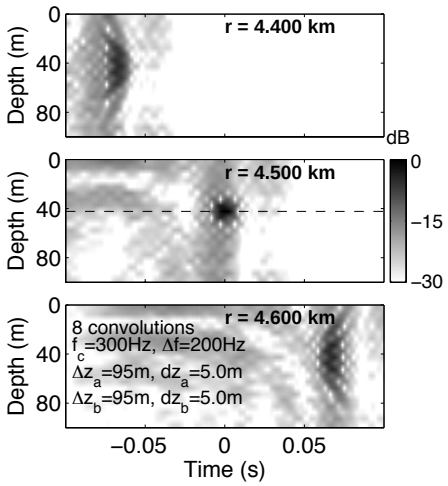
r = 4.400 km
r = 4.500 km
r = 4.600 km
Depth (m)
dB
0
−15
−30
8 convolutions
f_c=300Hz, Δf=200Hz
$Δz_a$=95m, dz_a=5.0m
$Δz_b$=95m, dz_b=5.0m
Time (s)

(d)

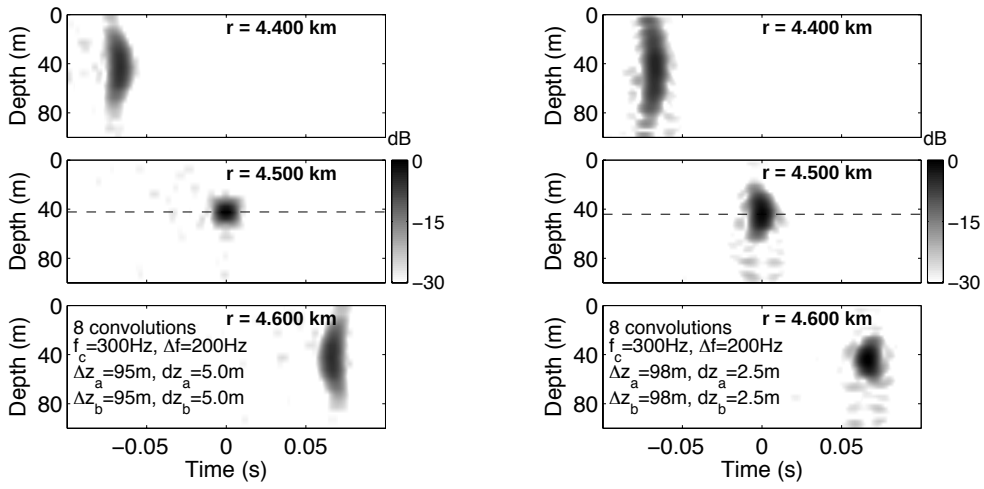

(e) (f)

Figure 2.6: Simulated time domain time-reversed pressure fields corresponding to the array geometries of Fig. 2.5. All TR results consist of 3 panels with each panel corresponding to the TR field measured over a receive array (V^{γ} of Fig. 2.1) located at the indicated range. Dashed line indicates the expected focal depth. (a) TR result for the benchmark field of Fig. 2.5(a). (b) TR result for full-spanning, densely-sampling field of Fig. 2.5(b). (c) TR result for partial-spanning, densely sampling case of Fig. 2.5(c). (d) TR result for full-spanning, sparsely-sampling field of Fig. 2.5(d). (e) TR result for cleaned full-spanning, sparsely-sampling field of Fig. 2.5(e). (f) TR result for compensated tilted array case of Fig. 2.5(f). The depth aperture and element spacing interval of array $V^{\alpha}(V^{\beta})$ are given by $\Delta z_{\alpha}(\Delta z_{\beta})$ and $dz_{\alpha}(dz_{\beta})$ respectively. The source signal bandwidth and carrier frequency are indicated by Δf and f_c respectively.

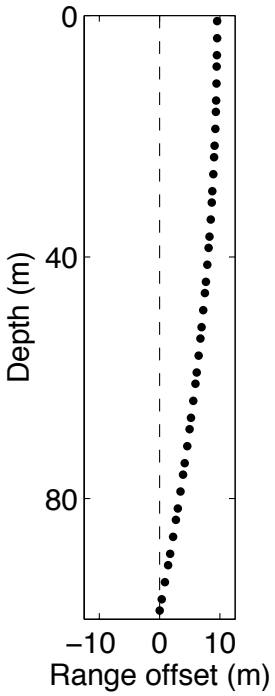

Figure 2.7: Array tilt schematic. Dots indicate locations of array elements of V^{β} relative to the deepest element.

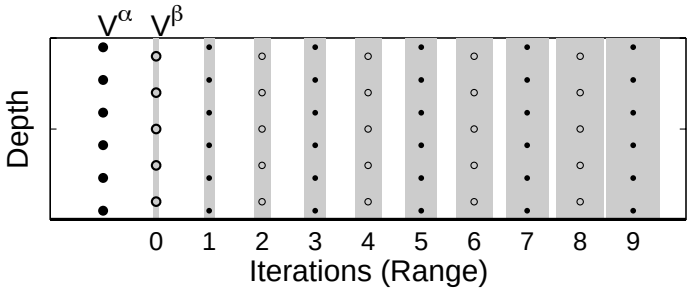

Figure 2.8: Schematic of the coverage of the waveguide resulting from combining the iteration method with variable range TR generalized to the case of arrays of differing geometry. Closed and open circles indicate the element depths of arrays V^{α} and V^{β} respectively. As a set these points represent the ensemble of virtual samples generated by the iteration process. The shaded gray areas indicate the regions of the waveguide to which TR focusing can be achieved when the iteration method is combined with variable range TR.

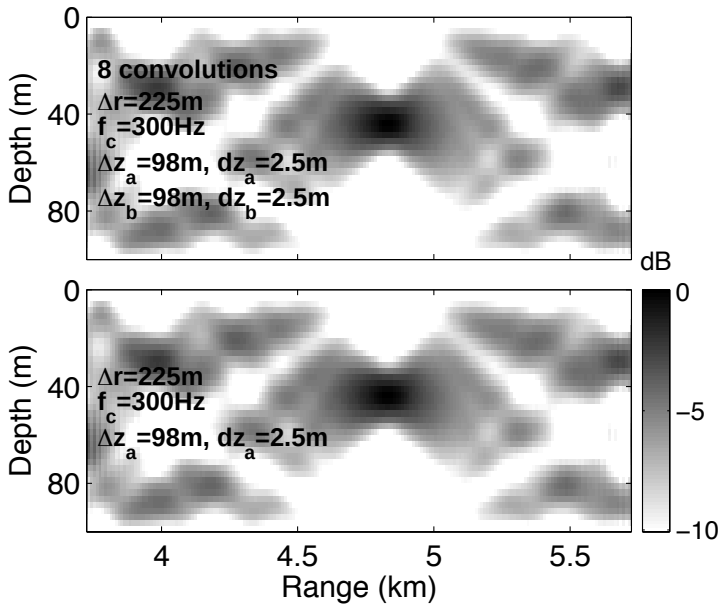

Figure 2.9: Comparison of the spatial components of simulated iterated and modal model benchmark range-shifted time-reversed fields for the case of full-spanning, densely-sampling arrays. The top panel shows the result after 8 iterations of the field while the bottom panel is the benchmark result for the modeled field for a source at 4.5 km. In both cases a fractional frequency shift of $\Delta\omega/\omega = +0.05$ has been applied resulting in the perceived range shift of the fields. The expected range shift, δr, for a $\beta = 1$ waveguide is indicated. The water depth is 100 m and the source depth is 45 m. The depth aperture and element spacing interval of array $V^{\alpha}(V^{\beta})$ are given by $\Delta z_{\alpha}(\Delta z_{\beta})$ and $dz_{\alpha}(dz_{\beta})$ respectively. The source signal carrier frequency is indicated by f_c.

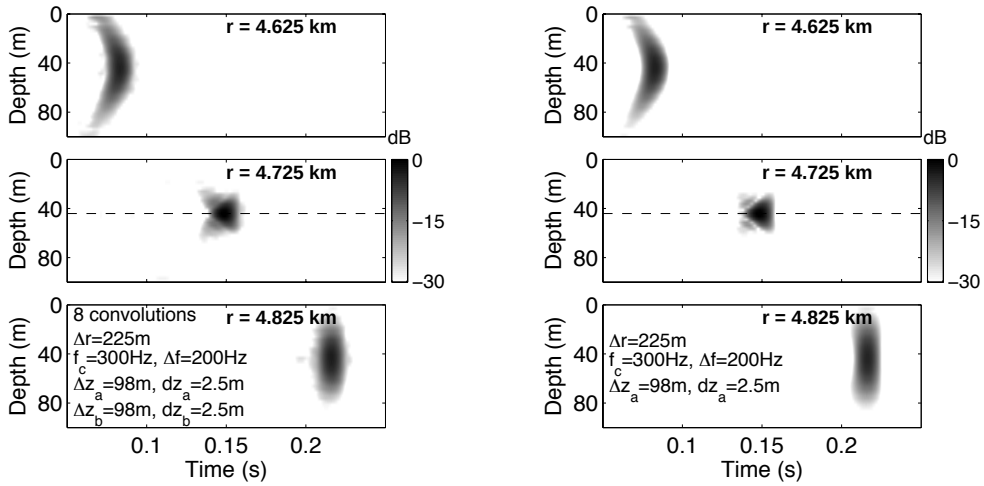

Figure 2.10: Simulated time domain range-shifted time-reversed pressure fields corresponding to the fields shown in Fig. 2.9. Each TR result consists of 3 panels with each panel corresponding to the TR field measured over a receive array (V^{γ} of Fig. 2.1) located at the indicated range. (a) Range-shifted iterated result. (b) Range-shifted benchmark result. The time axes indicate the delay with respect to the arrival time of the non-range-shifted TR focus at $r = 4.5\ km$. The dashed line indicates the expected focal depth. The expected range shift, δr, for a $\beta = 1$ waveguide is indicated. The depth aperture and element spacing interval of array $V^{\alpha}(V^{\beta})$ are given by $\Delta z_{\alpha}(\Delta z_{\beta})$ and $dz_{\alpha}(dz_{\beta})$ respectively. The source signal bandwidth and carrier frequency are indicated by Δf and f_c respectively.

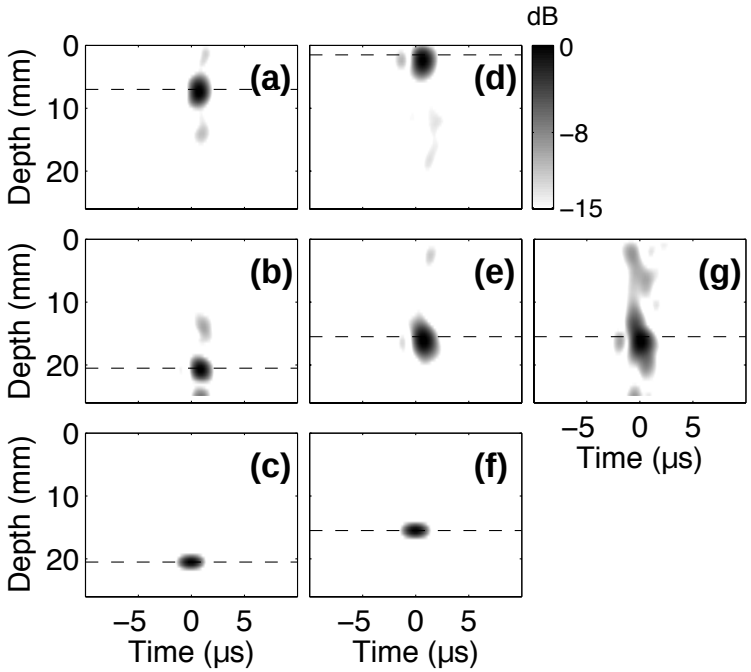

Figure 2.11: Experimental time domain time-reversed pressure fields. In all cases, the dashed line indicates depth of the source from which the TR field originated (real or virtual). Panels (a) and (b) show the TR foci produced by iterated fields (4 iterations) corresponding to virtual sources at $r = 414\ mm = 5R$. Panel (c) is the TR result for a real source at the same range. Similarly, (d) and (e) show the TR foci produced by iterated fields (9 iterations) corresponding to virtual sources at $r = 828\ mm = 10R$ with panel (f) giving the TR result for a real source at the same range. Panel (g) corresponds to panel (e). In this case, array tilt was not accounted for. The source signal bandwidth and carrier frequency were $f_c = 1.5\ MHz$ and $\Delta f = 1.5\ MHz$, respectively.

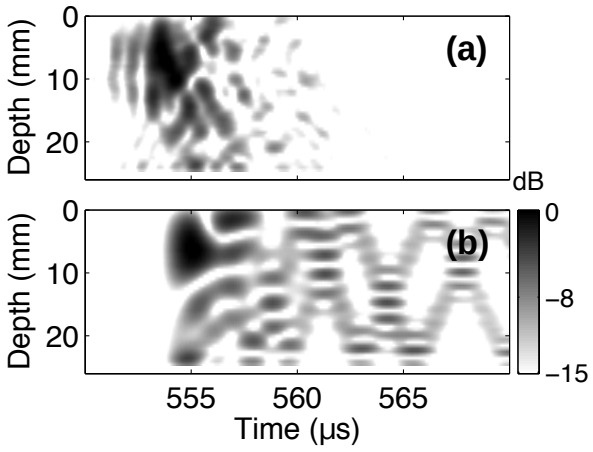

Figure 2.12: Experimental time domain pressure fields used to generate TR fields. Panel (a) is the iterated pressure field due to a virtual source used to produce the TR focus of Fig. 2.11(e). Panel (b) is the direct sampled pressure field due to a real source that resulted in the TR focus of Fig. 2.11(f).

Chapter 3

Data-based mode extraction with a partial water column spanning array

abstract

In a shallow ocean waveguide the acoustic field can be characterized by depth dependent modes propagating in range with an associated propagating wavenumber. Though recently developed methods for determining the modes from recorded acoustic data alone without ocean or bottom modeling have shown promise, they are only applicable when the acoustic field is sampled over the entire water column. This paper presents a method for determining the acoustic modes from measured data alone when the field is sampled over only a portion of the water column. The method requires broadband sources at many ranges, e.g., a moving source, in order to construct the frequency-wavenumber (f-k) structure of the waveguide. Because modal propagation is dispersive, the modes are characterized by a discrete set of wavenumbers that vary continuously with frequency. Due to the discreteness of the modal wavenumbers, it is possible to isolate the modes in the f-k domain and extract them individually with a singular value decomposition (SVD). Because the modes

are extracted individually the full-spanning and degeneracy limitations of the SVD are removed. Theory, simulation, and laboratory data confirm the process.

3.1 Introduction

The normal mode structure of an ocean waveguide is not only fundamental to describing propagation, but also provides opportunities for various types of array and signal processing[1]. In range-independent environments, matched mode or mode filtering methods [2, 3, 4] offer an effective alternative to more general matched field methods [5] that tend to be computationally costly and highly sensitive to environmental mismatch. Matched mode methods apply a knowledge of the modal components of the field to measured data over a vertical array of sensors. Typically, the modal components are constructed from theory using parameters derived from a detailed knowledge of the environment. The difficulty and high cost of obtaining the necessary environmental information has motivated research into the development of model-free methods for determining the modes of acoustic propagation. Of particular interest are methods that can be directly applied to acoustic data measured on a vertical line array (VLA) without any a-priori information. Current research strategies range from active methods involving feedback between a pair of VLAs [6] to passive methods in which a VLA is used to accumulate information from acoustic sources and/or noise in the environment [7, 8, 9, 10]. This paper demonstrates that, under certain conditions, normal modes can be extracted passively from the received acoustic field in a waveguide without a full water column spanning array, without environmental information and without any modeling.

We introduce a method for determining the acoustic modes of propagation from sound received on a partial-spanning VLA from a horizontally moving source. The method involves a combination of masking individual modal dispersion curves contained in a frequency-wavenumber (f-k) analysis of the data, and a subsequent singular value decomposition (SVD). The method is related to earlier work by Frisk

and Lynch [11] in which they Hankel transformed (over range) acoustic data (at a single frequency) recorded on a single receiver from sources spanning a range aperture at a single depth in order to estimate the Green's function characterizing the shallow ocean waveguide. Extending this idea to broadband signals measured at many depths using the receivers of the VLA leads to a comprehensive knowledge of the depth-dependent f-k structure of the waveguide. By combining this knowledge with the physics of modal dispersion, it possible to overcome the inherent limitations to the applicability of other SVD based methods; namely singular value degeneracy and the full-spanning requirement.

SVD methods are based on the premise that the equation describing the decoupled full-spanning cross spectral density matrix (CSDM) of the frequency domain acoustic field is isomorphic to its SVD. Existing SVD methods rely on range, frequency, and ambient noise ensemble averaging to decouple the modes in the CSDM [9, 10]. In this paper we introduce a frequency-wavenumber (f-k) modal dispersion curve isolation, or mode isolation (MI), scheme for decoupling the modes in the CSDM. By decomposing the acoustic field into its wavenumber components, it is possible to isolate the modes in the f-k domain prior to formation of the CSDM. Our scheme involves the formation of several CSDMs, each of which contains significant contributions from only one modal component of the acoustic field. Then a SVD is applied to each f-k averaged CSDM in order to extract each modal depth dependence one at a time. Not only does this eliminate the ambiguities arising from singular value degeneracies, it frees the SVD from its fully-spanning constraint so that modes can be extracted over any portion of the water column for any sound speed profile.

Sec 3.2 reviews the theory of SVD based mode extraction. The conditions under which the SVD of the CSDM is expected to be isomorphic to the depth-dependent modes are discussed in Sec. 3.2.3. The range averaged form of the CSDM introduced in Ref. [9] is used as an example. As well, the limitations of the SVD are addressed, namely those involving singular value degeneracies and normalization over a partial

half-space (Throughout this paper, the term "half-space" is meant to refer to all media below the surface of the water, i.e. the water column and all bottom layers). The MI method is introduced and its advantages over other SVD methods are discussed in Sec. 3.2.4. Mode extraction results for both simulated and laboratory data are presented in Sec. 3.3.

3.2 Theory: Singular value decomposition mode extraction from vertical line array data

In this section we explicitly develop the relationship between acoustic data on an array, normal mode expansions and the SVD process. After presenting this analysis, we then formally develop our extraction method.

3.2.1 Normal mode theory applied to the VLA pressure field

Normal mode theory states that the single frequency component, at angular frequency ω_j, of pressure field, $p(z', z_q, \omega_j, r_h)$, at receiver point $(z = z_q, r = 0)$ in a range-independent waveguide with depth varying density, $\rho(z)$, due to a time varying pressure signal originating from point source, $S(t-t_0)$, located at the source point $(z = z', r = r_h)$ is given by

$$P_{qhj}(z') \equiv p(z', z_q, \omega_j, r_h) = \frac{\sqrt{2\pi}e^{\frac{i\pi}{4}}}{\rho(z')} \sum_{m=1}^{M} \frac{\phi_m(z', \omega_j)\phi_m(z_q, \omega_j)}{\sqrt{k_m(\omega_j)r_h}} e^{-ik_m(\omega_j)r_h} \widetilde{S}(\omega_j). \tag{3.1}$$

Here M is the number of propagating modes supported by the environment, $\widetilde{S}(\omega_j)$ represents the Fourier transform of $S(t - t_0)$

$$\widetilde{S}(\omega_j) \equiv \frac{1}{2\pi} \int_{-\infty}^{+\infty} S(t - t_0) e^{-i\omega_j t} dt, \tag{3.2}$$

and $k_m(\omega_j)$ is the modal wavenumber. The $\phi_m(z_q, \omega_j)$ are the normalized, orthogonal depth dependent mode functions satisfying

$$\int_0^{D'} \frac{\phi_m(z_q, \omega_j)\phi_m(z_q, \omega_j)}{\rho(z_q)} dz_q \equiv \delta_{mn}. \tag{3.3}$$

Rigorously, δ_{mn} represents a Kronecker-delta function when D' spans the entire half space. The variables z_q, ω_j, and r_h are subscripted in order to facilitate the connection between the theoretical discussions in the continuous limit to follow and their discretized experimental implementations. Explicitly, discretization is introduced to describe the experimental situation shown in Fig. 3.1 such that z_q is the depth of the q^{th} VLA receiver element, r_h is the range of the h^{th} source, and ω_j is the j^{th} signal frequency component. Under an integral, a subscript serves as a label on a continuous variable. Under a summation, a subscript serves as a proper index. Functions of subscripted independent variables may also adopt the subscripted notation. Two notable examples are

$$\begin{aligned} k_m(\omega_j) &\rightarrow k_{mj} \\ \phi_m(z_q, \omega_j) &\rightarrow \phi_{qmj}. \end{aligned}$$

3.2.2 The SVD

Any $Q \times Q$ complex matrix $\mathbf{A}$ can always be written as a product of matrices such that

$$\begin{aligned} \mathbf{A} &= \mathbf{U}\mathbf{S}\mathbf{V}^\dagger, \\ A_{qq'} &= \sum_{\alpha=1}^{N} u_{q\alpha} s_{\alpha\alpha} v^*_{\alpha q'}, \end{aligned} \tag{3.4}$$

where $\mathbf{U}$ and $\mathbf{V}$ are unitary matrices, $\mathbf{V}^\dagger$ is the complex conjugate transpose of $\mathbf{V}$, and $\mathbf{S}$ is a diagonal matrix whose elements are the singular values of $\mathbf{A}$ and are positive. N is the number of rows of $\mathbf{Q}$ (and $\mathbf{V}$). $\mathbf{U}$ and $\mathbf{V}$ are unique when the singular values are nondegenerate . Performing a SVD on $\mathbf{A}$ yields $\mathbf{U}$, $\mathbf{V}$, and $\mathbf{S}$. By design, the SVD implementation we use orders the column vectors of $\mathbf{U}$ and $\mathbf{V}$

according to their respective singular values, with the vector corresponding to the greatest singular value appearing in the first column, the vector corresponding to the next highest singular value in column 2, and so forth.

3.2.3 The SVD of the decoupled CSDM and the normal modes

The SVD based mode extraction algorithms defined in Refs. [8] and [9] involve the formation of the spatial Cross Spectral Density Matrix (CSDM), $\mathbf{C}$, as the outer product of the complex frequency domain pressure field, $\mathbf{P} \equiv P_{qhj}(z')$ data array, with its complex conjugate transpose (for either constant h or constant j), $\mathbf{P}^\dagger$, averaged over range and/or frequency. In general, $\mathbf{C}$ is a complex $Q \times Q$ matrix where Q is the number of elements on the VLA. In accordance with Sec. 3.2.2, $\mathbf{C}$ may be written as a product of matrices $\mathbf{U}$, $\mathbf{V}$, and $\mathbf{S}$. Under the proper conditions, an isomorphism exists between some of the columns of $\mathbf{U}$ and the some of the propagating depth-dependent modes. The remainder of this section briefly summarizes the connection between the SVD of the CSDM and the depth-dependent modes using the range averaging or Multiple Range (MR) method of [9] as an example.

In the MR method, the CSDM, $\mathbf{C^{MR}}$, is defined as an average over ranges,

$$\begin{aligned} \mathbf{C^{MR}} &\equiv \left\langle \mathbf{P}\mathbf{P}^\dagger \right\rangle^{\mathbf{MR}} \\ C_{qq'}^{MR} &= \frac{1}{H}\sum_{h=1}^{H} P_{qhj}(z')P_{hq'j}^*(z') \\ &= \sum_{m,n=1}^{M,M} \phi_{qmj}\phi_{nq'j}^* \delta_{mn}^{MR} \end{aligned} \tag{3.5}$$

where

$$\delta_{mn}^{MR} \equiv \frac{2\pi|\widetilde{S}_j|^2\phi_{mj}(z')\phi_{nj}^*(z')}{H\rho^2(z')\sqrt{k_{mj}k_{nj}}}\left(\sum_{h=1}^{H}\frac{e^{-ik_{mnj}r_h}}{r_h}\right), \tag{3.6}$$

$$k_{mnj} \equiv k_{mj} - k_{nj}. \tag{3.7}$$

The MR method utilizes the information from a single frequency component, ω_j, of many acoustic pressure fields recorded at points z_q on the receiver VLA. The pressure fields are accumulated sequentially from sources at many ranges, r_h, all at the same depth z'. For a single frequency (constant j) then, $P_{qhj}(z')$ are the elements of a $Q \times H$ matrix for Q VLA elements and H range samples. For the case of adequate range sampling over a sufficiently large aperture, the summation over range in Eq. (3.6) results in the term in parentheses approaching an unnormalized Kronecker-delta function in the indices m and n. In this case, δ_{mn}^{MR} approaches a diagonal matrix so that Eq. (3.5) reduces to the approximation

$$C_{qq'}^{MR} \approx \sum_{m=1}^{M} \phi_{qmj} \phi_{mq'j}^{*} \delta_{mm}^{MR}. \tag{3.8}$$

Comparison to Eq. (3.4) makes explicit the isomorphism between the matrices $\mathbf{U}$ and $\mathbf{V}$ and the depth dependent modes, ϕ_{qmj}, as well as the isomorphism between the singular values and the diagonal elements δ_{mm}^{MR},

$$\begin{aligned} U_{q\alpha} \equiv \vec{U}_{\alpha} \quad &\leftrightarrow \quad \vec{\phi}_{mj} \equiv \phi_{qmj} \\ s_{\alpha\alpha} \quad &\leftrightarrow \quad \delta_{mm}^{MR}. \end{aligned} \tag{3.9}$$

As the quantity δ_{mm}^{MR} is proportional to the intensity of mode m, the modes will be ordered according to their intensities measured at the VLA. Therefore, column 1 of the matrix $\mathbf{U}$ (and $\mathbf{V}$ as well), $\vec{U}_1$, returned by applying a SVD to the CSDM is isomorphic to the depth-dependent mode of greatest intensity normalized to unity, and so forth. This isomorphism is valid only for modes which are completely decoupled from all other modes, i.e. for modes m for which δ_{mn}^{MR} approaches a Kronecker-delta function for all $n \neq m$. CSDM mode decoupling depends on the total number of sources, H, the span in range, or range aperture, of the sources, Δr, and the sampling interval of the sources, dr [8, 9].

Applying similar reasoning to a frequency averaged form of the CSDM, a method we refer to as the frequency averaging or Multiple Frequency (MF) method, an isomorphism can be established between the frequency averaged acoustic modes and

the SVD column vectors in the case of limited bandwidth where the frequency averaged acoustic modes are an adequate approximation to the true frequency dependent modes. Proceeding further, it is possible to improve mode decoupling, and hence the mode extraction results, by combining the MR and MF methods. This hybrid method, MRMF, applies the SVD to a time and range averaged form of the CSDM to extract the modes.

CSDM mode decoupling is a necessary but not sufficient condition for the extraction of a given mode. For the case of degenerate singular values, $\mathbf{U}$ and $\mathbf{V}$ are not unique. Specifically, all column vectors of $\mathbf{U}$ whose corresponding singular values are degenerate are not unique. Hence, an isomorphism cannot be established between these vectors and any of the depth-dependent modes. As well, because $\mathbf{U}$ is unitary, the isomorphism is valid only when the matrix formed by the set of modes, $\mathbf{\Phi}_j \equiv \{\phi_{qmj}\}$ (the subscript j is included in reference to the MR case where a single frequency component is considered), is unitary. This is only true when $\mathbf{\Phi}_j$ spans the entire half space, otherwise, $\sum_{q=1}^{Q} \phi_{mqj}\phi_{qnj}$ is not diagonal. This requires that the VLA cover the entire water column and that none of the propagating modes penetrate significantly into the bottom. Not only are the range, frequency, and ambient noise averaging techniques so far proposed in the literature constrained by the full-spanning requirement, but they are also hampered by degeneracy limitations (See Sec. 3.2.2).

As a final note, because $\mathbf{U}$ is comprised of Q columns, Q is the maximum number of modes that can be extracted. All the modes can be extracted when $Q \geq M$.

3.2.4 Using the f-k structure of the waveguide to extract the normal modes

In this section we augment the utility of range and frequency information in SVD based methods by considering the underlying physics of modal dispersion in the f-k domain. Not only will such considerations allow us to overcome the degeneracy

limitations of the earlier methods, but they also make it possible to extract all the depth dependent modes projected over a partially spanning VLA.

The mode isolation (MI) method capitalizes on an extra bit of information not considered by the previously discussed mode extraction algorithms: namely, the modal wavenumber pattern of an f-k dispersion representation. By accumulating the frequency domain VLA pressure fields from sources at many ranges all at the same depth, it is possible to apply a Fourier transformation over range as well as time. We note that the source ranges need not be evenly spaced [12]. In the case of varying sampling interval, the sampling intervals must be known. The range-wavenumber transformation results in the frequency-wavenumber structure of the waveguide projected over the VLA. This information is useful because in a horizontally stratified waveguide the modal wavenumbers are discrete and localized in the f-k domain, making it possible to isolate the modes (depending on the wavenumber resolution) from one another so that their depth dependence may be extracted individually. The effect of the isolation process is to reweight each isolated mode such that its effective excitation is much greater than the effective excitations of the other modes. This ensures that, upon applying the SVD to the isolated mode CSDM, the column vector of $\mathbf{U}$ corresponding to the greatest singular value, denoted here as $\vec{U}_1$, is associated with the isolated mode. By design, the SVD calculates the orthogonal column vectors of $\mathbf{U}$ sequentially according to their singular value. As each vector is calculated, it is constrained to be orthogonal with respect to each and every previously calculated vector. Because $\vec{U}_1$ is calculated first, it is not is not constrained by the orthogonalization process. Rather, it is merely normalized to unity over the spanning space. Furthermore, in the infinite wavenumber resolution limit ($\Delta r \to \infty$), the mode isolation process guarantees $\vec{U}_1$ to be nondegenerate. As a result, we conclude that $\vec{U}_1$ is isomorphic to the isolated depth-dependent mode projected over the VLA, regardless of the amount of the water column spanned by the VLA.

The remainder of this section is dedicated to the characterization of the MI

process in a quantitative framework. Taking the discrete Fourier transform over the sampled ranges of the pressure field, we define the f-k domain VLA pressure field

$$\widetilde{P}_{qh'j}(z') \equiv \sum_{h=1}^{H} P_{qhj}(z') e^{-i\tilde{k}_{h'} r_h}. \tag{3.10}$$

$\tilde{k}_{h'}$ represents the wavenumber conjugate to the range, r_h. Because it is assumed that all the recorded pressure fields originate from the same source depth, the explicit dependence of the f-k domain pressure field shall be suppressed for the remainder of the paper. Substituting Eq. (3.1) and rearranging yields

$$\widetilde{P}_{qh'j} = \frac{\sqrt{2\pi} e^{\frac{i\pi}{4}}}{\rho(z')} \sum_{m=1}^{M} \frac{\phi_{mj}(z')\phi_{qmj}}{\sqrt{k_{mj}}} \widetilde{S}_j \gamma_{mh'j}, \tag{3.11}$$

where all the wavenumber dependent phase factors have been included in $\gamma_{mh'j}$,

$$\gamma_{mh'j} \equiv \sum_{h=1}^{H} e^{-i\left(\tilde{k}_{h'} + k_{mj}\right) r_h}. \tag{3.12}$$

For constant range sampling interval, dr, $\gamma_{mh'j}$ reduces to the classical array diffraction result,

$$\gamma_{mh'j} = e^{-i\left(\tilde{k}_{h'} + k_{mj}\right) R_0} \frac{\sin\left(\left(\tilde{k}_{h'} + k_{mj}\right)\frac{Hdr}{2}\right)}{\sin\left(\left(\tilde{k}_{h'} + k_{mj}\right)\frac{dr}{2}\right)}. \tag{3.13}$$

where R_0 is the range of the nearest source (at $r = r_1$). The relevance of this result is that $\gamma_{mh'j}$ is peaked around $\tilde{k}_{h'} = -k_{mj}$. Equation (3.13) demonstrates explicitly the dependence of the wavenumber resolution of the f-k pressure field on the range aperture, $\Delta r = Hdr$. $\gamma_{mh'j}$ approaches a delta function, $\gamma_{mh'j} \rightarrow \delta(\tilde{k}_{h'} + k_{mj})$, in the infinite wavenumber resolution limit ($\Delta r \equiv |r_H - r_1| \rightarrow \infty$). For each q then, we recognize $\widetilde{P}_{qh'j}$ to be the f-k diagram of modal propagation at depth z_q defining the frequency dependent wavenumber characteristics of the propagating depth dependent modes. In the f-k domain, the modes appear as distinct, localized curvilinear regions centered on lines defined by $\tilde{k}_{h'} = -k_{mj}$. The localization is a consequence of the discreteness of the modal wavenumber spectrum. Figure. 3.2(a) shows an example of the discrete wavenumber spectrum of a simulated ocean Pekeris

waveguide. All f-k domain dispersion figures show the depth averaged modulus of the spectrum. Because the modal wavenumbers are localized in the f-k domain, it is possible to isolate them. The isolation is accomplished by means of a 2D mask applied in the vicinity of a given mode projected over all VLA elements.

At this point, it is convenient to introduce a modification to our transformation procedure that facilitates the mode isolation process. We emphasize that this modification in no way affects the analysis of the underlying waveguide dispersion physics. Returning to Eq. (3.10), we introduce a frequency dependent weighting factor (in parentheses) and define the rotated pressure field

$$\hat{\tilde{P}}_{qh'j} \equiv \sum_{h=1}^{H} P_{qhj} \left(e^{i\hat{k}_j r_h} \right) e^{-i\tilde{k}_{h'} r_h}. \tag{3.14}$$

Analogously to Eq. (3.12), the wavenumber dependent complex phase dependence of the rotated pressure field is

$$\gamma_{mh'j} \equiv \sum_{h=1}^{H} e^{-i\left(\tilde{k}_{h'} + k_{mj} - \hat{k}_j\right) r_h}. \tag{3.15}$$

As before, for the case of constant range sampling, Eq. (3.15) reduces to the array diffraction result similar to Eq. (3.13), only it is peaked about $\tilde{k}_{h'} = \hat{k}_j - k_{mj}$.

The weighting factor transforms the f-k dispersion structure according to the choice for $\hat{k}_j$. The transformation is arbitrary. For example, choosing $\hat{k}_j$ equal to a constant results in a simple translation in wavenumber of the dispersion structure. For our purposes, we find it convenient to define $\hat{k}_j \equiv k_{1j}$ where k_{1j} is the frequency dependent mode 1 wavenumber. This choice of transformation effectively rotates the f-k structure such that mode 1 curve appears at $\tilde{k}_{h'} \approx 0$ for all frequencies. We approximate the mode 1 wavenumber $k_{1j} \approx \frac{\omega_j}{v_{g1}}$, where v_{g1} is a frequency independent approximation to the mode 1 group velocity, $v_{g1} = 1500\ \frac{m}{s}$ over the bandwidth [13]. Because the modal wavenumber spectrum density increases as mode number decreases, modal wavenumbers of modes 1 and 2 will be the most difficult to resolve, and therefore, the most difficult to isolate. This choice of rotation facilitates the isolation of the low order modes by rendering them nearly vertical. Fig. 3.2(b)

shows the rotation applied to the f-k structure of Fig. 3.2(a). In this example using simulated shallow ocean waveguide data, all 5 propagating modes are well resolved in wavenumber.

Referring to the f-k dispersion structure, the mask of mode ν is defined as the set of $\tilde{k}_{h'}$ for which

$$\hat{k}_j - k_{\nu j} - \epsilon_\nu \leq \tilde{k}_{h'} \leq \hat{k}_j - k_{\nu j} + \epsilon_\nu \tag{3.16}$$

for each frequency component of interest. The width (in wavenumber) of the mode ν mask is determined by the quantity ϵ_ν. The mask width, and hence ϵ_ν, should be large enough that the mask contains all the important features of mode ν, but still small enough that it does not incorporate significant features of adjacent modes. We adopt the notation $\{X\}_\nu$ to represent the mode ν masking operation applied to the quantity X where X is a synthesis of modal components, $X = \sum_{m=1}^{M} x_m$. Because it is an isolation operation, the masking operation conceptually behaves similarly to the Kronecker delta function, $\delta_{m\nu}$. It isolates the mode ν component of quantity X, $\{X\}_\nu \approx x_\nu$. Applying the masking operation to the rotated f-k pressure field yields,

$$\{\hat{\tilde{P}}_{qh'j}\}_\nu \approx \frac{\sqrt{2\pi}e^{\frac{i\pi}{4}}}{\rho(z')} \frac{\phi_{\nu j}(z')\phi_{q\nu j}}{\sqrt{k_{\nu j}}} \widetilde{S}_j \gamma_{\nu h' j}. \tag{3.17}$$

This form for the masking operation applied to the pressure field is valid in the limit that $\gamma_{mh'j} \longrightarrow \gamma_{\nu h'j}$ over the mask region (the region defined by condition (3.16)). This is indeed the case when mode ν is well isolated and a mask containing only mode ν can be defined unambiguously. That is, as long as the wavenumber resolution is adequate to render mode ν distinct from its neighboring modes, $\nu - 1$ and $\nu + 1$, in the f-k domain, the dominant contribution to the the pressure field, and hence the CSDM, within the mask comes from mode ν.

Because the depth dependence of the modes is unaffected by the transformation process ($r \rightarrow k$), it is not necessary to transform back from wavenumber to range in order to form the CSDM. Defining the mask such that there are the same number of wavenumber elements, H', for each frequency, $\{\hat{\tilde{P}}_{qh'j}\}_\nu$ is a $Q \times H' \times J$ array which can be used to form the CSDM directly. J here is the number of frequency

components included in the mask. The CSDM is then defined as the double sum over the mode ν mask region

$$C_{qq'} = \frac{1}{H'J} \sum_{h',j=1}^{H'J} \{\hat{\widetilde{P}}_{qh'j}\}_\nu \{\hat{\widetilde{P}}_{qh'j}\}^*_\nu. \tag{3.18}$$

Notice the sum over range is replaced by a sum over the wavenumbers defined by the mask.

Because the CSDM involves frequency averaging, care must be taken in establishing an isomorphism between the modes and the column vectors of the SVD matrix $\mathbf{U}$. Rigorously, the isomorphism is only valid when the depth-dependence of the modes can be considered frequency independent. In practice this means that the frequency must be limited to a bandwidth over which the modal depth dependence is nearly constant. In this case the extracted modes can be thought of as an average over the bandwidth, $\phi_{q\nu j} \rightarrow \langle \phi_{q\nu} \rangle$, so that upon substitution by Eq. (3.17), Eq. (3.18) takes the form

$$C_{qq'} = \langle \phi_{q\nu} \rangle \left\langle \phi^*_{\nu q'} \right\rangle \widetilde{\delta}_\nu, \tag{3.19}$$

where

$$\widetilde{\delta}_\nu \equiv \frac{2\pi \langle \phi_\nu(z') \rangle \langle \phi^*_\nu(z') \rangle}{H'J\rho^2(z')} \left(\sum_{h',j=1}^{H'J} \left(\frac{|\widetilde{S}_j|^2}{\sqrt{k_{\nu j} k_{\nu j}}} \right) \gamma_{\nu h' j} \gamma^*_{\nu h' j} \right). \tag{3.20}$$

Clearly then, when mode ν is well resolved in wavenumber (as is the case with mode 4 in Fig. 3.2(c)), performing the singular value decomposition of $\mathbf{C}$ yields the matrix $\mathbf{U}$ such that the column vector $\vec{U}_1$ is isomorphic to the frequency averaged depth-dependent mode ν with corresponding singular value s_{11} proportional to $\widetilde{\delta}_\nu$,

$$\begin{aligned} U_{q1} &\leftrightarrow \langle \phi_{q\nu} \rangle \\ s_{11} &\leftrightarrow \widetilde{\delta}_\nu. \end{aligned} \tag{3.21}$$

In the case where the masked mode is not well resolved in wavenumber, it is not possible to define a mask that contains only mode ν and the SVD will not work for this mode.

To determine the resolvability of the modal wavenumbers, we consider the range-wavenumber relations of numerical Fourier transform implementations such as the FFT,

$$\begin{aligned} \Delta r &= \frac{2\pi}{d\widetilde{k}} \\ dr &= \frac{2\pi}{\Delta\widetilde{k}}. \end{aligned} \tag{3.22}$$

The mode ν wavenumber will be well resolved when the rotated wavenumber sampling interval is much less than the minimum interval separating adjacent modes within the bandwidth, $d\widetilde{k} \ll |k_{\nu j} - k_{(\nu-1)j}|_{min}$. This condition determines the minimum range aperture required to resolve mode ν, Δr_ν, in wavenumber,

$$\Delta r_\nu \gg \frac{2\pi}{|k_{\nu j} - k_{(\nu-1)j}|_{min}}. \tag{3.23}$$

Because $|k_{\nu j} - k_{(\nu-1)j}|_{min}$ decreases as ν decreases, this effectively sets a lower limit on the lowest mode that is extractable for a given range aperture. At the other end of the spectrum, the width of the rotated wavenumber domain, $\Delta\widetilde{k}$, of the f-k diagram determines the highest order mode appearing in the f-k structure. Then the upper limit on ν that is extractable for a given range sampling interval is set by the condition

$$dr = \frac{2\pi}{|k_{\nu j} - k_{1j}|_{max}}. \tag{3.24}$$

In the context of ocean applications, the range aperture needed to resolve mode ν (in the low mode order limit, $\nu \ll \frac{2D}{\lambda_w}$) is governed by the inequality

$$\Delta r_\nu \gg \frac{8D^2}{\lambda_w\,(2\nu - 1)}. \tag{3.25}$$

Here D is the water depth, and $\lambda_w \equiv \frac{f_0}{c_w}$ is the acoustic wavelength in the water (characterized by sound speed c_w) at frequency f_0. For example, in order to extract all the propagating modes excited by a moving broadband source radiating at a central frequency of 150 Hz in a 100 m deep waveguide, the source would have to cover greater than 8 km in range aperture. However, extracting modes 3 and greater would require only $\frac{1}{5}$ the range aperture. The sampling interval requirement can be

written in terms of physical parameters as $dr \approx \lambda_w \left(\frac{c_b}{|c_b - c_w|} \right)$. For water and bottom sound speeds $c_w = 1500 \ \frac{m}{s}$ and $c_b = 1800 \ \frac{m}{s}$, the sampling interval can be as large as 18 m $(= 6 \ \lambda_w)$.

3.3 Results: Application of the MI method to data

In this section we include comparisons of the depth-dependent mode extraction results of the MRMF and MI methods. Mode extractions using both simulated and experimental data are shown. The simulated mode extractions are useful because they allow us to compare the extracted modes with the true modes used to generate the simulated pressure fields. The experimental mode extractions provide a demonstration that the MI mode extraction method is experimentally applicable, a crucial first step proof of concept for shallow ocean applications. In the following sections, the vectors returned by the SVD operation are called SVD-vectors. This is done in order to differentiate them from the theoretical modes used to generate the simulation. This differentiation also serves to emphasize that these objects are not always faithful representations of (isomorphic to) the true modes of acoustic propagation.

The effectiveness of range averaging (MR) and ambient noise decoupling SVD methods over a full-spanning array have been demonstrated [9]. Except for degeneracy limitations, our work shows that the MRMF technique works as well as the MI method when applied to data over a full spanning array. Therefore, we shall not dwell on full-spanning applications, and instead discuss the more interesting case of partial-spanning applications.

3.3.1 Comparison of MI and MRMF methods applied to a partial-spanning VLA simulation

Range and frequency averaging CSDM decoupling scheme SVD methods, such as the MR, MF, and MRMF methods, have been applied to experimental data. The success achieved by such methods has been demonstrated to be limited by the constraints mentioned in Sec. 3.2.3, namely the degree of mode decoupling in the CSDM, the degeneracy of the singular values, and the full-spanning requirement. Of these, the latter is by far the most stringent constraint. Whereas, some of the modes may be successfully extracted under conditions in which only some of the modes are decoupled and some of the modes are degenerate, these methods fail to extract any of the modes when the VLA does not span the entire water column. The MI technique, on the other hand, can extract all modes for which the wavenumber resolution is adequate over a partial-spanning array. In this section we use simulation to demonstrate the MRMF and MI methods' respective abilities to extract the depth dependent modes of acoustic propagation over a partial-spanning VLA. Because the data is simulated it is possible to compare the extracted modes to theory.

We simulated the VLA pressure fields resulting from distant broadband (400-600 Hz) sources in a shallow ocean Pekeris waveguide characteristic of near shore environments of interest. The water depth was 60 m. The VLA consisted of 33 evenly spaced elements with element 1 at a depth of 12 m and element 33 at depth 44 m. The resulting f-k dispersion is shown in Fig. 3.3. Clearly, there are many propagating modes. The first 12 modes are labeled for clarity. Modes 2, 4, and 6 are weakly excited and do not appear on the dispersion plot. This results from the source depth being chosen to be at the midpoint of the water column.

Fig. 3.4(a) shows the SVD-vectors produced by the MRMF method applied to the simulated pressure field. The MRMF SVD-vectors were matched to all the theoretical modes. Each SVD-vector is plotted with its closest matching theoretical mode. On the other hand, as seen in Fig. 3.4(b), when it comes to extracting

depth-dependent modes projected over only a portion of the water column, the MI method performs remarkably well. Whereas in the MRMF case we do not automatically know to which mode a given SVD-vector corresponds, in the MI case we know which mode we are attempting to extract. As the wavenumber separation between the modes decreases, each mask contains increasing residuals from adjacent modes. If the mode for which the mask is defined is weakly excited compared to an adjacent mode, the extraction process will result in a mix of adjacent modes. As a result, we see that the weakly excited modes (2, 4, and 6) are not well extracted. The remaining modes are well extracted, with one caveat. It is possible to properly determine mode 1 in this example only because mode 2 is absent. Otherwise, due to the limited wavenumber resolution, it would not have been possible to isolate mode 1 from mode 2.

3.3.2 MI method applied to experimental data

Fig. 3.5 shows mode extraction results of the MI method applied to experimental data. The experiment was designed to mimic a typical shallow ocean range-independent environment at approximately a 1:10000 scale. Whereas ocean environments of interest typically involve ranges on the order of kilometers, depths on the order of tens of meters, and wavelengths on the order of meters, the experimental ranges were on the order of a meter (ranges between 390 mm and 990 mm), the experimental depth was on the order of tens of millimeters ($D \approx 27$ mm), and the acoustic wavelength was on the order of millimeters ($\lambda \approx 2.5$ mm). The waveguide consisted of approximately 27 mm (≈ 10.5 λ) of fresh water over a homogenous sand bottom. A vertical line array (VLA) measured the pressure fields individually from $H = 301$ identical broadband ultrasonic sources (400 kHz bandwidth at 600 kHz carrier frequency) located at evenly spaced range intervals between 390 mm and 990 mm ($\approx 160 - 400$ λ). The VLA consisted of $Q = 31$ evenly spaced hydrophones spanning most of the water column (see Fig. 3.1). The absolute depths of the array elements were unknown. The minimum and maximum source ranges were con-

strained by the physical dimensions of the waveguide apparatus. The water depth and source frequency were chosen to produce 10 propagating modes in a regime where the wavenumber resolution produced by the range aperture would be adequate for resolving most of the modal wavenumbers. The source depth was chosen to be near the bottom to ensure that all the modes would be excited by the source. As seen in the resulting f-k diagram of Fig. 3.5(a), there were indeed 10 propagating modes, 7 of which were well isolated. Fig. 3.5(b) shows the MI SVD-vectors resulting from both full-spanning (dashed lines) and partial-spanning (dark lines) VLA geometries. The full spanning case utilized data from all 31 VLA elements, while the partial-spanning extraction used data from elements 8-22 ($\approx 6 - 17\ mm$). Excluding mode 1, the full-spanning SVD-vectors appear remarkably sinusoidal. Furthermore, the partial-spanning SVD-vectors coincide perfectly with the corresponding portions of the full-spanning vectors. As mentioned, this would not be the case for the MRMF method. The wavenumber resolution was not adequate to isolate modes 1 and 2 (and perhaps mode 3).

3.4 Summary and discussion

We have demonstrated the conditions under which the singular value decomposition (SVD) of a cross spectral density matrix (CSDM) is expected to yield column vectors that are isomorphic to the depth-dependent modes of acoustic propagation. Typically, in order for the isomorphism to be valid (i) the CSDM must sample the entire half space (the vertical line array (VLA) over which acoustic data is recorded, must at least span the entire water column); (ii) the modes must be decoupled in the CSDM; and (iii) the singular values returned by the SVD must be nondegenerate. The constraints posed by these conditions limit the applicability of the current collection of SVD and eigenvalue decomposition mode extraction methods in the literature. The full spanning requirement alone is a formidable constraint to overcome in ocean applications. Add to this the degeneracy limitation, which arises whenever

two or more modes arrive at the VLA with nearly equal intensities, and it is unlikely that such techniques will have significant practical applications in the ocean.

In order to address these shortcomings, we introduced a variation on the current SVD methods which incorporates a knowledge (by measurement) of the dispersion characteristics of the waveguide environment. Because the modes are disperse and localized in the frequency-wavenumber (f-k) domain, it is possible to isolate and deal with them individually. Our mode isolation (MI) technique proved effective at extracting the modes of acoustic propagation over a VLA covering only a portion of the water column. In addition, because the modes are extracted individually, the MI technique does not suffer from degeneracy limitations.

The MI method is subject to two constraints: the soft constraint that the bandwidth be limited to a regime in which the depth dependence of the modes is weakly frequency dependent, and the hard constraint imposed by the available range aperture. The latter constraint, related to the CSDM mode decoupling requirement mentioned in (ii) above, determines the wavenumber resolution. It is the wavenumber resolution that dictates whether or not a given modal wavenumber will be well localized in the f-k domain. The MI technique is expected to perform well when the modes are well localized in the f-k domain regardless of the sound speed profile.

As a practical matter, it is worth mentioning that it is not necessary to determine the absolute ranges of the sources under the condition that they are evenly spaced. In this case transforming to wavenumber leads to the same fundamental f-k modal dispersion. Any error in estimating the range interval between the sources results only in a simple linear wavenumber scaling of the modal dispersion. In ocean applications, time gating the acoustic signal from a passing ship traveling at a constant velocity far from its closest point of approach might fulfill our requirement of evenly spaced acoustic sources. A misestimation of the ship's velocity would result in a linear scaling of the ranges and would not adversely affect the application of the MI mode extraction technique.

3.5 Acknowledgements

This chapter, in full, is a reprint of the material as it appears in The Journal of the Acoustical Society of America, 2005, with authors S. C. Walker, Philippe Roux, and W. A. Kuperman. Reprinted with permission from S. C. Walker, P. Roux, and W. A. Kuperman, "Data-based mode extraction with a partial water column spanning array," J. Acoust. Soc. Am. **118** (3), 1518-1525 (2005).

Bibliography

[1] F. B. Jensen, W. A. Kuperman, M. B. Porter, and H. Schmidt, *Computational Ocean Acoustics*, (AIP New York, 1994).

[2] C. S. Clay, "Waveguides, arrays, and filters," Geophysics 31, 501506 (1966).

[3] T. C. Yang, "A method of range and depth estimation by modal decomposition," J. Acoust. Soc. Am. **82** (5), 1736-1745 (1987).

[4] G. R. Wilson, R. A. Koch, and P. J. Vidmar, "Matched mode localization," J. Acoust. Soc. Am. **84** (1), 310-320 (1988).

[5] Arthur B. Baggeroer, W. A. Kuperman, and Peter Mikhalevsky, "An overview of matched field methods in ocean acoustics", IEEE J. of Oceanic Engineering, **1** (4) 401-424, 1993.

[6] J. R. Buck, J. C. Preisig, M. Johnson, and J. Catipovic, "Single-Mode Excitation in the Shallow-Water Acoustic Channel Using Feedback Control," IEEE J. Oceanic Engineering **22** 2, 281-291, 1997.

[7] S. N. Wolf, D. K. Cooper, and B. J. Orchard, "Environmentally adaptive signal processing in shallow water," Oceans '93, Engineering in Harmony with Ocean Proceedings, **1**, 99-104, 1993.

[8] P. Hursky, W. S. Hodgkiss, and W. A. Kuperman, "Matched field processing with data-derived modes," J. Acoust. Soc. Am. **109** (4), 1355-1366 (2001).

[9] T. B. Neilsen and E. K. Westwood, "Extraction of acoustic normal mode depth functions using vertical line data," J. Acoust. Soc. Am. **111** (2), 748756 (2002).

[10] W. A. Kuperman and F. Ingenito, "Spatial correlation of surface generated noise in a stratified ocean," J. Acoust. Soc. Am. **67**, 1988-1996, 1980.

[11] George V. Frisk, and James F. Lynch, "Shallow water waveguide characterization using the Hankel transform," J. Acoust. Soc. Am. **76** (1), 205-216 (1984).

[12] L. Greengard, June-Yub Lee, SIAM Review, "Accelerating the Nonuniform Fast Fourier Transform", **46** (3), 443-454, (2004).

[13] Barabara Nicolas, Jerome Mars, and Jean-Louis Lacoume, "Geoacoustical parameters estimation with impulsive boat-noise sources," IEEE J. Oceanic Engineering **28** (3), (2003).

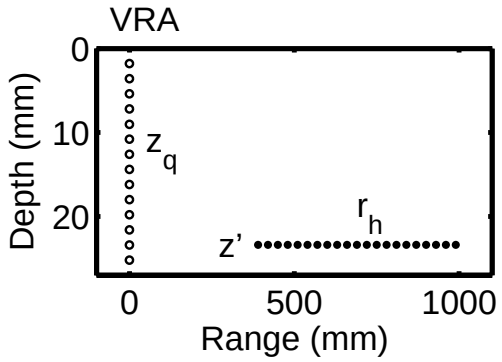

Figure 3.1: Experimental set up. VLA composed of Q transducers at depths z_q (open circles) located at range $r = 0$ records acoustic field from sources at ranges $r = r_h$ and depth z'. The acoustic fields from sources at the same depth for many ranges (closed circles) are recorded individually.

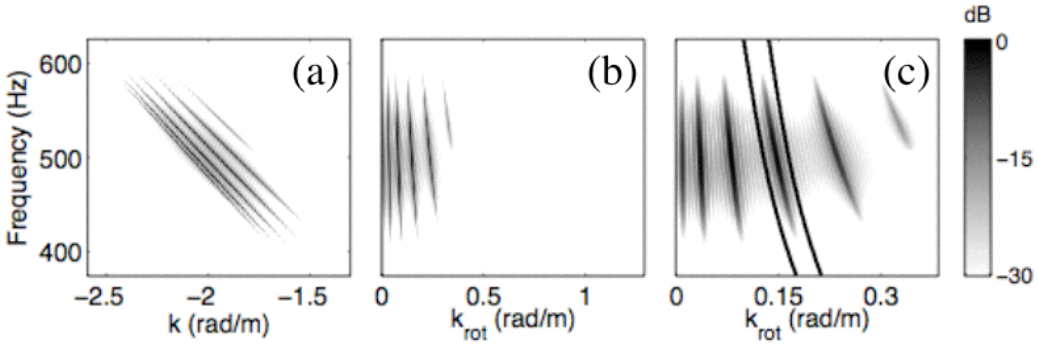

(a) (b) (c)

Figure 3.2: Depth averaged modulus of the f-k structure of a simulated waveguide. Propagating modes appear as localized dark curves. (a) Unrotated f-k structure. (b) Rotated f-k structure. (c) Magnified rotated f-k structure showing the mode 4 mask region (black lines). Simulated waveguide parameters: Pekeris waveguide, $D = 15\ m$, $c_w = 1500\frac{m}{s}$, $c_b = 1800\frac{m}{s}$, $\rho_b = 1800\frac{kg}{m^3}$, $dr = 2\ m$, $\Delta r = 1\ km$, $r_c = 3\ km$ (r_c is the range to the center of the range aperture), $z' = 15\ m$.

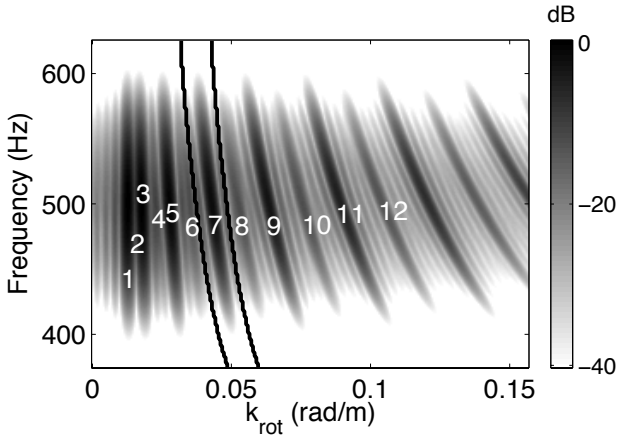

Figure 3.3: Depth averaged modulus of the rotated f-k structure of a simulated waveguide. Propagating modes appear as dark gray curved regions. Modes are enumerated for clarity. Modes 2, 4, and 6 were weakly excited by the source. Hence, they appear to be missing. The mode 7 mask is shown (solid black lines) as an example. Simulation parameters: Pekeris waveguide, $D = 60\ m$, $c_w = 1500\frac{m}{s}$, $c_b = 1800\frac{m}{s}$, $\rho_b = 1800\frac{kg}{m^3}$, $dr = 20\ m$, $\Delta r = 2\ km$, $r_c = 3\ km$, $z' = 30\ m$.

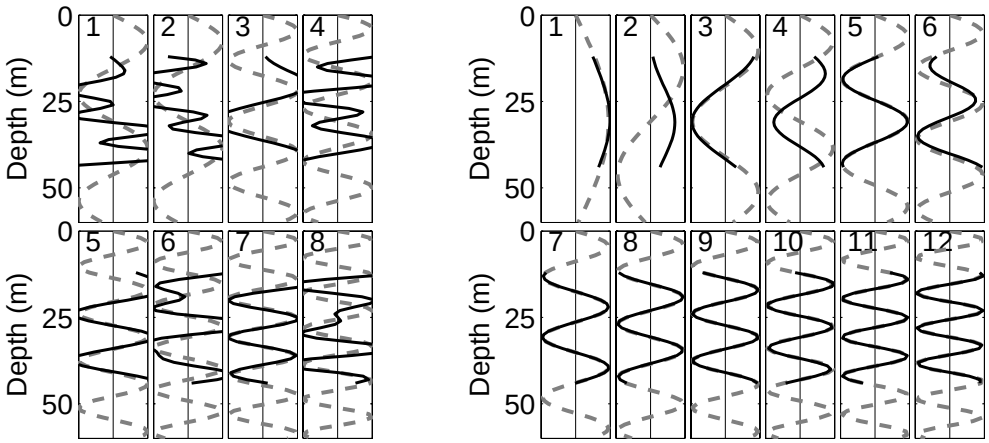

(a) (b)

Figure 3.4: Comparison of MRMF and MI method mode extractions using simulated pressure field data over part of water column ($12 - 44\ m$). (a) Depth-dependent modes extracted using the MRMF method. (b) Depth-dependent modes extracted using MI method. The SVD-vectors (solid lines) are plotted with the theoretical modes (dashed lines) used to generate the data. Each numbered panel shows one SVD-vector along with corresponding theoretical mode. In the MRMF case only the real components of the 8 best matching MRMF SVD-vectors are shown along with their best matching theoretical modes. Simulation parameters: Same as Fig. (3.3).

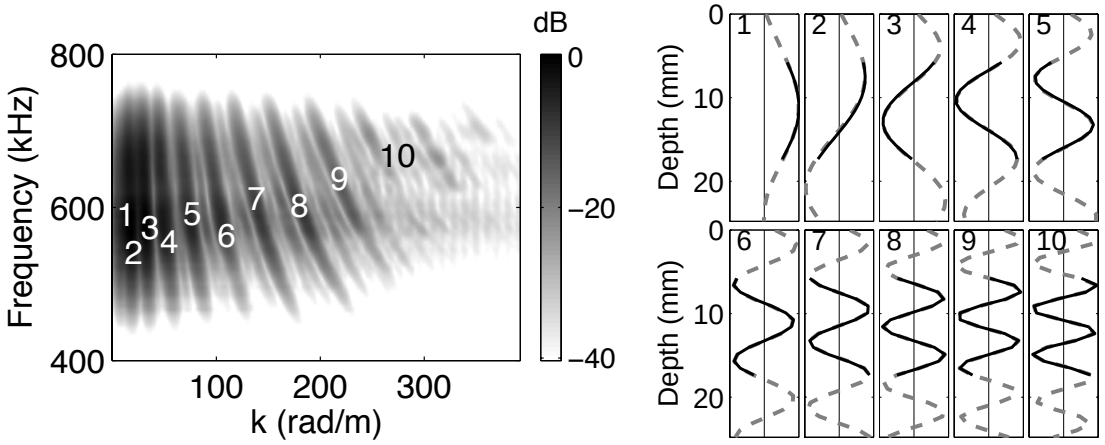

(a) (b)

Figure 3.5: MI method mode extraction results using ultrasonic experimental pressure field data over full-spanning (VLA elements 1-31) and partial-spanning (elements 8-22) VLAs. (a) Depth averaged modulus of the rotated f-k structure of the experimental waveguide. Propagating modes appear as dark gray curved regions. Modes are enumerated for clarity. (b) MI SVD-vectors from partial-spanning VLA data are indicated with solid lines. Full-spanning VLA SVD-vectors appear as dashed lines. Only modes 1-10 are shown. Experimental parameters: fresh water over sand bottom, $D = 27\ mm$, $c_w \approx 1490\frac{m}{s}$, c_b unknown, ρ_b unknown, $z' \approx 26\ mm$, $dr = 1\ mm$, $\Delta r = 600\ mm$, $r_c = 690\ mm$.

Chapter 4

Focal depth shifting of a time reversal mirror in a range-independent waveguide

abstract

A time-reversal mirror (TRM) refocuses back at the original probe source position. A goal has been to refocus at different positions without model based calculations. A method to refocus at different ranges has already been developed using frequency shifting. Here we present a technique to refocus at different depths than the original probe source in a shallow ocean range-independent waveguide. The requirement is to collect data from various ranges at a single depth, as from a moving broadband radiator, over a distance sufficient to construct the relevant frequency-wavenumber (f-k) structure of the waveguide. With this information, it is then possible to focus at arbitrary depth at any of the ranges that the probe source data were taken. Experimental results confirm the theory.

4.1 Introduction

Acoustic time-reversal (TR) focusing has been demonstrated to produce temporally and spatially focused acoustic signals in a static ocean environment. TR focusing consists of recording the pressure field from a distant probe source over a portion of the water column, reversing the signal in time and propagating the time-reversed signal back through the medium resulting in a pressure field that is temporally and spatially focused at the probe source location. The spatio-temporal focusing is a consequence of the time-reversal invariance of the linear lossless wave equation describing acoustic propagation in the ocean environment [1]. In waveguide acoustic environments that are range independent, the acoustic field propagates as dispersive normal modes[2]. In shallow ocean waveguide applications, TR is often implemented using a vertical line array (VLA) of acoustic transducers covering some or all of the water column. The VLA is often referred to as a time-reversal mirror (TRM) [1].

A TRM is limited by the requirement that a probe source initially broadcast from the desired focal spot. A method for shifting the TR focus in range by altering the frequency characteristics of the pressure field has been experimentally demonstrated [3]. As well, a method for shifting the TR focus in both depth and range in an iso-velocity waveguide in the high bandwidth limit has been proposed [4]. The ability to depth shift a TR focus might find applications to MIMO communications [5, 6]. For example, the data rate can be increased by sending different information to different depths simultaneously. This paper introduces a method for shifting the TR focus in depth from the initial probe source depth in the finite bandwidth modal propagation regime. The method is an extension of the frequency-wavenumber (f-k) mode extraction method introduced in Ref. [3]. Although other methods for extracting the depth dependence of the propagating modes exist (such as the control feedback method introduced in Ref. [8], the amient noise eigen-value decompostion methods discussed in Refs. [9, 10], and the moving source singular-value decompo-

sition method proposed in Ref. [2]), we find the f-k analysis of Ref. [3] particularly useful for depth shifting.

Similarly to the method of Ref. [12] generalized to broadband signals in the far-field regime, the f-k structure of the waveguide is constructed by Fourier transforming, in both range and time, the acoustic pressure fields measured over a TRM from sources at many ranges all at the same depth, z'. Due to the dispersion of the waveguide, it is possible to isolate the modes according to their discrete wavenumbers in the f-k domain and extract them individually. In addition, their wavenumber components may be modulated independently. Noting that the relative intensities of the modal components of the f-k structure are a function of the source depth and the depth dependence of the modes, the extracted modes can be used to remodulate the isolated modal components individually resulting in a depth shifting of the f-k structure. Transforming the depth shifted f-k structure back to the time-range domain yields the desired depth shifted time-domain TRM pressure fields for each initial source range. The depth shifted pressure fields can be time-reversed to produce TR foci at any of the initial ranges. The process is presented schematically in Fig. 4.1. The dimensions of Fig. 4.1 describe our experiment at ultrasonic frequencies ($\sim 600\ kHz$, $\frac{D}{\lambda} \approx 10$, $\frac{\Delta r}{\lambda} \approx 250$), where λ is the carrier wavelength of the acoustic field, D is the water depth, and Δr is the range over which data is recorded. The process is equally applicable to spatial scales characteristic of the shallow ocean in the regime $\frac{\Delta r}{\lambda} \approx \left(\frac{D}{\lambda}\right)^2$ [13]. Choosing a practical limit on the range aperture, $\Delta r \leq\ 5km$, limits the applicability of this technique to regimes involving 5 to 40 propagating modes, $5 \leq \frac{D}{\lambda} \leq 40$, where the lower limit results from the minimal TR focus resolution for which depth shifting is useful.

Though this technique may be adapted to weakly range-dependent (adiabatic) bathymetries, we have chosen to limit our analysis to range-independent environments in order to facilitate the description of the underlying physics. Broadening the scope of the discussion to range-dependent environments would overly complicate the analysis.

The theory of depth shifting by mode remodulation is presented in Sec. 4.2. It is developed and presented in conjunction with experimental results in Sec. 4.3. The experimental results serve to illustrate the theory. Complications associated with the depth shifting procedure are dealt with in Sec. 4.4. A discussion and summary is given in Sec. 4.5.

4.2 Theory of mode remodulation depth shifting

According to normal mode theory, the pressure field at angular frequency component, ω, measured over a vertically oriented TRM (with elements at discrete depths z_q $\{q = 1, 2, \ldots, Q\}$) located at $r = 0$ due to a point source at (r, z') in a range-independent waveguide can be expanded into a superposition of depth-dependent normal modes,

$$\vec{P}(z', r, \omega) = \sum_{m=1}^{M} \vec{\phi}_m(\omega)\phi_m(z', \omega)\psi_m(r, \omega), \tag{4.1}$$

where

$$\psi_m(r, \omega) \equiv \frac{i\widetilde{S}(\omega)}{4\rho_0} H_0^{(1)}\left(k_m(\omega)r\right). \tag{4.2}$$

$\widetilde{S}(\omega)$ is the complex frequency component of the source signal, $k_m(\omega)$ is the mode m propagating wavenumber, and ρ_0 is the medium density. $\vec{\phi}_m(\omega) \equiv \{\phi_m(z_q, \omega)\}$ and $\vec{P}(z', r, \omega) \equiv \{P_q(z', r, \omega)\}$ are Q component vectors representing the projections over the TRM of the mode m depth dependence and the pressure field respectively. M is the total number of propagating modes supported by the waveguide.

Each normal mode arrives at the TRM with an associated amplitude and phase given by $\phi_m(z', \omega)\psi_m(r, \omega)$. The depth dependence of the mode amplitudes, $\phi_m(z', \omega)$, has been isolated in Eq. (4.1) in order to emphasize the dependence of the mode amplitudes on the source depth. The pressure fields from point sources at different depths at the same range differ only by the relative amplitudes of the modes and

are related through

$$\begin{aligned}\vec{P}(z'',r,\omega) &= \sum_{m=1}^{M} \vec{\phi}_m(\omega)\phi_m(z'',\omega)\psi_m(r,\omega) \\ &= \sum_{m=1}^{M} \vec{\phi}_m(\omega)\left(\frac{\phi_m(z'',\omega)}{\phi_m(z',\omega)}\right)\phi_m(z',\omega)\psi_m(r,\omega).\end{aligned} \tag{4.3}$$

Noting that a TRM produces an acoustic focus back at the source depth, depth shifting can be achieved by remodulating the relative weighting of the modes according to the term in parentheses. This remodulation strategy requires that the mode amplitudes at depths z' and z'' be known and that the modes be isolated, or uncoupled, so that they may be individually remodulated.

There are 2 basic strategies for isolating the modes so that they may be independently modulated. The first strategy capitalizes on the orthonormality of the modes over a full spanning array, $\frac{1}{\rho_0}\vec{\phi}_n \cdot \vec{\phi}_m = \delta_{nm}$. Here, the dot notation $(\cdot)$ indicates an inner product. The modal amplitudes can be isolated by projecting the individual modal depth dependencies over the measured array data,

$$\frac{1}{\rho_0}\vec{\phi}_n \cdot \vec{P}(z',r,\omega) = \phi_n(z',\omega)\psi_n(r,\omega). \tag{4.4}$$

In this sense, the projection operation acts as a filter. The isolated modal amplitudes can be remodulated and the modal depth-dependence reintroduced. The depth shifted pressure field is synthesized from the depth shifted modal components. It is important to emphasize that projection requires an accurate knowledge of the modes over the entire water column and is only effective in full-spanning applications. Projection will be revisited in Sec. 4.4.1. In the second strategy, mode isolation is achieved by directly localizing the wavenumber characteristics of the modes [3]. By performing a wavenumber analysis, it is possible to isolate the modes according to their discrete propagating wavenumbers. Though this requires the accumulation of pressure fields from many ranges, it has the advantages that it can be applied over a limited aperture TRM and that it results in depth shifting over many ranges (see Fig. 4.1). As a result, the depth shifting procedure developed throughout the remainder of the paper is based on the latter strategy.

4.3 Laboratory demonstration of depth shifting

Depth shifting is now developed in the context of wavenumber isolation based on the mode extraction method of Ref. [3]. Experimental results are presented and used to illustrate the development of the wavenumber isolation depth shifting technique. The development is carried out in three phases: mode extraction, depth shifting, and time-reversal. For the sake of clarity, a discussion of complicating factors that arise during the development is delayed until Sec. 4.4.

4.3.1 Mode extraction from experimental data

The first step of the depth shifting method requires the extraction of the acoustic modes from measured data alone. Applying the mode extraction method of Ref. [3], the modes are extracted from the f-k structure of the waveguide according to their discrete propagating wavenumbers. The f-k structure results from applying Fourier transforms over both time and range to accumulated pressure field data from many ranges,

$$\vec{P}(z',k,\omega) = \mathcal{F}_r\{\mathcal{F}_t\{\vec{P}(z',r,t)\}\} = \sum_{m=1}^{M} \vec{\phi}_m(\omega)\phi_m(z',\omega)\psi_m(k,\omega). \tag{4.5}$$

Here $\mathcal{F}_t\{\}$ and $\mathcal{F}_r\{\}$ indicate the Fourier transforms over time and range respectively. The ranges need not be evenly spaced [14]. The modal wavenumber components of the f-k structure, $\psi_m(k,\omega)$, are peaked about $k(\omega) = k_m(\omega)$. For example, for the case of uniform range sampling at interval dr over a range aperture Δr centered at range r_c in the far-field limit ($\lim_{k_m r\to\infty} H_0^{(1)}(k_m r) \sim e^{ik_m r}$) of a range-independent waveguide (see Eq. 4.2), the modal components of the f-k structure can be approximated by the classical array diffraction result,

$$\psi_m(k,\omega) \approx \frac{i\widetilde{S}(\omega)e^{-ik_m(\omega)r_c}}{4\rho_0\sqrt{k_m(\omega)r_c}} \left(\frac{\sin\left(\left(k_m(\omega)-k(\omega)\right)\frac{\Delta r}{2}\right)}{\sin\left(\left(k_m(\omega)-k(\omega)\right)\frac{dr}{2}\right)}\right). \tag{4.6}$$

In deriving Eq. (4.6) we neglected the effects of cylindrical spreading in applying the range-wavenumber transform. The FFT in range results in a signal-to-noise

ratio (SNR) gain that is proportional to the number of range samples, $\frac{\Delta r}{dr}$ (dr is the nominal sampling interval).

The first phase of the experiment involved the accumulation of pressure field data over range. The experiment was performed in a laboratory waveguide using an ultrasonic transducer (400 kHz bandwidth at a carrier frequency of $600kHz$). The waveguide consisted of approximately 27 mm ($\approx 10.5\ \lambda$) of water over a homogenous sand bottom. Together, the far-field requirement and the finite length of the waveguide constrained the operational range limits to between 400 and 1000 mm ($\approx 160 - 400\ \lambda$).

The experimental configuration is illustrated in Fig. 4.1. A TRM (open black circles) located at $r = 0$ individually recorded pressure fields from the acoustic source at many ranges (closed black circles) all at the same depth, z'. The TRM consisted of $Q = 31$ evenly spaced hydrophone elements spanning most of the water column. Denoting the TRM elements by the index q, the time-domain pressure field measured at element q due to a source at depth z' and range r' is represented by the notation $P_q(z', r', t)$. Panels (a) and (c) of Fig. 4.2 show typical measured time-domain pressure fields (the remaining panels of Fig. 4.2 are discussed later).

Figure 4.3(a) shows the depth averaged modulus of the f-k structure,

$$\frac{1}{Q}\sum_{q=1}^{Q}|\hat{P}_q(z', k, \omega)|,$$

that results from Fourier transforming the measured data over range. The hat notation, $\hat{\vec{P}} \equiv \{\hat{P}_q\}$, indicates that a frequency-wavenumber rotation transformation has been applied to the time-range domain pressure field prior to applying the Fourier transformations. This initial rotation transformation, introduced in Ref. [15], facilitates mode extraction. As discussed in Ref. [3], the rotation transforms the location of the modal wavenumbers in the f-k domain, $k_m(\omega) \rightarrow k_1(\omega) - k_m(\omega)$. In addition to exaggerating the intermodal intervals, this choice of rotation mitigates aliasing of the high order modes. As a result, the range sampling interval can be increased, $dr = \frac{2\pi}{|k_w - k_b|}$, where k_w and k_b are the wavenumbers at the carrier

frequency in the water and bottom respectively. The inverse transformation is well defined and easily applied to the depth shifted pressure field discussed in Sec. 4.3.2.

Most of the modes (appearing as dark curved regions) are localized and distinct from one another in wavenumber. Following the mode extraction method detailed in Ref. [3], the well localized modes were masked and extracted individually. A mask defines a region in the f-k domain containing only one mode that is projected over all TRM elements. The only requirement on the masking procedure is that each mask contain a significant contribution from only one mode. Other than that the mask shape is arbitrary. The mode 7 mask is plotted on Fig. 4.3(a) as an example. Figure 4.3(b) shows the resulting extracted mode 7. Modes 3-10 were successfully extracted in this manner. Because the extraction process involves frequency averaging, the extracted modes are the modes averaged over their respective masks. To denote this averaging, the set of extracted modes are written with an over-line notation, $\overline{\phi}_m(z)$. Due to the frequency averaging associated with the mode extraction process, it is necessary to limit the frequencies spanned by each mask to bandwidths where the modes are weakly frequency dependent. The major advantage of this method is that the modes can be extracted over a partial spanning array (in this case the TRM) using data alone.

Modes 1 and 2 were not well extracted. Due to the limited range aperture of the experiment, the low order modes were not well localized and could not be separated and individually masked. In addition to limiting mode extraction, poor localization resulting from insufficient reange aperture also complicates depth shifting. Poorly localized modes cannot be modulated independently. Due to SNR considerations, the range aperture limitation is likely to be encountered in at sea applications of the depth shifting (DS) method. The issues of determining poorly extracted modes and remodulating poorly localized modes are dealt with in Secs. 4.4.1 and 4.4.2.

4.3.2 Depth shifting experimental data

In addition to facilitating mode extraction, the mode masking technique makes it possible to independently remodulate the modes with only a knowledge of the source depth. The source depth need not be known a-priori. It can be determined by applying mode matching techniques to the set of extracted modes [16, 17, 18]. Once the source depth, z', is determined, the set of extracted modes are used to calculate the modal remodulation coefficients, $\frac{\overline{\phi}_m(z'')}{\overline{\phi}_m(z')}$, (the parentheses term of Eq. (4.3)). Remodulation is accomplished simply by multiplying each mask by its corresponding remodulation coefficient. This is valid since the method has been restricted to weakly frequency dependent regimes. Intermodal f-k structure not included in any masks is irrelevant to far-field modal propagation and is discarded (set to zero). As well, it is possible to discard high order modes for which the TRM depth sampling is inadequate. Figure 4.4 shows the experimental masked f-k structure (compare to Fig. 4.3(a)). Modes 3-10 were remodulated by directly multiplying each mask by its corresponding remodulation coefficient. The independent remodulation of modes 1 and 2 was achieved by the method described in Sec. 4.4.1.

Since the array data now represents an ensemble of acoustic fields excited at depth z'' rather than z', applying the inverse f-k rotation transformation and inverse Fourier transforming the depth shifted f-k structure back to the time and range domains yields depth shifted time domain pressure fields for all original data ranges,

$$\vec{P}(z' \rightarrow z'', r, t) = \widetilde{\mathcal{F}}_r\{\widetilde{\mathcal{F}}_t\{\vec{P}(z' \rightarrow z'', k, \omega)\}\}. \tag{4.7}$$

$\widetilde{\mathcal{F}}_t\{\}$ and $\widetilde{\mathcal{F}}_r\{\}$ indicate the respective inverse Fourier transformations. Panel (b) of Fig. 4.2 shows an experimental depth shifted time domain pressure field from a selected range. The depth shifted pressure field resembles the pressure field measured from a source at the desired depth, z'', at the selected range shown in panel (c), particularly with respect to the early arrivals (low order modes). Close examination of panels (b) and (c) reveals that there is more energy in the high order modes relative to the low order modes in the depth shifted pressure field than in the mea-

sured pressure field. This is likely due to errors associated with the remodulation procedure. As a result, the depth shifted TR pressure more intense sidelodbes in depth than the expected TR result (panel (c)).

4.3.3 TR focusing experimental data

Time-reversing the depth shifted pressure fields produces TR foci at any of the initial source ranges. This result was experimentally verified. Depth shifted TR foci were experimentally observed at all initial source ranges (represented schematically in Fig. 4.1 by the closed gray circles). The foci were measured at selected ranges with a limited aperture Vertical Receive Array (VRA). Figure 4.2(e) shows the experimental TR focus produced by the depth shifted pressure field shown in panel (b). The limited aperture of the VRA resulted in observed clipping at the shallowest and deepest depths. The data source depth and desired focal depth are indicated by (*) and (#) respectively. As a control, this result is compared to the optimal TR foci (panels (d) and (f)) produced by the measured pressure fields from the source and desired depths shown in panels (a) and (c) respectively. Figure 4.5 shows experimental depth shifted TR foci at various depths at a given selected range. Figure 4.6 shows experimental depth shifted TR foci at various ranges at a given desired focal depth.

4.4 Overcoming some complications

Thus far the DS procedure has been developed in the context of ideal conditions; namely, that all modes are well localized and maskable in the f-k domain. In practice, this is often not the case. In this section we discuss methods for dealing with poorly localized modes.

4.4.1 Remodulating coupled modes

As mentioned in Sec. 4.3.1, wavenumber resolution may limit the localization of the low order modes which complicates the masking procedure. The range aperture, Δr, sampled by the data determines the wavenumber resolution,

$$dk = \frac{2\pi}{\Delta r}. \tag{4.8}$$

Adjacent modes (in the f-k domain) for which the intermodal spacing is of the order of the wavenumber sampling interval, dk, cannot be masked, extracted or independently remodulated. Because intermodal spacing decreases with mode order, the lowest order modes are the most prone to the effects of wavenumber resolution limitations.

The simplest strategy for dealing with modes that cannot be separated is to eliminate them from the depth shifted f-k structure entirely. Neglecting the low order modal contributions leads to side lobes in the time-reversed field. The experimental TR field resulting from a depth shifted pressure field from which modes 1 and 2 were eliminated is shown in Figure 4.7. Comparing this to a case where the depth shifted pressure field included properly remodulated contributions from modes 1 and 2 (Fig. 4.2(e)), we see that neglecting the low order modes leads to poor depth shifting results.

In the special case where the depth dependence of the poorly localized modes is known over most of the water column (by most here we mean the portion of the bottom half-space over which the modes can be considered orthogonal to one another), modal wavenumber isolation and remodulation can be achieved by the projection procedure mentioned in Sec. 4.2. However, recalling that the mode extraction procedure of Ref. [3] is also limited by the wavenumber resolution, the depth dependence of poorly localized modes cannot be determined by this technique. Later on in this section we outline an optimization procedure for determining the depth dependence of poorly localized modes from a knowledge of the depth dependence of the known, well-localized modes. Here we continue with the projection remodulation procedure

under the assumption that the depth dependence of the poorly localized modes is known over most of the water column.

Applying the projection of a given mode to f-k domain rotated pressure field, $\vec{P}(z', k, \omega)$, yields

$$\begin{aligned} \Psi_\alpha(k,\omega) &\equiv \frac{1}{\rho_0}\vec{\Phi}_\alpha \cdot \vec{P}(z',k,\omega) \\ &\approx \phi_\alpha(z',\omega)\psi_\alpha(k,\omega), \end{aligned} \tag{4.9}$$

where $\vec{\Phi}_\alpha$ represents an optimized poorly localized mode projected over the TRM. The wavenumber components are then remodulated independently, $\left(\frac{\Phi_\alpha(z'')}{\Phi_\alpha(z')}\right)\Psi_\alpha(k,\omega)$. The depth dependence of the corresponding modes, $\vec{\Phi}_\alpha$, is reintroduced and the components summed with the masked regions of the depth shifted f-k structure. Figure 4.8 shows a schematic of the process applied to experimental data. Panel (a) shows a magnification of the unlocalized low order modes (see Fig. 4.3). Panels (c) and (e) show the modulus of the isolated mode 1 and 2 wavenumber components, $|\Psi_1(k,\omega)|$ and $|\Psi_2(k,\omega)|$ respectively, resulting from the projection procedure. The mode 1 and 2 depth dependences used to make the projections appear in panels (b) and (d). The array diffraction behavior predicted by Eq. (4.6) is apparent for each mode. The projection would not have succeeded in separating modes 1 and 2 had the TRM spanned only a small portion of the water column.

Remembering that mode extraction only works in the case of well localized, maskable modes, we point out that modes 1 and 2 shown in panels (b) and (d) did not result from the original extraction technique. Rather they resulted from an optimization algorithm.

We developed a genetic algorithm [19], based on the orthogonality conditions relating the modes, to construct a small subset of the lowest order modes from a larger subset of known higher order modes. Based on the appearance of the f-k structure (Fig. 4.3) we assumed that modes 4-10 were well extracted, modes 1 and 2 were poorly extracted, and mode 3 was questionable. The optimization cost

functions for modes 1-3 were defined as

$$F_\alpha \equiv |\vec{\Phi}_\alpha \cdot \vec{\Phi}_\alpha - c_{\alpha\alpha}| + \sum_{m=4}^{10} |\vec{\Phi}_\alpha \cdot \vec{\overline{\phi}}_m - c_{\alpha m}|. \tag{4.10}$$

The $\vec{\Phi}_\alpha$ ($\alpha = 1, 2, 3$) represent the optimized modes. $c_{\alpha m}$ and $c_{\alpha\alpha}$ are scalars introduced to account for the fact that the optimization was not performed over the entire half space. Because the TRM spanned most of the water column and did not sample the bottom, the set of known modes are not expected to be strictly orthogonal to one another, nor are they expected to be strictly orthogonal to the optimized modes. These scalars were calculated using a crude environmental model based on minimal knowledge of the environment, namely an estimate of the bottom sound speed, bottom density, and the sound speed profile. The resulting optimized modes (solid black curves) are plotted along with the modes derived from the masking extraction process (gray dashed curves) in Figure 4.9. That the optimized mode 3 so closely resembles the extracted result tells us that the mode 3 mask was valid. Therefore, only modes 1 and 2 were remodulated by projection.

4.4.2 Complications due to weakly excited modes

Depth shifting achieves optimal results when the source excites all propagating modes. Modes whose excitations are too low to appear distinctively in the f-k structure cannot be masked nor extracted. Hence, these modes cannot be included in the depth shifted pressure fields which in turn adversely effects the resulting TR focus. Therefore, the efficacy of the DS algorithm depends on the source depth. Optimal TR focusing results when the source is not near any of the modal nodes. In a Pekeris waveguide, for example, the bottom is an ideal depth for the source.

As well, care must be taken in the case of maskable modes whose excitations are small but measurable. Because the source depth excitation appears in the denominator of the mode remodulation coefficient, $\frac{\overline{\phi}_m(z'')}{\overline{\phi}_m(z')}$, small errors in either the denominator or numerator may result in large errors in remodulation. Remodulation errors resulting in over-excitation are avoided by defining a threshold, β_{max}, for

the remodulation coeffiecients. All coefficients above the threshold are set to zero removing the given mode from the depth shifted f-k structure. Under-excitation is preferable to over-excitation.

4.5 Summary and discussion

Depth shifting of a TR focus over a large portion of a range independent waveguide using broadband sources from many ranges has been experimentally demonstrated at ultrasonic frequencies in a laboratory setting that scales to typical shallow water scenarios. Data from many ranges were used to perform a frequency-wavnumber (f-k) analysis of the waveguide so that the modes could be isolated according to their characteristic wavenumbers. The isolated modes were extracted and remodulated independently resulting in a depth shifting of the waveguide f-k structure. The depth shifted f-k structure was used to produce depth shifted TR foci over the extent of the original range aperture. In cases where the range aperture is large enough to resolve the characteristic wavenumbers of all the modes, it is possible to achieve optimal depth shifted TR focusing with a partial spanning Time-Reversal Mirror (TRM). In cases, such as our experiment, where the range aperture is not adequate to resolve all the modes, optimal depth shifted TR focusing can only be achieved with a TRM that spans most of the water column. We achieved good experimental results using a 90%-spanning TRM.

4.6 Acknowledgements

This chapter, in full, is a reprint of the material as it appears in The Journal of the Acoustical Society of America, 2005, with authors S. C. Walker, Philippe Roux, and W. A. Kuperman. Reprinted with permission from S. C. Walker, P. Roux, and W. A. Kuperman, "Focal depth shifting of a time reversal mirror in a range-independent waveguide," J. Acoust. Soc. Am. **118** (3), 1518-1525 (2005).

Bibliography

[1] W. A. Kuperman, W. S. Hodgkiss, and H. C. Song, "Phase-conjugation in the ocean: Experimental demonstration of an acoustic time-reversal mirror," J. Acoust. Soc. Am **103**, 25-40 (1998).

[2] F. B. Jensen, W. A. Kuperman, M. B. Porter, and H. Schmidt, *Computational Ocean Acoustics*, (AIP New York, 1994).

[3] H. C. Song, W. A. Kuperman, and W. S. Hodgkiss ,"A time-reversal mirror with variable range focusing," J. Acoust. Soc. Am **103**, 3224-3240 (1998).

[4] S. Conti, P. Roux, and M. Fink. "Depth and range shifting of a focal spot in an acoustic waveguide." Applied Phys. Lett. **80**(19), 3647-3649 (2002).

[5] D. Kilfoyle, J. Preisig, and A.B. Baggeroer, "Spatial modulation over partially coherent multiple-input/multiple-output channels," IEEE Trans. Signal Processing, Vol. 51, 794-804, March 2003.

[6] H.C. Song, P. Roux, W.S. Hodgkiss, W.A. Kuperman, T. Akal, and M. Stevenson, "Multiple-input/multiple-output coherent time reversal communications in a shallow water acoustic channel," IEEE J. Oceanic Eng., (in press) 2005.

[7] S. C. Walker, P. Roux, and W. A. Kuperman, "Data-based mode extraction with a partial water column spanning array," J. Acoust. Soc. Am. **118** (3), 1518-1525 (2005).

[8] J. R. Buck, J. C. Preisig, M. Johnson, and J. Catipovic, "Single-Mode Excitation in the Shallow-Water Acoustic Channel Using Feedback Control," IEEE J. Oceanic Engineering **22** 2, 281-291, 1997.

[9] S. N. Wolf, D. K. Cooper, and B. J. Orchard, "Environmentally adaptive signal processing in shallow water," Oceans '93, Engineering in Harmony with Ocean Proceedings, **1**, 99-104, 1993.

[10] P. Hursky, W. S. Hodgkiss, and W. A. Kuperman, "Matched field processing with data-derived modes," J. Acoust. Soc. Am. **109** (4), 1355-1366 (2001).

[11] T. B. Neilsen and E. K. Westwood, "Extraction of acoustic normal mode depth functions using vertical line data," J. Acoust. Soc. Am. **111** (2), 748756 (2002).

[12] George V. Frisk, and James F. Lynch, "Shallow water waveguide characterization using the Hankel transform," J. Acoust. Soc. Am. **76** (1), 205-216 (1984).

[13] G. A. Grachev, "Theory of acoustic field invariants in layered waveguides," Acoust. Phys. **39** (1), 748756 (1993).

[14] L. Greengard, June-Yub Lee, SIAM Review, "Accelerating the Nonuniform Fast Fourier Transform", **46** (3), 443-454, (2004).

[15] Barabara Nicolas, Jerome Mars, and Jean-Louis Lacoume, "Geoacoustical parameters estimation with impulsive boat-noise sources," IEEE J. Oceanic Engineering **28** (3), (2003).

[16] E. C. Shang, "Source depth estimation in waveguides," J. Acoust. Soc. Am. **77**, 1413-1418 (1985).

[17] T. C. Yang, "A method of range and depth estimation by modal decomposition," J. Acoust. Soc. Am. **82** (5), 1736-1745 (1987).

[18] G. R. Wilson, R. A. Koch, and P. J. Vidmar, "Matched mode localization," J. Acoust. Soc. Am. **84** (1), 310-320 (1988).

[19] P. Gerstoft, *SAGA Users guide 4.0, an inversion software package*, An updated version of "SAGA Users guide 2.0, an inversion software package," SACLANT Undersea Research Centre, SM–333, La Spezia, Italy, 1997.

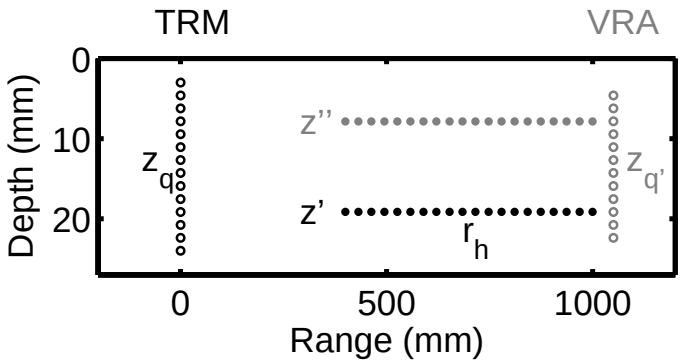

Figure 4.1: Experimental set up. A Time-Reversal Mirror (TRM) composed of Q transducers at depths z_q (black open circles) located at range $r = 0$ individually recorded pressure fields from acoustic point sources (black closed circles) at ranges $r = r_h$ and depth z'. The resulting depth shifted TR foci at depth z'' at selected ranges (gray closed circles) were measured with a Vertical Receive Array (VRA - gray open circles) with elements at depths $z_{q'}$.

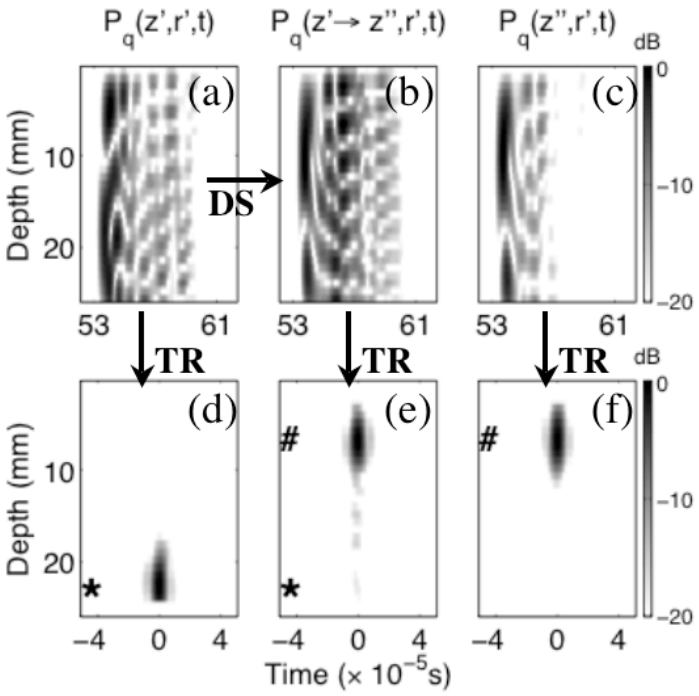

Figure 4.2: Experimental depth shifting (DS) result at a single range. (a) Time domain pressure field, $P_q(z', r', t)$, recorded on the Time-Reversal Mirror (TRM) due to an acoustic source at (r', z') produced (d) Time-Reversal (TR) focus at (r', z'). (b) Depth shifted time domain TRM pressure field, $P_q(z' \rightarrow z'', r', t)$, and (e) resulting TR focus at (r', z''). (c) TRM pressure field, $P_q(z'', r', t)$, due to acoustic source at (r', z'') and (f) its TR focus at (r', z''). $(*)$ and $(\#)$ indicate the source depth, z', and desired focal depth, z'', respectively. $z' \approx 25\ mm$, $z'' \approx 7\ mm$.

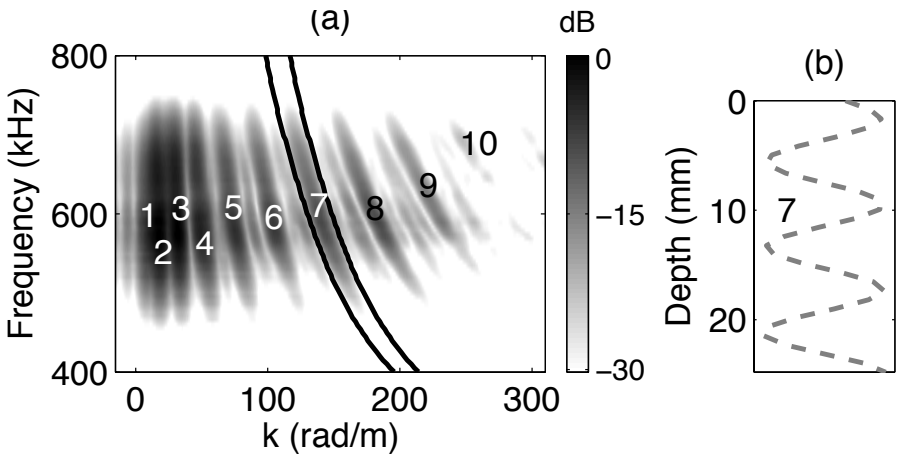

Figure 4.3: (a) Depth averaged modulus of the rotated f-k structure of the experimental waveguide. Propagating modal wavenumbers appear as dark gray curved regions. The modal wavenumbers, which are enumerated for clarity, appear at their rotated values, $k_m(\omega) \rightarrow k_1(\omega) - k_m(\omega)$.Solid black lines indicate the mode 7 mask region. (b) Mode 7 depth dependence extracted from masked region.

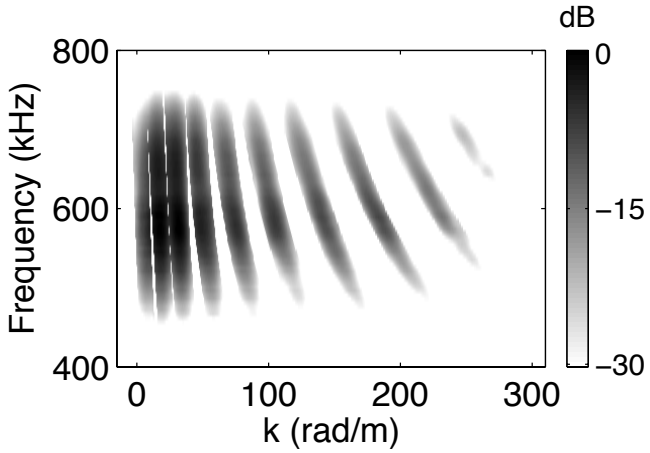

Figure 4.4: Depth averaged modulus of the masked rotated f-k structure of the experimental waveguide. Dark regions indicate the relevant masked modal regions. White regions indicate intermodal modal structure exterior to masks that has been set to zero.

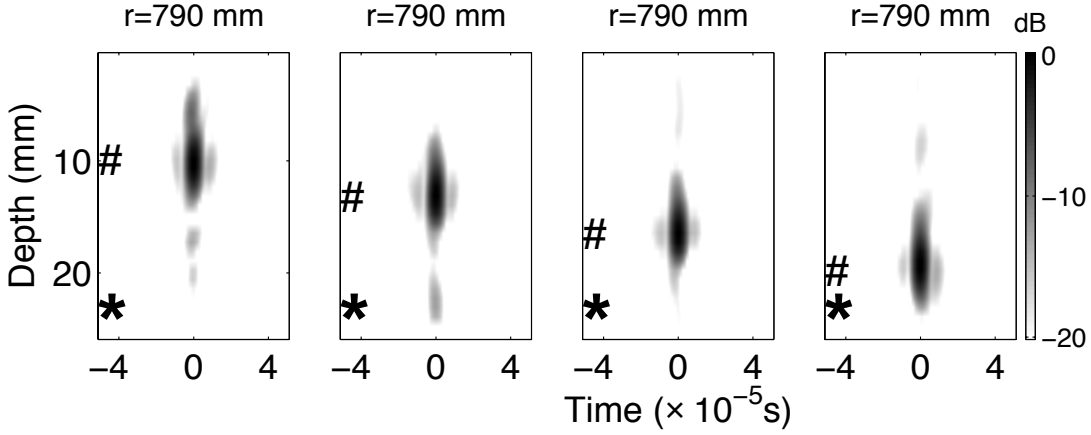

Figure 4.5: Experimental depth shifting results at multiple depths. TR foci produced at several depths at same range. $(*)$ and $(\#)$ indicate the source depth, z', and desired focal depth, z'', respectively.

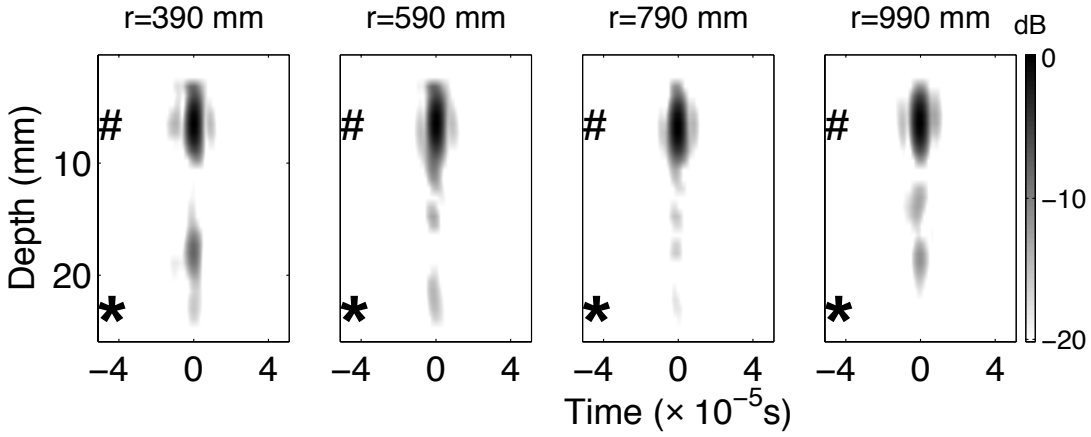

Figure 4.6: Experimental results at a multiple ranges. TR foci produced at several ranges. $(*)$ and $(\#)$ indicate the source depth, z', and desired focal depth, z'', respectively.

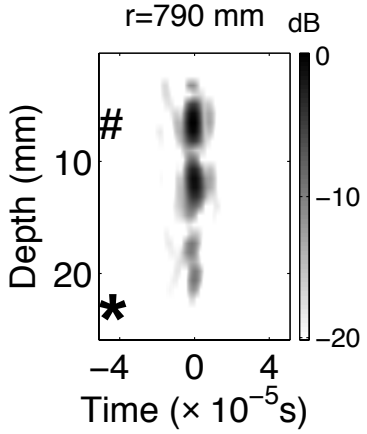

Figure 4.7: Experimental depth shifting result. Time-reversal of depth shifted pressure field from which poorly localized, unmaskable modes 1 and 2 were removed. $(*)$ and $(\#)$ indicate the source depth, z', and desired focal depth, z'', respectively.

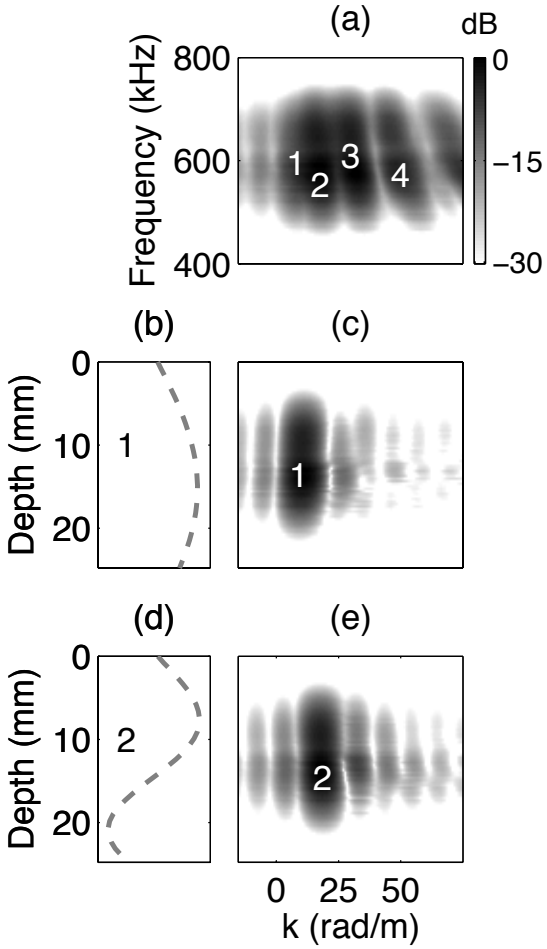

Figure 4.8: Rotated frequency-wavenumber (f-k) structure resulting from projection of optimized modes. (a) Magnification of Fig. 4.3 showing low order modes. (b) Optimized mode 1. (c) Projected mode 1 f-k structure. (d) Optimized mode 2. (e) Projected mode 2 f-k structure.

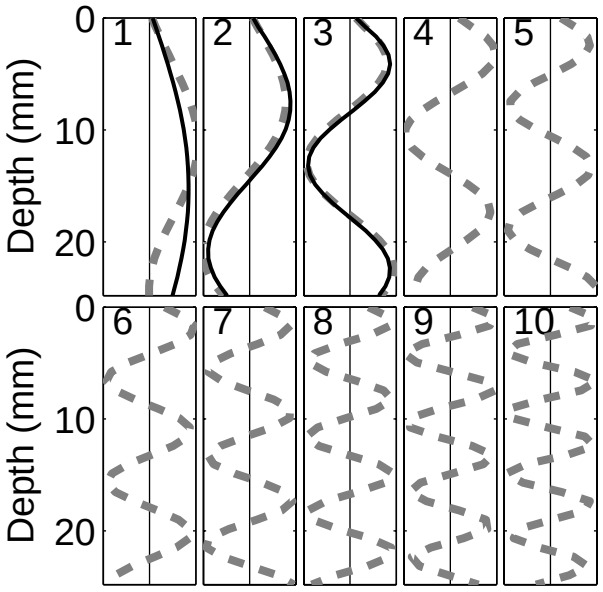

Figure 4.9: Experimental mode extraction results. Modes resulting from mode masking extraction technique (gray dashed lines) are plotted along with optimized modes (dark solid lines). Modes 4-10 were used to optimize for modes 1-3.

Chapter 5

Mode extraction from an accelerating narrowband source in shallow water

abstract

A Doppler-based method for using a moving narrow-band source to extract the modes over a partial-water-column spanning Vertical Line Array (VLA) has been developed. Acceleration due to source motion, ocean currents, wind and waves has a significant degrading impact on frequency estimation. This paper introduces a technique to compensate for the time-dependent Doppler shift from an accelerating source so that the modal depth functions can be extracted from the frequency response. The technique is applied to simulation, and ocean data.

5.1 Introduction

Recently, matrix decomposition methods have been proposed for extracting the depth-dependence of the propagating modes in the shallow ocean from acoustic data measured over a vertical line array (VLA). These methods involve applying an eigenvalue decomposition or a singular value decomposition (SVD) to the spatial

cross-spectral density matrix (CSDM) formed from the measured array data. For these matrix decomposition techniques to be successful the CSDM must be properly conditioned. Conditioning typically involves an averaging over range and/or frequency. References [1] and [2] discuss averaging the measured ambient noise field over time. Reference [3] investigates averaging the signal measured from a moving source over both range and frequency. To ensure proper conditioning, the averaging must be carried out over an effective range aperture which samples several modal interference wavelengths. In the case of a moving source, the range aperture can be constructed by relating received signal times to source ranges. In the case of a broadband signal from a stationary source, an effective range aperture may be constructed by identifying normalized bandwidth with range diversity. Because these methods involve unitary matrix operations, they may only be properly applied to full water column spanning VLAs.

In contrast, the SVD mode extraction technique introduced in Ref. [4] can be applied to the acoustic field received from a broadband source over only a partial-spanning VLA. In this case the measured field is Fourier transformed over both time and range yielding the frequency-wavenumber structure of the waveguide. Because the modes are dispersive, they can be isolated according to their discrete wavenumbers. Constructing the CSDM with only the field from a single isolated mode then renders the CSDM well conditioned for SVD mode extraction. Each well-isolated mode can be extracted in this manner. Interestingly, the conditions for which the modes are expected to be well isolated are identical to the averaging conditions required of the other matrix decomposition methods, namely that the range aperture sample several modal interference wavelengths.

This paper introduces a method for extracting the depth dependence of the modes of acoustic propagation from a moving cw source over a partial water column spanning VLA. As pointed out by Hawker [5] and Schmidt and Kuperman [6], one consequence of the discreteness of the modal wavenumber spectrum is that the modes from a moving source are Doppler shifted relative to the source frequency

in direct relation to their wavenumbers and the source velocity. As a result, each mode from a moving source propagates at a discrete frequency different from the other modes.This paper proposes a method for isolating the modes according to their Doppler shifted discrete frequency spectrum so that they may be extracted individually.

Associating the measured time with the source range, the frequency resolution depends on the range aperture traversed by the source. The modal frequencies will be well resolved when the range aperture approaches several modal interference wavelengths. As an example, a minimum of 5 km of range aperture is required to extract modes 1 and 2 from a 100 Hz source moving in a realistic 150 m deep shallow ocean waveguide. To make this technique practical for ocean applications, a method for measuring and compensating for radial accelerations of the source is presented. The time varying Doppler effects arising from radial accelerations of the source are measured using a time domain least-mean-squares fit to short duration harmonic tones. The resulting information is then applied to compensate for radial accelerations in the received signal. The compensation technique extends the scope of the mode extraction procedure and other wavenumber inversion procedures, such as that developed by Frisk and Lynch [7], to include radially accelerating non-end fire sources subject to currents, wind and waves.

Section 5.2.1 introduces the theory of the mode extraction method applied to a harmonic source traveling at a constant radial velocity. The theory is illustrated with simulation results for the case of a constant radial velocity source in Sec. 5.2.2. In Section 5.3.1, the theory is expanded to include radially accelerating sources. Section 5.3.2 develops the Doppler compensation formalism. The frequency tracking algorithm is presented and applied to a spectral integration simulation of a radially accelerating cw source. The mode extraction procedure is further discussed and simulated mode extraction results are presented. Section 5.4 presents the results of the mode extraction method applied to experimental data measured during the SWellEx experiment conducted in 1996. In that experiment a source was towed

along an isobath following a straight line non-endfire trajectory. The source was broadcasting several cw tones. Compensation and mode extraction results for one of the tones are presented. The final section provides a summary and discussion.

5.2 Mode extraction from a constant radial velocity cw source

The first part of this section summarizes Doppler theory applied to a constant radial velocity cw source in the context of a shallow ocean waveguide in which the acoustic field propagates as a set of depth dependent modes. The second part of this section introduces the method for isolating the modes according to their discrete Doppler-shifted frequency spectrum and the mode extraction procedure.

5.2.1 Theory: Doppler shift of a moving cw source in a range-independent waveguide

According to Doppler theory, the angular frequency, ω, measured by a stationary receiver from a cw acoustic source at angular frequency ω_s traveling at a constant radial velocity, v_s, in an unbounded, homogenous, isotropic medium of sound speed, c, is given by $\omega = \frac{\omega_s}{1+\frac{v_s}{c}}$. This paper focuses on sources, such as ships, that travel at velocities much slower than the speed of sound in the ocean so that $\frac{v_s}{c} \ll 1$. Therefore, for the remainder of this paper, the Doppler shift is applied using the approximation $\omega \approx \omega_s \left(1 - \frac{v_s}{c}\right)$.

As stated in Ref. [8], the pressure field measured at a stationary receiver at depth z_r and range $r = 0$ due to a distant cw source traveling at a constant radial velocity, v_s, in a range-independent waveguide is written

$$P(z_r, z_s, t') = \sum_{m=1}^{M} \phi_m(z_r, \omega_m)\phi_m(z_s, \omega_m)\frac{e^{-i(k_m r_0 + \theta_0)}}{\sqrt{k_m r(t')}} e^{i(\omega_s - \omega_m)t'}. \tag{5.1}$$

In Eq. (5.1) time, $t' = t - t_0$, is measured relative to a specified time, t_0, at

which the phase of the source signal and location of the source are $\theta_0 = \omega_s t_0$, and $r_0 = r(t_0)$ respectively. The source trajectory is given by $r(t') = r_0 + v_s t'$. Each mode propagates at a unique frequency, $\omega_m \equiv \omega_s - k_m v_s$. The modal wavenumbers are given by

$$k_m \approx k_m(\omega_s)\left(1 + \frac{v_s}{u_m}\right) \tag{5.2}$$

to first order in the low velocity limit, $\frac{v_s}{u_m} \ll 1$ [5]. Here $u_m \equiv \frac{d\omega}{dk_m}$ denotes the group velocity of mode m. For a source moving toward the sensor $v_s < 0$, the measured frequency is greater than the source frequency.

5.2.2 Theory: Mode extraction from the frequency response of a moving cw source

Defining

$$a_m(z_s, t') \equiv \phi_m(z_s, \omega_m)\frac{e^{-i(k_m r_0 + \theta_0)}}{\sqrt{k_m r(t')}}, \tag{5.3}$$

and taking the short aperture (in time) Fourier transform of Eq. (5.1) yields

$$\widetilde{P}(z_r, z_s, \omega) = \sum_{m=1}^{M} \widetilde{P}_m(z_r, z_s, \omega), \tag{5.4}$$

where

$$\widetilde{P}_m(z_r, z_s, \omega) = \phi_m(z_r, \omega_m)\left(\frac{1}{\sqrt{2\pi}}\int_0^{t_1} a_m(z_s, t')e^{i(\omega_m - \omega)t'}dt'\right) \tag{5.5}$$

is the short time aperture Fourier transform of the mode m component. Figure 5.1 shows a schematic of the magnitude of the pressure field frequency spectrum (Eq. (5.4)) for an approaching constant velocity source. Though all formalism is developed in terms of the angular frequency, all figures are given in units of Hz for convenience. The 3 propagating modes are shifted to higher frequencies (indicated by $f1$, $f2$, and $f3$) than the source frequency (fs). The pressure frequency spectra of the individual modal components are also plotted for the purposes of illustration. Comparing Eq. (5.5) to Fig. 5.1 demonstrates that the mode m component dominates in the vicinity of its modal frequency. This suggests the possibility of

extracting its depth dependence by selecting the appropriate frequency component of the spectrum projected over the VLA.

Figure 5.2 shows the absolute value of a simulated pressure frequency response projected over the VLA. The normalized pressure response summed incoherently over the VLA elements (black line) is superimposed on the image. The simulation was carried out for a source moving toward the VLA at 4 $\frac{m}{s}$ along an endfire trajectory at a constant depth of 145 m in a 150 m deep Pekeris waveguide using a spectral method [8]. The water sound speed, water density, bottom sound speed, and bottom density were $c_w = 1500\ \frac{m}{s}$, $\rho_w = 1026\ \frac{kg}{m^3}$, $c_b = 1800\ \frac{m}{s}$, and $\rho_b = 1800\ \frac{kg}{m^3}$, respectively. The VLA consisted of 28 elements evenly spaced between 10 m and 145 m of depth. Evident are 11 propagating modes, with mode 11 appearing at the lowest frequency. Since the source is moving toward the array the modes are shifted to higher frequencies than the source frequency, $fs = 100.17\ Hz$. The frequency resolution is such that modal frequencies for modes 5 -11 appear well-isolated and their depth dependencies can be extracted. In contrast, the frequency resolution is not adequate to resolve the modal frequencies of modes 1-4. Interestingly, it is the range aperture traversed by the source that determines the resolution of the Fourier frequency response,

$$\left.\begin{aligned} d\omega &= \tfrac{2\pi}{\Delta t}, \\ \Delta r &= |v_s \Delta t|, \\ d\omega &\ll |(k_m - k_{m+1}) v_s| \end{aligned}\right\} \longrightarrow \Delta r \gg \frac{2\pi}{|k_m - k_{m+1}|}. \tag{5.6}$$

In order to resolve modal frequency m from modal frequency $m+1$, the source must cover a distance significantly longer than the mode m mode $m+1$ interference wavelength regardless of the source velocity. Figure 5.3 shows the minimum range aperture (as defined by resolution relations (5.6)) needed to resolve the theoretical modes of the simulation. The range aperture of the simulation was 2400 m. Because the modal components are monochromatic and coherent in the constant velocity case, the Fourier analysis results in a coherent summation of the modal depth dependencies. The gain in intensity of the modes at their respective frequency max-

ima is directly proportional to the size of the time aperture used to calculate the frequency response. As a result, SNR increases with time aperture. SNR, then, is velocity dependent. For a given range aperture, the SNR increases inversely to the source velocity, $SNR \propto \Delta t = \frac{\Delta r}{v_s}$. For a large time aperture with high SNR it is possible to extract the modes simply by isolating the depth dependence at a given frequency maximum. Returning to Eq. (5.5), the depth dependence will be multiplied by a complex phase that is constant over depth. A method for removing the phase and mode extraction results will be given in the next section.

5.3 Mode extraction from a radially accelerating cw source

In light of the frequency resolution arguments outlined in the last section, effective mode isolation in shallow ocean applications requires several kilometers of range aperture. Because the ocean is such dynamic environment with waves, wind, and currents, it is necessary to adapt the basic technique to radially accelerating sources, particularly if the end goal is mode extraction from sources of oppportunity. This section extends the mode extraction technique to radially accelerating sources. It is divided into three subsections. In part 5.3.1 modal theory is developed in the context of a radially accelerating source for which the modal Doppler shift varies with time. Part 5.3.2 of this section introduces a method for detecting and compensating for the time varying Doppler effects associated with radial acceleration. Section 5.3.3 presents simulated compensation and mode extraction results and further develops the extraction procedure.

5.3.1 Theory: Modal Doppler shifts from a radially accelerating source

As shown in Sec. 5.2, the pressure field measured by a stationary sensor from a constant radial velocity source can be written analytically. For the case of a source that accelerates arbitrarily in the radial direction, an analytic solution is not always possible. Though a time domain expression for the case of a constant velocity, nonendfire source has been derived [5, 8], this paper treats the case of arbitrary acceleration. The difficulty in treating the arbitrary acceleration case derives from the dependence of the modal wavenumbers and the associated set of depth dependent orthogonal mode functions, on the radial velocity of the source. For a radially accelerating source, the modal wavenumbers and depth functions become implicit functions of time. Intuitively, it seems logical that a solution of the form

$$P(z_r, z_s, t') \approx \sum_{m=1}^{M} \phi_m(z_r, \widetilde{\omega}_m(t'))\phi_m(z_s, \widetilde{\omega}_m(t'))\frac{e^{i(\omega_s t' - k_m(t')r(t') - \theta_0)}}{\sqrt{k_m(t')r(t')}} \tag{5.7}$$

should exist, where the $\widetilde{\omega}_m(t')$ represent the set of frequencies at which the mode depth functions are to be evaluated. It must be stressed that determining the modal wavenumbers and the set of associated depth functions in the arbitrary acceleration case is generally not possible analytically.

However, it is not the aim of this paper to derive an expression for the time domain pressure field from an arbitrarily accelerating source. Equation (5.7) serves merely to illustrate the nature of the proposed problem. Rather, the aim is to extract the depth dependent mode functions from a Fourier frequency analysis of the measured time domain field. In analogy to Eqs. (5.3) - (5.5), the short time aperture Fourier frequency response of the radially accelerating source is given by

$$\widetilde{P}(z_r, z_s, \omega) = \sum_{m=1}^{M} \widetilde{P}_m(z_r, z_s, \omega), \tag{5.8}$$

where

$$\widetilde{P}_m(z_r, z_s, \omega) = \left(\frac{1}{\sqrt{2\pi}} \int_0^{t_1} a_m(z_r, z_s, t') e^{i((\omega_s - \omega)t' - k_m(t')r(t'))} dt'\right) \tag{5.9}$$

is the short time aperture Fourier transform of the mode m component, and a_m is defined by

$$a_m(z_r, z_s, t') \equiv \frac{\phi_m(z_r, \omega)\phi_m(z_s, \omega)}{\sqrt{k_m(t')r(t')}} e^{i\theta_0}. \tag{5.10}$$

It is illustrative to decompose the range into a component associated with uniform motion at velocity $r_0 + v_c t$ and an acceleration component, $\hat{r}(t')$, such that $r(t') = r_0 + v_c t' + \hat{r}(t')$. Here v_c is defined to be the average velocity on the interval. Additionally, the acceleration component satisfies the following boundary conditions: $\hat{r}(0) = 0$, and $\dot{\hat{r}}(t_c) = 0, 0 \leq t_c \leq t_1$. The range has been written in this form for convenience as will be made apparent in Sec. 5.3.2. Notice that this set of equations is encumbered by the implicit time dependence of the wavenumbers. The time dependence is made explicit to emphasize the dynamic response of the modal wavenumbers which vary with time as a function of the radial source velocity. Expansion (5.2) is still valid in the accelerating case in the limit, $\frac{|v_s(t')|}{u_m(t')} \ll 1$. Identifying the radial source velocity as the first time derivative of the source range, $v_s(t') = \dot{r}(t') = v_c + \dot{\hat{r}}(t')$, where the dot notation signifies the first derivative with respect to time, the modal wavenumbers are approximately

$$k_m \approx k_m(\omega_s)\left(1 + \frac{v_c}{u_m} + \frac{\dot{\hat{r}}(t')}{u_m}\right). \tag{5.11}$$

Because modal depth dependence is relatively insensitive to small fluctuations of the modal wavenumbers, in the low source velocity limit the modal depth functions can be taken as constant over the time aperture of interest. For the remainder of the paper, the mode functions are approximated by their narrowband responses at the source frequency, $\phi_m(z) \equiv \phi_m(z, \omega_s)$.

Referring to Eq. (5.9) for a radially accelerating source, because the phases of the modal components of the time domain pressure field are no longer linear with time, there is no unique constant frequency for each mode throughout the duration of the time aperture. As a result the modal components do not sum coherently over the time aperture, and the frequency response of the pressure field no longer responds as a superposition of well defined harmonic components such as is shown in Fig.

5.1. Rather, the frequency response appears "smeared" or broadened. Figure 5.4(a) shows a schematic of the magnitude of the pressure field frequency response for an approaching source under constant acceleration. Because the source is approaching, its velocity is negative over the time aperture and positive acceleration manifests as a decrease in the magnitude of the radial speed. The initial frequencies of the 3 propagating modes at the beginning of the time aperture are indicated by $f1$, $f2$, and $f3$. As the source velocity increases, the modal frequencies decrease, resulting in a broadening of the frequency responses of the modal components. As a consequence, the modal depth functions are not be identifiable as isolated regions such as in Fig. 5.2.

5.3.2 Detecting and compensating for time varying Doppler effects

The modal frequency broadening arising from the time varying Doppler effects associated with a radially accelerating source prevents direct application of the mode extraction strategy outlined in Sec. 5.2.2. The mode m instantaneous frequency response, $\varpi_m(t)$, is defined as the time derivative of the mode m phase progression from Eq. (5.9),

$$\begin{aligned} \varpi_m(t) &\equiv \frac{d}{dt}\left(\omega_s t - k_m(t)r(t)\right) \\ &= \omega_s - \dot{k_m}(t)r(t) - k_m(t)\dot{r}(t). \end{aligned} \tag{5.12}$$

The frequency broadening is quantifiable in terms of the right-most pair of terms in the last equation. Expanding out these terms and substituting Eq. (5.11) yields

$$\dot{k_m}(t)r(t) + k_m(t)\dot{r}(t) = \left(\frac{r(t)\ddot{\hat{r}}(t) + v_s^2(t)}{u_m} + v_s(t)\right) k_n(\omega_s). \tag{5.13}$$

For a source moving at $-3\ \frac{m}{s}$ at a range of 4 km at time $t = 0$ and constantly accelerating to $-1\ \frac{m}{s}$ at time $t = 600\ s$, assuming a modal group speed of 1000 $\frac{m}{s}$,

$$\left| \left(\frac{r(t)\ddot{\hat{r}}(t) + v_s^2(t)}{u_m}\right) / v_s(t) \right|_{max} < 0.01. \tag{5.14}$$

Here *max* refers to the maximum value over the time aperture. Thus, in the low velocity limit the instantaneous modal frequencies respond in direct relation to the radial source velocity to a high degree of accuracy. Within the error associated with Eq. (5.14) the modal frequency responses share the same functional form with respect to time,

$$\begin{aligned} \varpi_m(t) &= \omega_s + k_m v_s(t) \\ &= \omega_s + k_m v_c + k_m \dot{\hat{r}}(t). \end{aligned} \tag{5.15}$$

Our aim is to use the functional form of the modal Doppler shifts to compensate for the time varying Doppler effects. In order to make practical use of Eq. 5.15, we introduce a frequency-tracking technique for measuring the time evolution of the instantaneous frequency response of an experimental pressure field in a multipath environment. The basic component of the technique is a time domain least mean squares fit to short time duration intervals of the measured signal. To implement the fit, the measured time domain pressure field is band-pass filtered to remove any strong frequency components not related to modal propagation arising from the source at frequency ω_s. The filtered field on the i^{th} VLA element, $P_i(t)$, is decomposed into time windows of duration δt_{win} at intervals of Δt_{samp}. The j^{th} time window sampled at time $t = j\Delta t_{samp} \equiv t_j$ is denoted by $P_i(t_j; t_j + \delta t_{win})$. Each window is assigned to the array $D_{ij}(t'') = P_i(t_j; t_j + \delta t_{win})$. Here the $t'' = t - t_j$ is the local time relative to the start time of each time window. Indices $i = 1, 2, \ldots I$ and $j = 0, 1, \ldots J$ denote the the particular VLA array element and time window, respectively. Each time window is fit to a 2 parameter model, $\sin(\hat{\omega}t'' + \alpha)$, for each element using a least mean squares method. For high SNR in the $\delta t_{win} \to 0$ limit, this procedure is equivalent to sampling the instantaneous time derivative of the phase of the received signal at times t_j. For the fit to be valid, δt_{win} must be small enough that the frequency content is nearly monochromatic over the duration of the window.

The appropriate window duration and sampling interval are determined by the

dynamics of the measured pressure field. As shown above, the time domain pressure field is composed of several time varying monochromatic modal frequency components whose instantaneous frequency distribution depends on the instantaneous wavenumbers and instantaneous source velocity. Interference among these frequency components results in beating of the time domain signal. In order for the monochromatic assumption to be valid, the window duration must be smaller than the characteristic beating duration, Δt_b. The beating duration depends on the maximum frequency interval between the highest and lowest modal frequency components, $\Delta t_b \approx \frac{2\pi}{\left|(\frac{1}{c_b}-\frac{1}{c_w})\omega_s v_s\right|_{max}}$, where c_b and c_w are sound speeds characterizing acoustic propagation in the bottom and water respectively. The sampling interval must be small enough that it adequately samples the macroscopic frequency behavior. However, oversampling causes no error, so Δt_{samp} may be as small as computation power allows.

The minimization function is defined as

$$\chi_{ij}(\hat{\omega},\alpha) = \int_0^{\Delta t_{win}} \left|D_{ij}(t'') - \mathcal{E}_{ij}(t'')\sin\left(\hat{\omega}t'' + \alpha\right)\}\right|^2 dt'' \tag{5.16}$$

where $\hat{\omega}$ and α are the fit parameters. $\mathcal{E}_{ij}(t'')$ is defined as the envelope of $D_{ij}(t'')$. Including the envelope accounts for modulations caused by the beating and thereby improves ability of the 2 parameter model to fit the data. The value of the frequency parameter, $\hat{\omega}_i(t_j)$, that minimizes χ_{ij} on element i for window j, is regarded to be the instantaneous frequency response of the pressure field on the i^{th} element sampled at times t_j. The phase parameter, α, is ignored. Signal minima arising from destructive interference among the modal frequency components can lead to unacceptable mismatch and poor values for the instantaneous frequency response of a given element at various times. Sampling the signal over depth ensures that, for any particular time,t_j, some elements will not experience a destructive interference minima. Such redundancy allows for a variety of schemes for determining the instantaneous frequency response at each time sample, ranging from an averaging of the individual element fits to acceptance of only the best fit. The multi-element best fit frequency at time t_j is denoted by $\hat{\varpi}(t_j)$.

Figure 5.4 shows the results of the frequency tracking procedure applied to simulation for a source moving toward the VLA at 4 $\frac{m}{s}$ along a nonendfire trajectory at a constant depth of 5 m in the same Pekeris waveguide environment from Sec. 5.2.2. The VLA elements are also at the same depths. The source range and radial velocity trajectories are plotted in Fig. 5.5(a) and 5.5(b). As the source is not traveling along an endfire trajectory, the radial velocity varies with time. The frequency tracking technique was applied using a time window duration of $\delta t_{win} = 2\ s$ and a sampling interval of $\Delta t_{samp} = 1\ s$. The thick black line in Fig. 5.5(c) is the frequency tracking result. It is plotted along with the theoretical time dependent modal frequencies. There is one thin black curve for each of the 11 time varying modal frequencies. The fluctuations in the frequency tracking result are physical and arise from the complex dynamics of the interference among the modal frequencies. Notice the fluctuations fall within the spread of the theoretical modal frequencies and diminish as the spread diminishes.

Interpolating the frequency track result to the sampling rate of the pressure field yields the desired functional form needed to perform the compensation. The interpolated measured frequency response is indicated by $\hat{\varpi}(t')$. Choosing a reference frequency, ω_c, such that $\hat{\varpi}(t') = \omega_c + \hat{\delta\omega}(t')$ the compensation function is defined

$$\mathcal{F}_{\pm}(\gamma, t') = e^{\pm i\gamma\hat{\Theta}(t')} \tag{5.17}$$

where $\hat{\Theta}(t')$ represents the deviation in phase as a function of time from the linear phase progression of monochromatic component at frequency ω_c,

$$\hat{\Theta}(t') = \int_0^{t'} \hat{\delta\omega}(t'')dt''. \tag{5.18}$$

The $\pm$ notation relates to the ambiguity in the measured frequency response arising from a degeneracy with respect to the source velocity. Both an approaching source ($v_s < 1$) and a receding source ($v_s > 1$) can generate the same measured response. Knowledge of the source frequency or travel direction breaks the degeneracy. The parameterization γ is included to make the connection to Eq. (5.15),

$$\begin{array}{rcl} \varpi_m(t) & \leftrightarrow & \hat{\varpi}(t) \\ \Downarrow & & \Downarrow \\ k_m v_c & \leftrightarrow & \gamma(\omega_c - \omega_s) \\ k_m \hat{r}(t) & \leftrightarrow & \gamma\hat{\Theta}(t) \end{array} \tag{5.19}$$

Though the choice for ω_c is arbitrary, we define it so that the total phase change of the compensation, $\hat{\Theta}(t_1) - \hat{\Theta}(0)$, is zero for $\gamma = 1$,

$$\omega_c = \frac{1}{t_1}\int_0^{t_1} \hat{\varpi}(t')dt'. \tag{5.20}$$

Written this way, ω_c is the average measured frequency on the time aperture. This choice for ω_c is based on the physics underlying the method. Returning to Eq. (5.15), in this form, ω_c can be thought of as the frequency response of the source at the average velocity on the time aperture, v_c. It is important to make the connection to average velocity. In the low velocity limit, where the modal wavenumbers are nearly constant over the time aperture, the total phase difference is determined by the range aperture traversed by the source. Choosing ω_c to be greater than the average on the interval results in a greater total phase change in the compensation function than is warranted by the physics; doing so effectively creates more range aperture than was actually traversed and is therefore unphysical. Likewise, choosing ω_c to be less than the average has the effect of reducing the aperture and is counterproductive.

In analogy with Eqs. (5.8) and (5.9), the short time aperture Fourier response of the compensated field is given by

$$\hat{\tilde{P}}(z_r, z_s, \omega, \gamma) = \sum_{m=1}^{M} \hat{\tilde{P}}_m(z_r, z_s, \omega, \gamma), \tag{5.21}$$

where

$$\hat{\tilde{P}}_m(z_r, z_s, \omega, \gamma) = \left(\frac{1}{\sqrt{2\pi}}\int_0^{t_1} a_m(z_r, z_s, t') e^{i\left((\omega_s - k_m v_c - \omega)t' - k_m \hat{r}(t') \pm \gamma\hat{\Theta}(t')\right)} dt'\right) \tag{5.22}$$

is the short time aperture Fourier transform of the mode m component. The factor a_m is given by Eq. (5.10). As demonstrated by Eqs. (5.15) and (5.19), $\hat{\Theta}(t') \propto \hat{r}(t')$.

Therefore, there exists a value of the compensation parameter, $\gamma = \Gamma_m$, for which $k_m \hat{r}(t') \pm \gamma \hat{\Theta}(t') \approx 0$ is true for all t', rendering the frequency response of mode m constant over the duration of time aperture. Of course, this value of γ does not render the other modal frequency responses constant.

The effects of the compensation procedure are displayed schematically in Fig. 5.5. Recall, the short time aperture Fourier transform of the pressure field, $P(t)$, from a constant radial acceleration source in a 3 mode environment is shown in Fig. 5.5(a). The frequency response is a superposition of broadened modes. Fig. 5.5(b)-(d) shows the short time aperture Fourier transforms of the compensated pressure fields, $P(t)\mathcal{F}_{\pm}(\Gamma_1, t)$, $P(t)\mathcal{F}_{\pm}(\Gamma_2, t)$, and $P(t)\mathcal{F}_{\pm}(\Gamma_3, t)$, respectively. Each compensation transforms the pressure field so as to render the chosen modal frequency response constant. A Fourier analysis results in a coherent summation of the depth dependence of the chosen mode over the time aperture.

5.3.3 Phase compensation and mode extraction from a simulated radially accelerating source

Having developed the formalism of the phase compensation, we apply the procedure to the simulated pressure field from a radially accelerating source. The simulation is identical to that of Sec. 5.3.2 to which the frequency tracking technique was applied. The time aperture used for the following development corresponds to the first 750 s of Fig. 5.4. The frequency tracking results (solid dark curve), $\hat{\varpi}(t')$, over the time aperture are shown in Fig. 5.6(a). For convenience, all figures are plotted in frequency and *cycles* rather than angular frequency and phase. The dashed line indicates the average frequency over the time aperture, ω_c. The resulting time dependent phase deviation, $\hat{\Theta}(t')$, is plotted in Fig. 5.6(b). Notice that because the phase deviation is calculated with respect to the average frequency over the time aperture, the total phase deviation is zero at the end of the aperture. Fig. 5.7 shows the frequency response resulting from a compensated pressure field (black

curve) summed incoherently over depth, $\sum_q \left|\hat{\widetilde{P}}(z_q, z_s, \omega, \gamma)\right|$ (for receiver depths z_q). The compensation parameter is $\gamma = 0.93$. The uncompensated frequency response, $\sum_q \left|\widetilde{P}(z_q, z_s, \omega)\right|$, is plotted for comparison (gray curve). Because the acceleration is mild, this value of the compensation parameter results in the unbroadening of frequency responses of several of the modes. The mode 10 response is the best for the purposes of mode extraction. Figure 5.8 demonstrates the behavior of the frequency response as a function of compensation parameter. The compensated pressure field frequency response is imaged as a function of the compensation parameter, γ. As γ increases, the modal frequency responses are sequentially unbroadened, or made constant over the time aperture. The dark regions correspond to optimal compensations for the respective modal frequency responses. The corresponding modes are indicated. By determining the value of the compensation parameter yielding the optimal response for mode m, $\gamma = \Gamma_m$, the corresponding wavenumber can be calculated in the low radial source velocity limit,

$$k_m = \Gamma_m \frac{(\omega_c - \omega_s)}{v_c}. \tag{5.23}$$

Assuming that the source frequency, ω_s, and average velocity over the time aperture, v_c, are known, the wavenumber can be deduced from Fig. 5.8. Even without knowledge of ω_s and v_c, information about the wavenumbers can be deduced. Namely, the ratios between the wavenumbers are given by the the ratios between the optimal compensation parameters,

$$\frac{k_m}{k_n} = \frac{\Gamma_m}{\Gamma_n}. \tag{5.24}$$

However, even for the case of a simulation with high SNR, the task of determining the optimal compensation parameter for each mode is difficult. As seen in Fig. 5.8, determining the local maximum for each mode with respect to γ involves uncertainty on the order of the spacing between the maxima. This translates to an uncertainty in wavenumber on the order of the inter wavenumber intervals.

Though it would be beneficial to deduce the wavenumbers from the compensation procedure, it is not necessary for extraction of the modal depth functions.

All that is required for extraction is that the frequency response of a given mode be highly peaked. Figure 5.9 demonstrates the relationship between modal depth dependence and the frequency response for different values of the compensation parameter. These images show the absolute value of the frequency response projected over the VLA. For each image, the normalized frequency response summed incoherently over the VLA (black line) for the given compensation parameter is superimposed. Figure 5.9(a) shows the optimal compensation for mode 10, though the mode 9 and mode 11 modal frequencies and depth dependencies are also well resolved. The mode 7 modal frequency and depth dependence is well resolved in the compensation of Fig. 5.9(b). In Fig. 5.9(c), the compensation parameter is too high to resolve any of the modes.

Returning to Fig. 5.9(a), the mode 10 depth dependence can be extracted by isolating the frequency component corresponding to the maximum of its compensated frequency response projected over the VLA. This procedure can be applied to all modes that are well resolved and isolated from the neighboring modes for some value of the compensation parameter. As mentioned in Sec. 5.2.2, the depth dependence obtained in this manner will in general result in the a complex vector of the form $e^{i\theta}\phi_m(z_q)$ for each element of the array. The top left panel of Figure 5.10 shows the real and imaginary components of the complex mode vector resulting from the mode extraction procedure. The top right panel shows the phase "unwrapped" in units of π. For a vertical array, the phase associated with the modal depth dependence of a well resolved and isolated mode is expected to be constant. The staircase structure of the unwrapped phase indicates that the array is vertical and that the modal depth dependence is free from interference from neighboring modes. The phase can be easily compensated by multiplying the complex mode vector by $e^{-i\delta\theta}$ where $\delta\theta$ is the modulus of θ with respect to π for one or several of the vector components. The bottom panels of Fig. 5.10 show the results of applying the transformation to the complex vector of the top panels. Mode extraction results for modes 3 - 11 are plotted in Fig. 5.11. The dark solid curves are the mode extraction results. The

theoretical modes (dashed curves) are plotted for comparison. As mentioned in Sec. 5.2.2, the range aperture was insufficient to successfully resolve, isolate, and extract modes 1 - 4.

5.4 Experimental mode extraction from a radially accelerating source

In this section the compensation and mode extraction procedure are applied to experimental data. The data were recorded during the SWellEx-96 experiment conducted near San Diego, California in the spring of 1996. During this experiment, an acoustic cw source was towed along an isobath of a mildly sloping environment. The water depth was approximately 210 m. The data were recorded by a vertical line array composed of 64 elements evenly distributed over the bottom half of the water column, between 94 m to 210 m. This analysis considers only 21 of the 64 elements at depth intervals of approximately 5 m over the extent of the VLA. Matched field processing (MFP) was successfully employed [9] using a set of normal modes calculated from the knowledge of the measured environmental parameters [11]. These modes, then, are used as a benchmark for our mode extraction technique results.

The source tow track and the surrounding bathymetry are displayed in Fig. 5.12(a). The source tow, indicated by the dark thick solid line, began about 8 km from the VLA. The VLA is indicated by one of the stars. Other measurement devices not related to this analysis are also indicated with stars. The source followed a nonendfire approximately straight trajectory at a velocity of about 2 $\frac{m}{s}$. The velocity varied over the track. The closed circles along the source trajectory indicate 5 minute intervals. The source depth was approximately 9 m. The source range is shown as a function of time in Fig. 5.12(b). The gray line is the entire source track while the thick black line indicates the part of the track used for mode extraction in the following analysis. Again, the closed circles indicate 5 minute intervals. The time

aperture used for the mode extraction is 25 minutes. During this time the source traversed about 3.5 km. The set of benchmark wavenumbers generated from the normal mode method were used to estimate the minimum amount of range aperture needed to resolve and extract the propagating modes. Referring to Fig. 5.12(c), the range aperture is sufficient to extract modes 7-12 under the assumption that at least 2 modal interference wavelengths of aperture are required for resolution of adjacent modes.

The result of the frequency tracking technique applied to the time aperture of the experimental data is plotted in the top panel of Fig. 5.13. The gray curve is the frequency tracking result, $\hat{\varpi}(t')$. The dashed line marks the average frequency, ω_c, over the time aperture. The fluctuations are too large to be explained merely by beating of the modal frequencies. However, because the frequency tracking algorithm yielded the same results for several combinations of δt_{win} and Δt_{samp}, we must conclude that the fluctuations do not result from random errors associated with the fit. In other words, the fluctuations must be physical. Interestingly, the magnitude of the fluctuations corresponds to source velocity fluctuations of about $\pm 20\ \frac{cm}{s}$ and the dominant periodicity of the fluctuations is about 8 s. This suggests that the fluctuations could be the result of wave action on the motion of the source. The bottom panel shows the resulting time dependent phase deviation, $\hat{\Theta}(t')$. The source frequency was $\omega_s = 109.00\ Hz$. The frequency response (black curve) for a selected value of the compensation parameter summed incoherently over depth, $\sum_q \left|\hat{\tilde{P}}(z_q, z_s, \omega, \gamma)\right|$ is plotted in Fig. 5.14 along with the uncompensated result (gray curve). Because the radial acceleration is very mild over the time aperture, the frequency response improvement is not as drastic as in the simulation of the last section. However, the displayed compensation still results in a substantial gain in SNR for a few of the modal components. The absolute value of the frequency response for the same value of the compensation parameter projected over the VLA is shown in Fig. 5.15. Again, the normalized frequency response summed incoherently over the VLA (black line) for the given compensation parameter is superimposed.

The depth dependence of mode 9 is well resolved. Modes 8 and 10 on either side are also resolved. Figure 5.16 shows the mode extraction results. The data derived modes projected over the VLA are indicated by black curves. They are plotted against the calculated benchmark normal modes (dashed lines) for comparison. A few data derived mode results are plotted in each panel. Each data derived mode was extracted for a different value of the compensation parameter. As expected, the range aperture was insufficient to extract the low order modes. In addition to the limitations posed by the short aperture, the low order modes were not highly excited by the shallow source. Because the extracted mode functions are known only over the VLA, they have been normalized to unity over the VLA. This limitation is unavoidable in partial spanning applications and can lead to normalization mismatch between the low order and high order modes.

5.5 Summary and discussion

A method for self-adaptively extracting the modal depth functions projected over a partial spanning vertical line array (VLA) of acoustic sensors from a radially accelerating acoustic cw point source has been presented. Doppler effects arising from the source motion break the degeneracy of the modal frequency response so that each mode propagates at a distinct frequency from the other modes. For a constant velocity source, the modal frequencies remain constant in time. As a result, coherent processing methods such as the Fourier transform lead to high SNR gains for the modal depth functions. Modes for which the range aperture is long enough can be resolved in the frequency domain and isolated and extracted individually. However, radial source accelerations add a time variation to the modal frequencies reducing the SNR and resolution. Radial accelerations become an issue in at sea applications where the required range aperture can be on the order of kilometers. In order to make this technique practical, a method for compensating for the time varying Doppler effects was developed in conjunction with the mode extraction

technique. The acceleration induced Doppler dynamics are measured with a time domain least mean squares fit to short duration harmonic tones. This information makes it possible to transform the measured time domain pressure field so that one or more of the modal frequencies remain constant in time.

The technique was successfully applied to both simulation and experimental data. The depth dependent mode functions projected over a partial water column spanning VLA were successfully extracted in both instances, limited only by the resolution restrictions related to the range aperture traversed by the source. In both cases, the range aperture was insufficient for extraction of the low order modes. Though this technique may only yield a fraction of the modal depth functions over a portion of the water column, there is still a potential for application to coherent matched field processing [10] and matched mode processing [12] techniques. For example, this technique in conjunction with the optimization scheme presented in Ref. [10] (which assumes *a-priori* knowledge of the sound speed profile of the water column) could be used to determine the full set of full-spanning modal depth functions and their corresponding wavenumbers. In a similar fashion, an accurate knowledge of the modal depth functions can serve as the basis for bottom property inversion techniques. Though the frequency response analysis in this work has been developed in the context of Fourier decompositions, other methods for determining the frequency response can be used. For instance, because the compensation procedure renders one or more of the modal frequency responses constant over the time aperture, a high resolution nonlinear frequency-comb method such as that proposed in Ref. [13] may allow for the relaxation of the range aperture requirements.

5.6 Acknowledgements

This chapter, in full, has been submitted for publication to The Journal of the Acoustical Society of America, 2005, with authors S. C. Walker, Philippe Roux, and W. A. Kuperman. Reprinted with permission from S. C. Walker, Philippe Roux,

and W. A. Kuperman, "Mode extraction from an accelerating narrow band source in shallow water," J. Acoust. Soc. Am., submitted for publication. Copyright 2005. Acoustical Society of America.

Bibliography

[1] W. A. Kuperman and F. Ingenito, "Spatial correlation of surface generated noise in a stratified ocean," J. Acoust. Soc. Am. **67**, 1988-1996, 1980.

[2] P. Hursky, W. S. Hodgkiss, and W. A. Kuperman, "Extracting modal structure from vertical array ambient noise data in shallow water," J. Acoust. Soc. Am. **98**, 2791 (1995).

[3] T. B. Neilsen and E. K. Westwood, "Extraction of acoustic normal mode depth functions using vertical line data," J. Acoust. Soc. Am. **111** (2), 748756 (2002).

[4] S. C. Walker, P. Roux, and W. A. Kuperman, "Data-based mode extraction with a partial water column spanning array," J. Acoust. Soc. Am. **118** (3), 1518-1525 (2005).

[5] Kenneth E. Hawker, "A normal mode theory of acoustic Doppler effects in the oceanic waveguide," J. Acoust. Soc. Am. **65** (3), 675681 (1979).

[6] Henrik Schmidt and W. A. Kuperman, "Spectral and modal representations of the Doppler-shifted field in ocean waveguides," J. Acoust. Soc. Am. **96**, 386 (1994).

[7] George V. Frisk, and James F. Lynch, "Shallow water waveguide characterization using the Hankel transform," J. Acoust. Soc. Am. **76** (1), 205-216 (1984).

[8] F. B. Jensen, W. A. Kuperman, M. B. Porter, and H. Schmidt, *Computational Ocean Acoustics*, (AIP New York, 1994).

[9] P. A. Baxley, "Matched-field replica model optimization and bottom property inversion in shallow water," Master's thesis, University of California, San Diego, 1997.

[10] P. Hursky, W. S. Hodgkiss, and W. A. Kuperman, "Matched field processing with data derived modes," J. Acoust. Soc. Am. **109**(4), 1355-1366 (2001).

[11] M. B. Porter, "The KRAKEN normal mode program," SACLANT Undersea Research Center, La Spezia, Italy, 1991.

[12] T. C. Yang, "A method of range and depth estimation by modal decomposition," J. Acoust. Soc. Am. **82** (5), 1736-1745 (1987).

[13] Philippe Roux, Didier Cassereau, and André Roux, "A high-resolution algorithm for wave number estimation using holographic array processing," J. Acoust. Soc. Am. **115**(4), 1059 (2004).

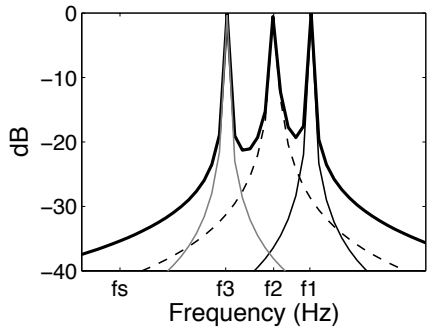

Figure 5.1: Schematic of the discrete modal frequency spectrum from a constant radial velocity cw source. This environment supports 3 propagating modes. The thin black line, the thin, dashed black line, and the thin gray line represent the Fourier transforms of the individual modal components. The thick black line is the Fourier transform resulting from a modal superposition. For a constant radial velocity source, the modal frequencies, indicated by $f1$, $f2$, and $f3$ (for modes 1, 2, and 3 respectively), are unambiguously discrete. The modes experience Doppler shifts of $fn = fs - \frac{k_n \beta}{2\pi}$. Here k_n is the mode n wavenumber, fn is the frequency of mode n, β is the ratio of the radial source velocity to the mode n group velocity, $\beta \equiv \frac{v_s}{v_{ng}}$, and fs is the source frequency. In this case the source is moving toward the sensor, $v_s < 0$.

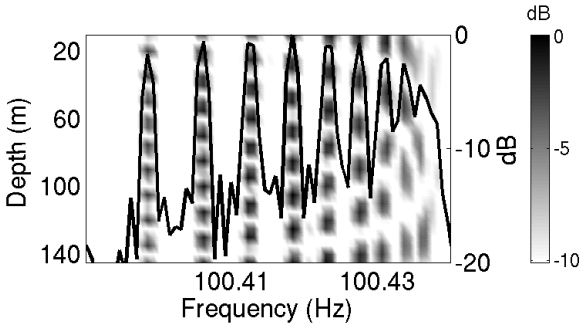

Figure 5.2: Fourier transform frequency response of a simulated VLA pressure field from the constant radial velocity cw source. The absolute value of the frequency domain pressure field as a function of depth is imaged in dB. The solid black line represents the frequency domain pressure field summed incoherently over depth in dB (right axis). The source ($fs = 100.17\ Hz$) is traveling toward the VLA at a constant velocity along an endfire trajectory.

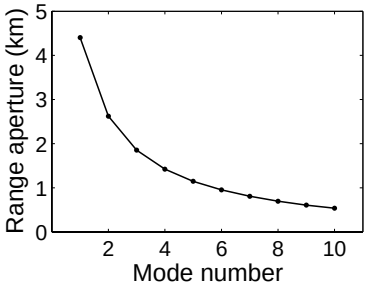

Figure 5.3: Minimum range aperture required to resolve adjacent modal frequencies. This figure corresponds to the simulation shown in Fig. 5.1.

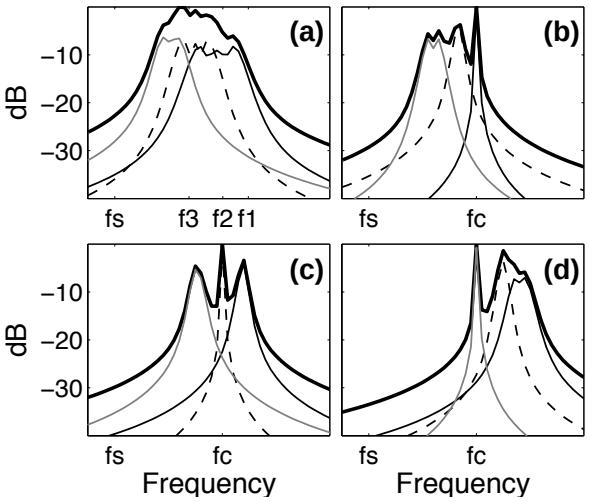

Figure 5.4: Schematic of the modal frequency spectrum from a radially accelerating cw source. The thin black line, the thin, dashed black line, and the thin gray line represent the Fourier transforms of modes 1, 2, and 3 respectively (each considered individually). The thick black line is the Fourier transform a superposition of the modes. (a) At the beginning of the source track, when the radial velocity of the source is the least, the modal frequencies, $f1$, $f2$, and $f3$, are the greatest. As the radial velocity of the source increases, the modal frequencies decrease, approaching the source frequency, fs, causing a "smearing" of the Fourier transform of the received source signal. By applying a transform to the received signal that compensates for the radial acceleration, it is possible to "unsmear" the Fourier frequency spectrum. In cases of extreme acceleration, this can only be done for one mode at a time. Panels (b), (c), and (d) show the effects of the compensation procedure. By properly scaling the compensation function it is possible to return each mode to the desired compensation frequency, fc.

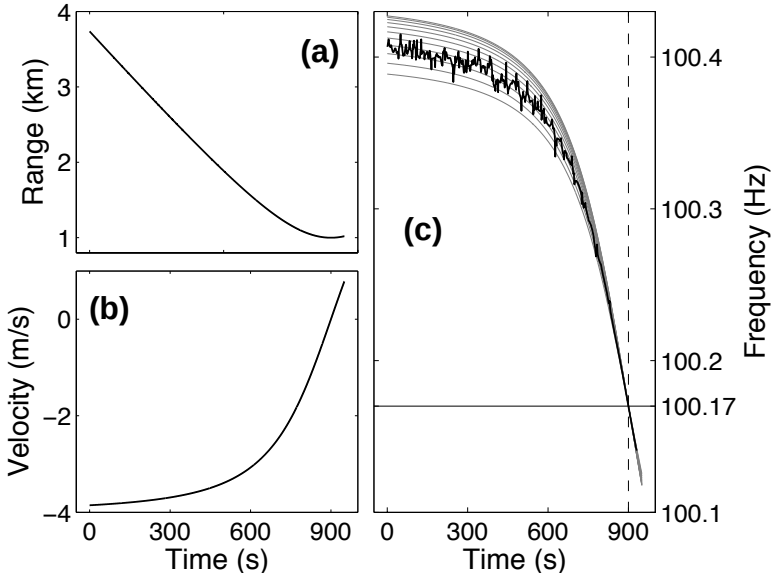

Figure 5.5: Time dependent range (a) and velocity (b) of nonendfire cw source used in simulation 2. The source is radially accelerating. (c) Frequency tracking algorithm results from radially accelerating cw source of simulation 2. The thick black line represents the output of the algorithm. The fine black lines indicate the expected frequencies of each propagating mode over the source trajectory. The dashed line marks the time of closest approach, and the solid medium black line marks the source frequency.

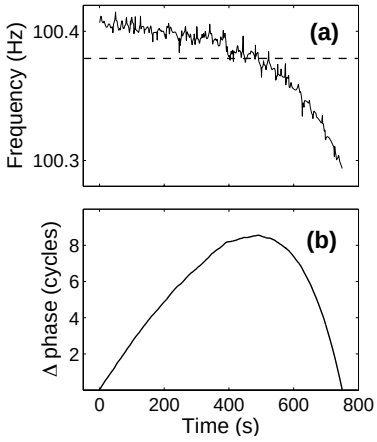

Figure 5.6: (a) Frequency tracking result for a simulated radially accelerating cw source. The solid curve is the frequency track result. The dashed line indicates the average frequency over the time aperture. (b) Time dependent phase deviation derived from the frequency tracking result shown in (a).

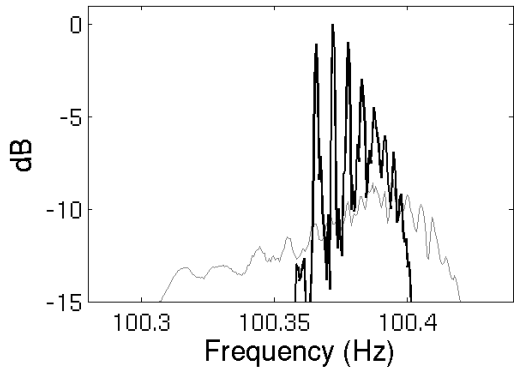

Figure 5.7: Compensated versus uncompensated simulated frequency spectrum from a simulated radially accelerating source. The gray line is the Fourier transform frequency response of the simulated pressure field summed incoherently over the elements of the VLA. The black line is the frequency response that results from applying a compensation to the time domain pressure field prior to applying the Fourier transformation. The compensation has transformed the field so that it resembles the field from a constant radial velocity source.

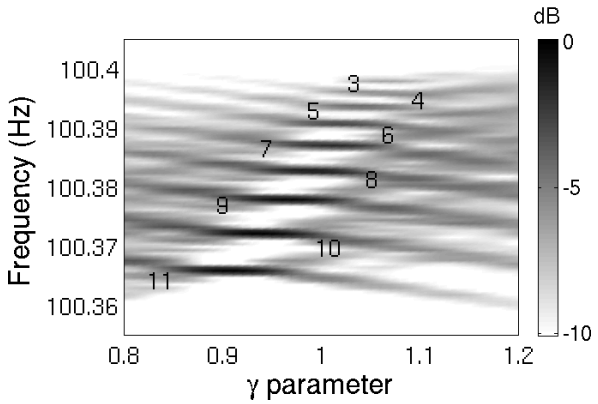

Figure 5.8: Fourier transform frequency response of the compensated VLA pressure field from the radially accelerating cw source of simulation 2 versus the compensation parameter, γ. The frequency response has been summed incoherently over depth. The dark regions indicate where a given mode is expected to be well resolved.

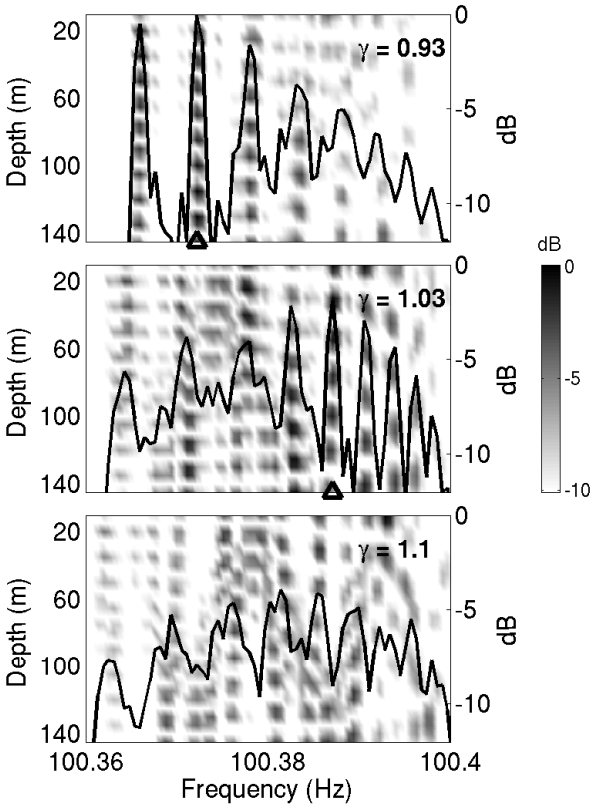

Figure 5.9: Fourier transform frequency response as a function of depth of the compensated VLA pressure field from the radially accelerating cw source. The results for 3 values of the compensation coefficient, γ, are shown. The solid black line represents the frequency response of the respective compensated pressure fields summed incoherently over depth in dB (right axis). As the compensation coefficient is increased, different modal frequencies are resolved. Mode 10 (triangle) is best resolved at $\gamma = 0.93$, while $\gamma = 1.03$ results in the best resolution for mode 7 (triangle). At $\gamma = 1.1$ no modes are well resolved.

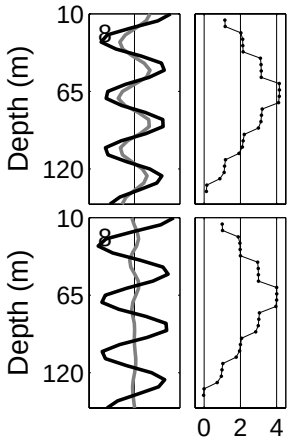

Figure 5.10: Extracted mode 8 from simulation 2 and its complex phase. The depth projection of the compensated pressure field at a given modal frequency is a product of the depth dependence of the mode and a complex phase. For a vertical, untilted array of sensors the complex phase should be constant over depth. The top-left panel shows the modal depth dependence at the mode 8 modal frequency. The top-right panel shows the complex phase at each array element in units of π. The phase has been "unwrapped" so that it can assume values outside the range $[-\pi, \pi]$. The staircase structure of steps of π indicates that the phase is constant at all depths. The bottom panels show a phase translation that results in the depth dependence being purely real.

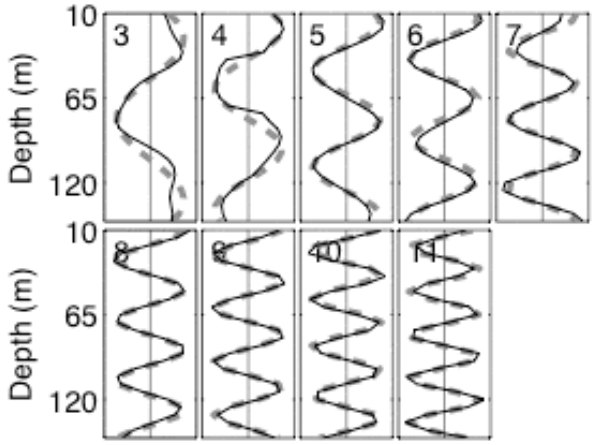

Figure 5.11: Mode extraction results from the compensated VLA pressure field from the radially accelerating cw source of simulation 2. The extracted modes (solid black lines) are compared to the theorectical modes (gray dashed lines). A different compensation factor was used for each modal extraction. The range aperture covered by the source was insufficient for extracting modes 1 through 4.

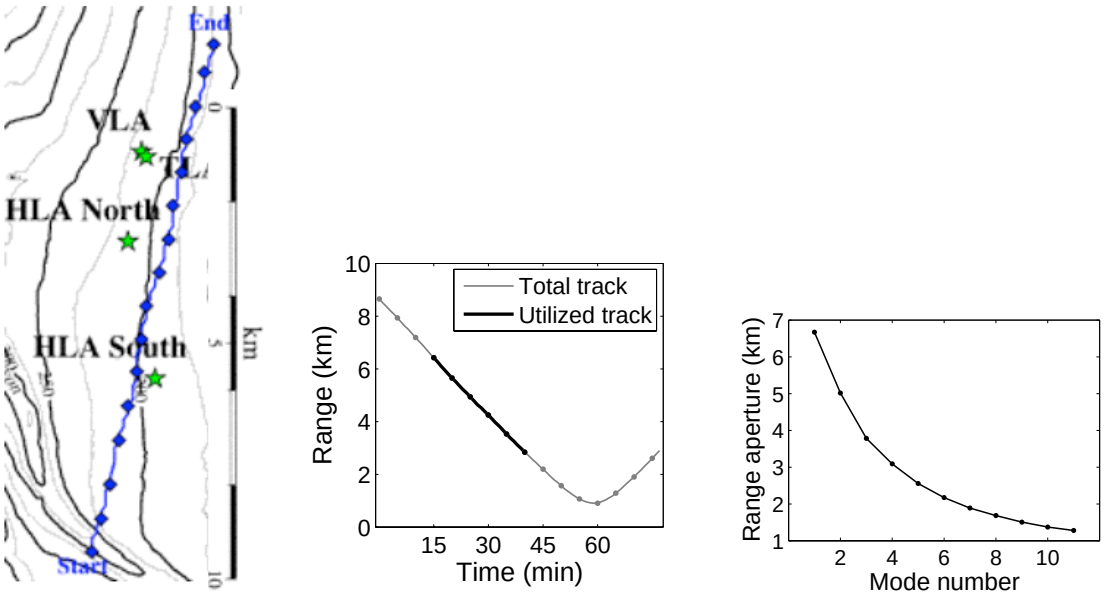

(a) (b) (c)

Figure 5.12: (a) Source track and bathymetry for the SWellEx 1996 experiment. The source moved along the trajectory indicated by the thick dotted line. The dots represent 5 minute intervals. The signal was recorded by the VLA. Each unbroken black line indicates an isobath. The source followed a 200 meter isobath. (b) Source range as a function of time. The approximate range covered by the source during time domain VLA pressure field used for mode extraction is indicated by the thick black line. Each dot represents 5 minutes. (c) Minimum range aperture required to resolve adjacent modal frequencies.

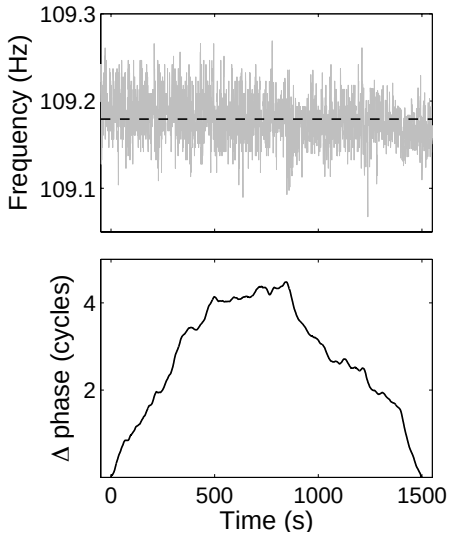

Figure 5.13: Frequency tracking algorithm result (top) and the resulting phase compensation function (bottom) for the SWellEx source. The thin gray line indicates the frequency tracking result. The thick black line is the phase compensation function. The dashed line marks the average frequency over the interval used by the compensation algorithm.

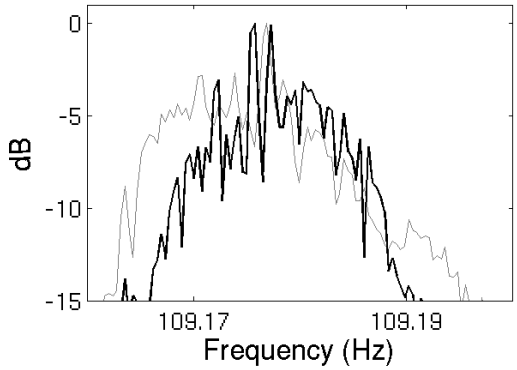

Figure 5.14: Compensated versus uncompensated experimental frequency spectrum from the SWellEx source data. The gray line is the Fourier transform frequency response of the measured pressure field summed incoherently over the elements of the VLA. The black line is the frequency response that results from applying a compensation to the time domain pressure field prior to applying the Fourier transformation.

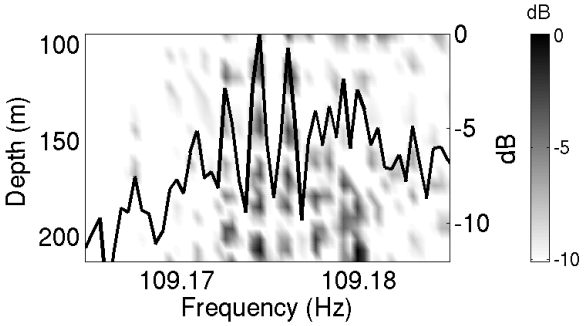

Figure 5.15: Fourier transform frequency response as a function of depth of the compensated VLA pressure field from the SWellEx source data. The results for a single value of the compensation coefficient is shown. The solid black line represents the frequency domain pressure field summed incoherently over depth in dB (right axis).

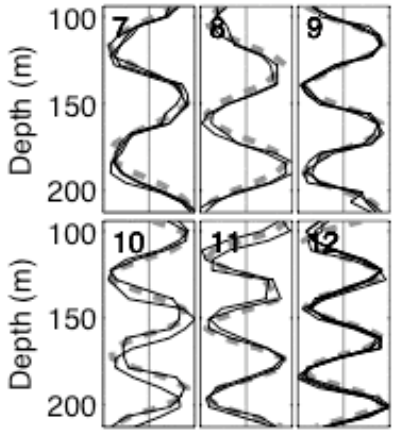

Figure 5.16: Mode extraction results from the compensated SWellEx source track VLA pressure field. The extracted modes (solid black lines) are compared to the modes modeled from knowledge of the environmental parameters (gray dashed lines). A different compensation factor was used for each modal extraction. The range aperture covered by the source was insufficient for extracting modes 1 through 6.

Chapter 6

An analysis of self-adaptive mode extraction from scattered fields

abstract

Previous chapters discuss methods for using the unscattered pressure field from a down range source sampled over a vertical line array (VLA) to extract the modal depth functions characterizing acoustic propagation in the shallow ocean. The VLA samples the field over depth while the down range source provides a means for sampling the field over range. Under the right conditions, reverberation from bottom scattering features can also be used to sample the field in range. This chapter assesses the potential for using the VLA as both a source and receiver to self-adaptively extract the modal depth functions from the reverberant field with no a-priori knowledge about the propagation medium. As a broadband signal propagates away from the VLA, inhomogeneities along the water/bottom interface scatter some of the field back toward the VLA, mimicking a moving source, providing a method for sampling a large range aperture. In constrast to the unscattered field, modal theory predicts a coupling between the outbound and inbound modal components of the reverberant field. Additionally, modal dispersion leads to ambiguities in time-to-range mapping of the received time domain field. These complications undermine the mode extraction process. A method for suppressing reverberant mode coupling

is introduced. Theory, simulation, and laboratory measurements are presented.

6.1 Introduction

The mode extraction methods discussed so far require active acoustic sources down range from the vertical line array (VLA). For example, experimental applications often deploy a dedicated source, while passive sonar applications might rely on passing sources of opportunity. One way to eliminate the need for down range sources would be to use bottom reverberation. The idea is similar to that proposed by in Ref. [1], where the authors develop a method for extracting the mode amplitudes from ambient noise generated by a sheet of uncorrelated sources (surface bubbles) extending over a large range aperture. In the reverberation case, randomly distributed inhomogeneities along the water/sediment boundary, serve as a sheet of uncorrelated scatterers extending over a large range aperture. In order to improve the signal-to-noise-ratio (SNR), the scattering features can be ensonified using the same VLA that samples the field. The concept is illustrated schematically in Fig. 6.1.

Whereas the acoustic field from active sources or ambient noise comprises only inward propagating components (from the perspective of the VLA), the reverberant field comprises both inward and outward propagating components, resulting in coupling between the inbound and outbound modal components. To illustrate the point, consider the case of a narrowband (monochromatic) field, where each modal component has a definite propagation angle. As demonstrated in Fig. 6.2, a given modal component is scattered in all directions, including the propagation angles of the other modes. In the broadband case, where each modal component travels as a group at a constant group velocity, the modal components disperse in both the outbound and inbound directions. The broadband case is illustrated schematically in Fig. 6.3. Panel (a) shows 3 outward propagating broadband modal components. As the components propagate out, they disperse so that each reaches a given scat-

tering feature at a different time. Panel (b) depicts the situation a short time after the slowest propagating mode has interacted with the scatterer. Each outbound component has been scattered into the complete spectrum of modal components which continue to disperse as they propagate back toward the VLA. One interesting consequence is that a mode m outbound component scattered into a mode n component arrives back on the array simultaneously with a mode n outbound component that scatters into a mode m component.

In the case of many scattering features distributed in range, the extended geometry of the scattering medium leads to increased duration of the measurable reverberated return. A half second duration pulse source signal, for example, may generate several seconds of measurable reverberation. In the absence of dispersion, assigning a range to a specific time of the measured return is straightforward,

$$r = \frac{c_w t_h}{2}$$

where c_w is the sound speed of the water and t_h is the time at which the return from a scatterer at range r arrives on the VLA. In the shallow ocean waveguide, however, mapping sampled signal time to range is more complicated. Due to dispersion, contributions from scatterers at different ranges arrive simultaneously on the VLA, resulting in an ambiguity in time-to-range mapping. Because the modal groups are dispersing over time, the ambiguity increases with sampled signal time.

Both the coupling of the inbound and outbound modal components and the ranging ambiguity complicate self-adaptive mode extraction applications. Section 3.2 discusses two strategies for using the singular value decomposition (SVD) to extract the modal amplitudes from the data generated cross spectral density matrix (CSDM). In one strategy, the CSDM is conditioned through averaging [1, 2], in the other, the modal components are isolated in the CSDM according to their frequency-wavenumber (f-k) response [3]. The remainder of this chapter is dedicated to demonstrating and analyzing the complications introduced to both mode extraction strategies. It turns out that by employing the entire array as an ensemble of simultaneous sources, it is possible to overcome the mode coupling complication.

Section 6.2 develops a theoretical foundation for understanding the complications associated with the reverberant pressure field in the context of modal theory. Three cases are considered: the point-source/point-scatterer field, the broadside-source/point-scatterer field, and the extended-scatterer field. The potential for mode extraction from the shot-to-shot averaged CSDM is addressed in Sec. 6.3. Section 6.4 considers the possibility of extracting the modal depth functions from the f-k dispersion response of the reverberant field, offering an experimental verification of mode coupling. Section 6.5 summarizes and discuses the results.

6.2 The reverberant pressure field

As a basis for understanding the complications associated with applying self-adaptive mode extraction methods to scattered fields, this section develops the reverberant pressure field in the context of modal theory.

6.2.1 The point-source/point-scatterer field

According to modal theory, the ω component of the reverberant pressure response measured at element q of the VLA due to a single scattering feature on the bottom at depth $z = D$ (D being the depth of the water/sediment interface) and range r from a source coincident with element q' of the array is written [4, 5]

$$\begin{aligned} \widetilde{P}_q^{q'}(r,\omega) &= \frac{e^{-i\pi/4}}{\sqrt{8\pi}\rho(z_s)} \sum_{m=1}^{N} \frac{\phi_m(z_{q'},\omega)\phi_m(D,\omega)}{\sqrt{k_m(\omega)r}} e^{-ik_m(\omega)r} W_{mn}(\omega)\widetilde{S}(\omega) \\ &\quad \times \frac{e^{-i\pi/4}}{\sqrt{8\pi}\rho(D)} \sum_{n=1}^{N} \frac{\phi_n(D,\omega)\phi_n(z_q,\omega)}{\sqrt{k_n(\omega)r}} e^{-ik_n(\omega)r} \end{aligned} \tag{6.1}$$

The notation for the pressure field adheres to the following index convention, $\widetilde{P}_q^{q'}(r,\omega) \equiv \widetilde{P}(\omega, z_q, z_{q'}, r)$. The subscripted q indicates that the reverberant field is discretely sampled at the element depths, $z = z_q$, so that for a Q element VLA, $\widetilde{P}_q^{q'}(r,\omega)$ is a Q component vector. The superscripted q' indicates that the response is unique to the choice of source depth of the scattering feature. The scattering coefficient, $W_{mn}(\omega)$,

relates how acoustic waves of a given frequency incident upon the scattering feature from one angle, θ_{in}, scatter into acoustic waves propagating at another angle, θ_{out}. Thus, the scattering parameter is a function of the incident and scattered angles as well as the frequency. This discrete form for the scattering coefficient, $W_{mn}(\omega) \equiv W(\theta_{in}, \theta_{out}, \omega)$, is particular to the case of far-field modal propagation where θ_{in} and θ_{out} are restricted to the a discrete set of modal propagation angles.

In addition to the incidence and scattering angles, a more general scattering model may include material and geometric parameters to account for scatterer properties such as shape, density, sound speed, attenuation, etc. Presupposing a knowledge of the scatterer properties, there are numerous methods for modeling the scattering coefficient. Acoustic scattering-theory is treated extensively in the literature (see [6] for a review). From the stand point of self-adaptivity, where the aim is to progress without any a-priori information about the environment, sophisticated modeling of the scattering coefficient is impossible. Rather, the scattering feature properties are lumped with the set of unknown environmental quantities, such as the sound speed profile and the sediment properties, which are embedded in the sampled fields. The highly simplified form of the scattering coefficient in Eq. (6.1) emphasizes the essential physics of modal scattering in the context of self-adaptivity.

For the sake of readability, the explicit dependence on frequency, ω, is omitted for the remainder of this chapter. It is useful to redefine the scattering constant to include the modal excitations along the bottom as well as the source excitation, $\widetilde{S}$,

$$\widehat{W}_{mn} \equiv \left(\frac{-i\phi_m(D)\phi_n(D)}{8\pi\rho(D)\sqrt{k_m}\sqrt{k_n}} \widetilde{S} \right) W_{mn}. \tag{6.2}$$

With an eye toward ocean applications deploying omnidirectional VLAs, scattering from all azimuthal directions is here considered. In this case, the pressure response is properly an integral over azimuth,

$$\widetilde{P}_q^{q'}(r) \rightarrow \int_0^{2\pi} d\phi P_q^{q'}(r)\chi(r,\phi), \tag{6.3}$$

where the distribution of scattering features is described by $\chi(r,\phi)$. In this form, $\widetilde{P}_q^{q'}(r)$ represents the pressure response on the VLA due scatterers distributed around

a ring at range r. Substitution of Eqs. (6.2) and (6.1) into Eq. (**??**) yields

$$\widetilde{P}_q^{q'}(r) = \frac{1}{\rho(z_{q'})} \sum_{m,n=1}^{N,N} \phi_m(z_{q'})\phi_n(z_q)\widehat{W}_{mn}\frac{e^{-i(k_m+k_n)r}}{r}\int_0^{2\pi} d\phi\chi(r,\phi). \tag{6.4}$$

In this form, the mode coupling between the outgoing and incoming modal components is clear. Not only are the mode amplitudes coupled, but more importantly, so are the modal wavenumbers.

6.2.2 The broadside-source/point-scatterer field

In applications where it is necessary to transmit alot of acoustic power into the medium, VLAs are sometimes used to generate broadside fields. The term broadside refers to the case where identical signals are emitted simultaneously by all the elements of the VLA. Because they are unifrom over depth, broadside transmissions strongly excite all the modes. Just as in the single element source case, the broadside reverberant field exhibits strong mode coupling between outbound and inbound modal components. However, by modulating, or shading, the broadside signal over the elements of the array, it is possible to suppress this coupling.

Consider first the reverberant broadside field modulated by an arbitrary shading function, $\Psi(z_{q'})$. Summing over the sources results in the depth shaded broadside reverberant pressure response,

$$\begin{aligned} \widetilde{P}_q(r) &\equiv \sum_{q'=1}^{Q} \Psi(z_{q'})\widetilde{P}_q^{q'}(r) \\ &= \sum_{m,n=1}^{N,N} \widehat{\Psi}_m\widehat{W}_{mn}\phi_n(z_q)\frac{e^{-i(k_m+k_n)r}}{r}\int_0^{2\pi} d\phi\chi(r,\phi), \end{aligned} \tag{6.5}$$

where $\widehat{\Psi}_m$ is the projection of the shading function over the modes,

$$\widehat{\Psi}_m \equiv \left(\sum_{q'=1}^{Q} \frac{\Psi(z_{q'})\phi_m(z_{q'})}{\rho(z_{q'})}\right). \tag{6.6}$$

Because the modes are approximately a complete set, any shading function can be

synthesized from the modal components (provided they are well sampled in depth),

$$\Psi(z_{q'}) = \sum_{m'=1}^{N} a_{m'}\phi_{m'}(z_{q'}). \tag{6.7}$$

In the case of a full spanning densely sampling VLA, $\widehat{\Psi}_m = a_m$ (see Eq. 3.3). Using a crude sound speed profile, it should be possible to generate an approximation to a given mode, $\Psi(z_{q'}) \approx \phi_\alpha(z_{q'})$, such that $|a_\alpha| \approx 1 \gg |a_m|$ $(m \neq \alpha)$, thereby suppressing modal coupling in the reverberant field,

$$\widetilde{P}_q(r) \approx \sum_{n=1}^{N} a_\alpha \widehat{W}_{\alpha n}\phi_n(z_q)\frac{e^{-i(k_m+k_n)r}}{r}\int_0^{2\pi} d\phi\chi(r,\phi). \tag{6.8}$$

Physically, because it is an invariant, a modal group excitation by the VLA propagates coherently in range, suffering only from intra-modal dispersion. Therefore, it ensonifies each scattering feature only once. Practically speaking, because mode 1 has no zeros, it is the best candidate for estimation.

Figure 6.4 offers a schematic demonstration. Panel (a) depicts a mode 1 excitation propagating in range. The net effect is equivalent to down range point-sources sounding off sequentially as the outbound field passes by. Because they are located along the bottom, each scattering feature produces a point-source field that excites all the modes which propagate back to the VLA (Panel (b)).

6.2.3 The extended-scatterer field

Generalizing Eq. (6.4) to the case of non-interacting scattering features distributed in range leads straightforwardly to the following expression for the sampled VLA pressure response due to a single point-source on the VLA at $z = z_{q'}$,

$$\begin{aligned} \widetilde{P}_q^{q'} &\equiv \int_0^\infty \widetilde{P}_q^{q'}(r) r dr \\ &= \frac{1}{\rho(z_{q'})}\sum_{m,n=1}^{N,N}\phi_m(z_{q'})\phi_n(z_q)\widehat{W}_{mn} \\ &\quad \times \int_0^\infty dr e^{-i(k_m+k_n)r}\int_0^{2\pi} d\phi\chi(r,\phi). \end{aligned} \tag{6.9}$$

The non-interaction assumption, equivalent to the Born approximation, is valid in the limit that the spatial dimensions of the scattering features are small compared to the dimensions of the waveguide. In the shallow ocean environments of interest, this is generally the case. For example, prototypical bottom scattering features in a $D = 100\ m$ depth waveguide might measure a half-meter in height by a meter or two in radial length with tens of meters separating the them. In this limit, it is valid to consider only single scattering.

Combining Eqs. (6.8) and (6.9), the mode α shaded broadside field for an extended-scatterering medium is

$$\widetilde{P}_q \approx \sum_{n=1}^{N} a_\alpha \widehat{W}_{\alpha n} \phi_n(z_q) \int_0^\infty dr e^{-i(k_m+k_n)r} \int_0^{2\pi} d\phi \chi(r,\phi). \tag{6.10}$$

6.2.4 Medium fluctuations and scatterer decorrelation

In a completely static propagation medium, repeated measurements of the acoustic field will be identical. However, though the ocean can be considered static on the small time scales of acoustic propagation over several kilometers, it is, nevertheless, a dynamic medium. In the case of coherent ocean acoustics applications requiring many data acquisition (to enhance SNR for example) it is necessary to account for ocean fluctuations. Though each acquisition, or shot, may require only a few seconds, the full regime of acquisitions can take minutes to hours.

Small fluctuations of the propagation medium result in small aberrations among the shot-to-shot fields. In terms of the reverberant field from multiple simultaneous scattering features, a medium fluctuation coefficient, $\sigma(r,\phi)$, is introduced to account for fluctuations of the medium. Incorporating the medium fluctuation coefficient into Eq. (6.9) gives

$$\begin{aligned} \widetilde{P}_q^{q'} &\approx \frac{1}{\rho(z_{q'})} \sum_{m,n=1}^{N,N} \phi_m(z_{q'}) \phi_n(z_q) \widehat{W}_{mn} \\ &\quad \times \int_0^\infty dr e^{-i(k_m+k_n)r} \int_0^{2\pi} d\phi \chi(r,\phi) \sigma(r,\phi). \end{aligned} \tag{6.11}$$

and similarly for the broadside field, $\widetilde{P}_q$. Physically, $\sigma(r,\phi)$ represents a distribution of fluctuation induced deviations in the shot-to-shot acoustic trajectories between the source, scattering features at (r,ϕ), and the VLA. For a stable medium (one that is fluctuating about a mean state), it is often valid to assume that the different scattering features decorrelate over many shots,

$$\langle\sigma(r,\phi)\sigma(r',\phi')\rangle \equiv \frac{1}{J}\sum_{j=1}^{J}\sigma(r,\phi)\sigma(r',\phi') = \delta(r-r')\delta(\phi-\phi'). \tag{6.12}$$

This procedure is heuristically equivalent to considering an ensemble of random scattering surfaces.

6.3 Mode extraction from the conditioned CSDM

This section discusses the prospect of self-adaptively extracting modal amplitudes using a CSDM conditioning strategy analagous to that of Sec. 3.2.3. Similarly to the CSDM conditioning method applied to ambient noise in Ref. [1], here the CSDM formed from the reverberant field sampled over the VLA is averaged over many acquisitions or snap shots. Experimentally, a snap shot consists of a time windowed measurement associated with an acoustic source event, in this case the VLA generated signal. As addressed in 6.2.4, fluctuations of the propagation medium over the duration of the acquisitions can lead to decorrelation of the scatterers. Here it is assumed that the scattering features are uncorrelated.

6.3.1 The point-source/extended-scatterer CSDM

In analogy to Sec. 3.2.3, the point-source/multiple-scatterer reverberant pressure response of Eq. (6.9) is used to generate the reverberant CSDM,

$$\mathbf{C_j} = [Cqq'']_j \equiv \left[\widetilde{P}_q^{q'}\widetilde{P}_{q''}^{q'*}\right]_j, \tag{6.13}$$

where the asterisk denotes complex conjugation. The subscripted j denotes that this is for a single snap shot. Assuming a uniform distribution of scattering features,

$\chi(r,\phi) \to \chi$, that decorrelate (see Eq. 6.12) over many acquisitions, the shot-to-shot averaged CSDM is

$$\begin{aligned}
\mathbf{C^{ss}} &\equiv \frac{1}{J}\sum_{j=1}^{J}\mathbf{C_j} = \frac{1}{J}\sum_{j=1}^{J}\left[\widetilde{P}_q^{q'}\widetilde{P}_{q''}^{q'*}\right]_j \qquad (6.14)\\
&\approx \left[\frac{\chi^2}{\rho^2(z_{q'})}\sum_{m,n,m',n'=1}^{N,N,N,N}\phi_m(z_{q'})\phi_n(z_q)\phi_{m'}(z_{q'})\phi_{n'}(z_{q''})\widehat{W}_{mn}\widehat{W}^*_{m'n'}\right.\\
&\quad \left.\times\int_0^\infty dr e^{-i(k_m+k_n)r}\int_0^\infty dr' e^{i(k_{m'}+k_{n'})r'}\int_0^{2\pi}d\phi\int_0^{2\pi}d\phi'\,\langle\sigma(r,\phi)\sigma(r',\phi')\rangle\right]\\
&\approx \left[\frac{\chi^2}{\rho^2(z_{q'})}\sum_{m,n,m',n'=1}^{N,N,N,N}\phi_m(z_{q'})\phi_n(z_q)\phi_{m'}(z_{q'})\phi_{n'}(z_{q''})\widehat{W}_{mn}\widehat{W}^*_{m'n'}\right.\\
&\quad \left.\times\int_0^\infty dr e^{-i(k_m+k_n-k_{m'}-k_{n'})r}\right]
\end{aligned}$$

Referring to the discussion in Secs. 3.2.2 and 3.2.3, as a result of mode coupling between the outbound and inbound modal components, it is not possible to establish a relation between a SVD of $\mathbf{C^{ss}}$ and the modal components, even in the case of a full-spanning VLA.

6.3.2 The broadside-source/extended-scatterer CSDM

Using Eq. (6.10) for a uniform distribution of scatterers that decorrelate over many acquisitions, the shot-to-shot averaged CSDM for a mode α shaded broadside source has the form

$$\begin{aligned}
\mathbf{C^{ss}} &= \frac{1}{J}\sum_{j=1}^{J}\left[\widetilde{P}_q\widetilde{P}^*_{q''}\right]_j\\
&\approx \left[\sum_{n,n'=1}^{N,N}a_\alpha^2\widehat{W}_{\alpha n}\widehat{W}^*_{\alpha n'}\phi_n(z_q)\phi_{n'}(z_{q''})\right. \qquad (6.15)\\
&\quad \left.\times\int_0^\infty dr e^{-i(k_n-k_{n'})r}\right].
\end{aligned}$$

In connection with the discussion of Sec. 3.2.3, the term in parentheses above approaches the delta function $\delta(k_n - k_{n'})$. As a result a relation can be established

between the SVD of $\mathbf{C^{ss}}$ and the modes (see Sec. 3.2.2),

$$C^{ss}_{qq''} \approx \sum_{n=1}^{N} |a_\alpha \widehat{W}_{\alpha n}|^2 \phi_n(z_q)\phi_n(z_{q''}). \tag{6.16}$$

This result is analogous to the ambient noise case cited in the introduction, [1], where the bottom scattering features serve as uncorrelated sources similarly to bubbles at the surface. However, because the scattering takes place along the bottom where all the modes are strongly excited, the reverberated energy will be equally distributed among the modes, resulting in singular value degeneracies. As shown in Sec. 3.2.3, such degeneracies limit the effectiveness of the SVD in extracting the modes. Furthermore, Eq. 6.16 neglects near-field contributions due to reverberation from scattering features close to the VLA. In the narrowband limit, there is no way to remove these contributions. Including the near-field complicates the relation between the SVD of $\mathbf{C^{ss}}$ and the modes.

6.4 The f-k reverberant pressure response and mode extraction

As demonstrated in the last section, the prospects for extracting the modal depth functions using the shot-to-shot averaged CSDM of the reverberant pressure response are not promising. Though progress can be made using a broadside source, singular value degeneracies lead to poor mode extraction results. Section 3.2.4 introduces a method for extracting modes over a partial-spanning VLA that overcomes the degeneracy limitations of the SVD. Fourier analysis yields the frequency-wavenumber response of the pressure field, revealing its f-k dispersion structure. Because the modal dispersion is discrete in the f-k domain, it is possible to isolate the modal components from one another and extract them separately, thereby eliminating singular value degeneracies. The aim is to apply this method to the reverberant field. However, the mode coupling issues and ranging ambiguities associated with the reverberant field complicate matters.

In order to generate the wavenumber structure, the VLA must sample an ensemble of individual point-source fields with each source being at the same depth, but at different ranges. By sampling each source field separately, it is possible to unambiguously assign ranges to the field contributions of each source. In the reverberation case, it is not possible to directly sample the fields from the scatterers individually because the scattering features are not removable. As mentioned in the introduction, modal dispersion complicates the time-to-range mapping of the received time domain reverberant field. Reverberant field time-to-range mapping is an active area of current research beyond the scope of this disussion. The remainder of this section is dedicated to addressing mode coupling in the reverberant field in the context of the f-k dispersion spectrum. In order to simplify the analysis, individual scatterers are used in order to remove the ranging ambiguity associated with the more complex problem of simultaneous scatterers.

6.4.1 Modal dispersion of the reverberant field: simulation and experiment

For this analysis, an ensemble of H point-source/point-scatterer reverberant pressure fields are sampled by the VLA. The ensemble comprises isolated scatterers distributed in range. To make a connection to the geometry of the experiment discussed later in this section, the point-scatterers are evenly distributed along a single azimuthal direction with (r_h, ϕ_0, D) being the location of the h^{th} scatterer. In analogy with Eq. (6.4), the reverberant point-source/point-scatterer pressure filed on the VLA due to a single scatterer at r_h is

$$\widetilde{P}_q^{q'}(r_h) = \frac{1}{\rho(z_{q'})} \sum_{m,n=1}^{N,N} \phi_m(z_{q'})\phi_n(z_q) \left(\frac{e^{-i(k_m+k_n)r_h}}{r_h} \right) \widehat{W}_{mn}. \tag{6.17}$$

Sampling the scattered fields individually eliminates the range ambiguity associated with sampling all the scatterers simultaneously. Consequently, it is possible to apply a discrete Fourier transform over range to reveal the f-k response of the extended-

scatterer field,

$$\begin{aligned}\widetilde{\widetilde{P}}_q^{q'}(k_{h'}) &= \int_0^{2\pi} d\phi\delta(\phi-\phi_0)\sum_{h=1}^{H} r_h \widetilde{P}_q^{q'}(r_h)e^{-ik_{h'}r_h} \qquad (6.18)\\ &= \frac{1}{\rho(z_{q'})}\sum_{m,n=1}^{N,N}\phi_m(z_{q'})\phi_n(z_q)\widehat{W}_{mn}\\ &\quad\times\left(\sum_{h=1}^{H} e^{-i(k_{h'}+k_m+k_n)r_h}\right).\end{aligned}$$

Here $k_{h'}$ is the discretely sampled wavenumber conjugate to range, r_h. The double tilde notation, $\widetilde{\widetilde{P}}$, denotes that the pressure field has been transformed over both time and range. In the infinite range aperture limit, $\Delta r \equiv r_H - r_1 \rightarrow \infty$, the term in parentheses approaches a delta function, $\delta(k_{h'}+k_m+k_n)$, defining the dispersion characteristics of the reverberant field in the infinite resolution limit. That is, the coupled modal components manifest at frequency dependent wavenumbers in the f-k domain defined by the curves $k_{h'} = -(k_m + k_n)$.

This result is verified experimentally. Figure 6.5(a) shows the f-k dispersion spectrum of the extended-scatterer VLA pressure field synthesized from an ensemble of individual point-source/point-scatterer fields. The scattering features were evenly distributed along the bottom at 2 mm intervals over a range aperture of 600 mm. One of the array elements was used as the source. For the purposes of comparison, the reverberant field result is accompanied in Fig. 6.5(b) by an experimental dispersion spectrum generated from an ensemble of unscattered point-source fields. The sources were distributed along water/sediment interface in the same manner as the scattering features of the reverberant case. Both experiments were conducted in a controlled laboratory setting under similar conditions in nearly identical waveguides.

In the unscattered case (Fig. 6.5(b)) the modal components (enumerated dark curved regions) are easily identifiable, with the f-k response exhibiting the characteristic modal dispersion, $k = -k_m$. In both cases, a wavenumber transform has been applied to the f-k response in order to facilitate identification of the dispersion structure and mode extraction. Because the modal components are so clearly

defined and isolated from one another, it is possible to extract modes from the f-k response.

Returning to Fig. 6.5(a), the f-k response of the reverberant field exhibits much more complexity than that of the unscattered f-k response. Coupling of the inbound and outbound modal components leads to inter-modal structure in the reverberant field f-k dispersion, $k = -(k_m + k_n)$. The added structure undermines the mode extraction process. As a result, it is not possible to extract modes from the reverberant f-k response arising from a point-source.

A possible solution can be found in the broasside reverberant field. Discrete Fourier transforming the individually sampled mode α shaded broadside/point-source fields over range yields the f-k response of the broadside/extended-scatterer field,

$$\begin{aligned} \widetilde{\widetilde{P}}_q(k_{h'}) &= \int_0^{2\pi} d\phi \delta(\phi - \phi_0) \sum_{h=1}^{H} r_h \widetilde{P}_q^{q'}(r_h) e^{-ik_{h'} r_h} \\ &\approx \sum_{n=1}^{N} \widehat{W}_{\alpha n} \phi_n(z_q) \left(\sum_{h=1}^{H} e^{-i(k_{h'} + k_\alpha + k_n) r_h} \right) \end{aligned} \tag{6.19}$$

In the infinite range aperture limit, the dispersion structure of the shaded broadside reverberant field is governed by the relation $k_{h'} = -(k_m + k_\alpha)$ for the location of the modal contributions. Because α is constant, the dispersion spectrum is merely offset in wavenumber.

Figure 6.6 shows a comparison between point-source and shaded broadside-source simulation results. Figure 6.6(a) shows the reverberant VLA field due to a point source in a Pekeris waveguide. As expected, the point-source f-k response is complicated by reverberant mode coupling. The broadside response in Fig. 6.6(b) has been shaded using mode 1 from a pressure-release waveguide as an approximation to the true Pekeris mode 1. Even using an approximation to mode 1 leads to strong suppression of the coupled mode inter-modal components. Small errors due to the approximation start to become evident among the higher order modal components. Importantly, modes can be extracted from the resulting broadside-source

f-k response.

6.5 Summary and discussion

A study of the reverberant pressure field sampled over a vertical line array (VLA) has been presented. Analytic expressions for the reverberant pressure field between bottom scattering features and the VLA are derived from modal theory for several source/scatterer geometries: point-source/point-scatterer, point-source/extended-scatterer, and broadside-source/extended scatterer. The reverberant pressure field is more complicated than the direct, unscattered field. Most notably, dispersion in the reverberant field leads to coupling between the inbound and outbound modal components, particularly in the case of a point-source field. Additionally, the inability to isolate field contributions from individual scattering features leads to an ambiguous time-to-range mapping of the sampled field.

The potential for extracting the modal depth functions from the reverberant field using a VLA has been assessed. Two mode extraction strategies, based on applying a singular value decomposition (SVD) to the cross spectral density matrix (CSDM) of the sampled reverberant VLA field, are considered. The first involves shot-to-shot averaging of the reverberant field over the VLA to decorrelate the scattering features in the CSDM. The second requires knowledge of the ranges of the scattering features to construct the frequency-wavenumber (f-k) dispersion spectrum. Because the modal dispersion spectrum is characteristically discrete, the modal components can be isolated in the CSDM. In both cases, coupling of the inbound and outbound modal components undermines the mode extraction process.

It is shown that sending a broadside signal shaded by one of the modal depth functions suppresses mode coupling. Applying shot-to-shot CSDM conditioning in combination with a mode shaded broadside-source leads to an isomorphism between the SVD of the CSDM and the modal depth functions. However, because the scatterers are distributed along the bottom, the acoustic power is evenly distributed

among the modal components. This equipartition of energy among the modal components leads to degeneracies to singular values that undermine the mode extraction process.

A frequency-wavenumber (f-k) dispersion analysis has been used to experimentally verify mode coupling in the reverberant field. In order to overcome the time-to-range ambiguity of the reverberant field, the extended-scatterer f-k response was synthesized from an ensemble of point-source/point-scatterer fields. The resulting f-k response is consistent with the expected coupled mode dispersion. Modes cannot be extracted from the coupled mode reverberant f-k response. However, simulation results demonstrate that it is possible to suppress reverberant mode coupling by using a broadside-source as opposed to a point-source, suggesting a possible strategy to be incorporated into any future mode extraction methods. This strategy may be extendable to weakly range-dependent environments where low order modal components exhibit coherence over long ranges.

These results represent an important preliminary step in the direction of a solution to the problem of extracting mode depth functions from the reverberant field. This work demonstrates an effective method for suppressing mode coupling. Future work focused on overcoming the ranging ambiguities inherent in reverberant fields is called for.

6.6 Acknowledgements

This chapter, in part, will be submitted for publication with authors S. C. Walker, Philippe Roux, and W. A. Kuperman.

Bibliography

[1] W. A. Kuperman and F. Ingenito, "Spatial correlation of surface generated noise in a stratified ocean," J. Acoust. Soc. Am. **67**, 1988-1996 (1980).

[2] T. B. Neilsen and E. K. Westwood, "Extraction of acoustic normal mode depth functions using vertical line data," J. Acoust. Soc. Am. **111** (2), 748756 (2002).

[3] S. C. Walker, P. Roux, and W. A. Kuperman, "Data-based mode extraction with a partial water column spanning array," J. Acoust. Soc. Am. **118** (3), 1518-1525 (2005).

[4] H. P. Bucker and Halcyon E. Morris, "Normal-mode reverberation in channels or ducts," J. Acoust. Soc. Am. **44**, 827 (1968).

[5] Dale D. Ellis, "A shallow-water normal mode reverberation model," J. Acoust. Soc. Am. **97**, 2804 (1995).

[6] J. A. Ogilvy, "Wave scattering from rough surfaces," Rep. Prog. Phys. **50**, 1553-1608 (1987).

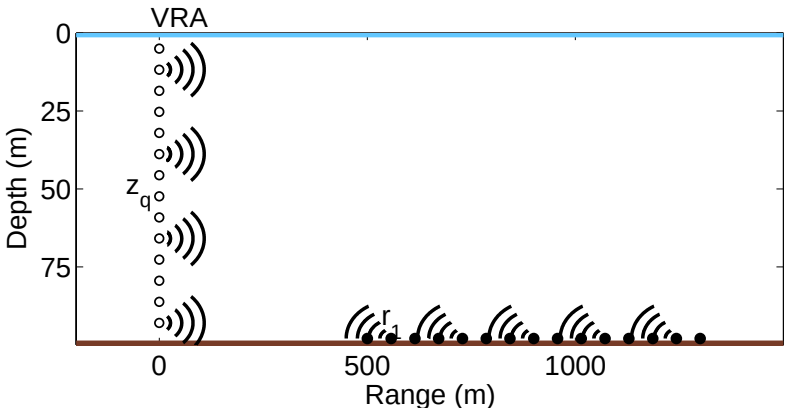

Figure 6.1: Experimental set up. The acoustic field originating from one or more elements (open circles) of a VLA (indicated as VRA on the figure) ensonifies scattering features (closed cirlces) along the water/sediment interface. The resulting reverberation is sampled by all the elements of the VLA.

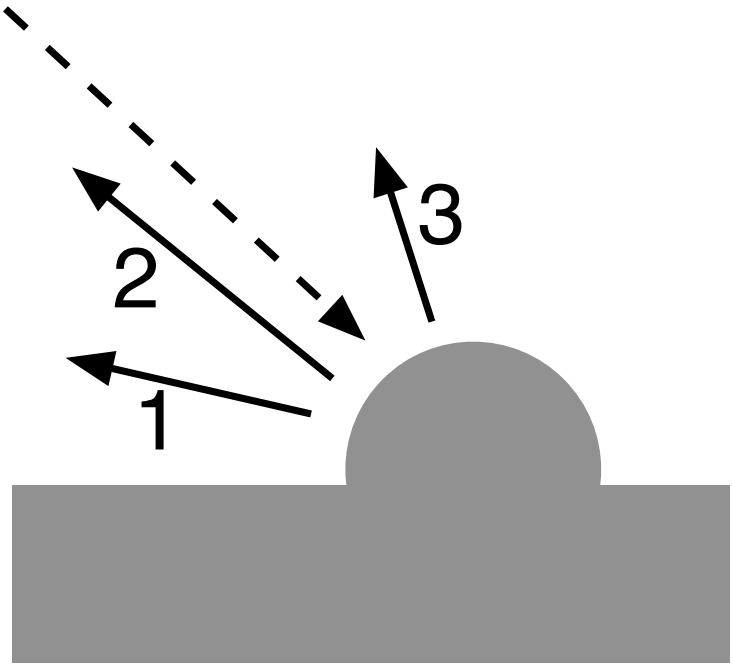

Figure 6.2: Narrowband scattering mode coupling schematic. Each outbound modal component (dashed arrow) of the acoustic field incident upon a scattering feature is scattered into the full spectrum of modal angles in the inbound field (enumerated solid arrows).

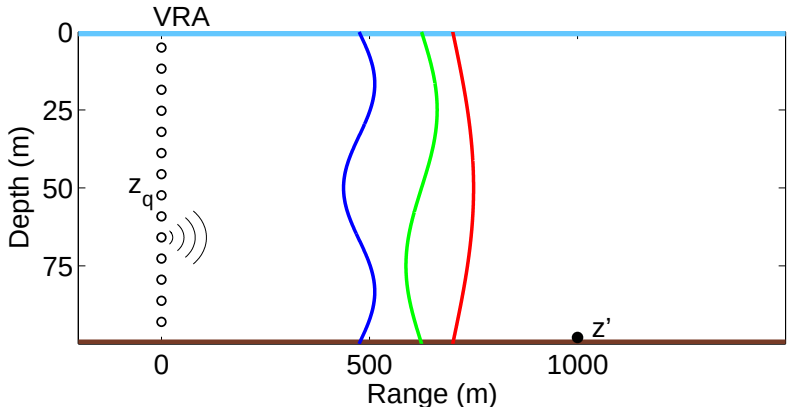

(a)

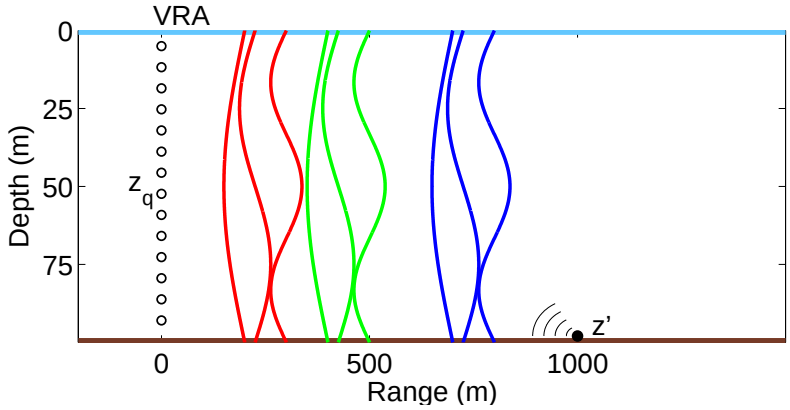

(b)

Figure 6.3: Broadband reverberant mode coupling schematic. (a) Each dispersive modal group component (gray curves) of the outbound field is (b) scattered into the spectrum of modal group components. Inbound components from scatterers at different ranges can arrive simultaneously on the VLA (indicated as VRA).

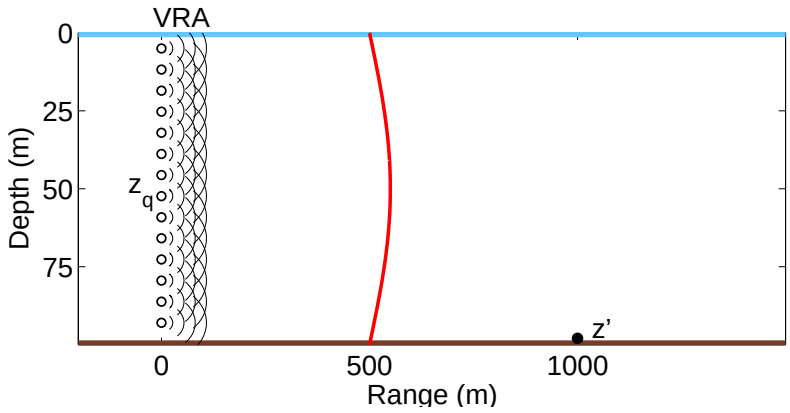

(a)

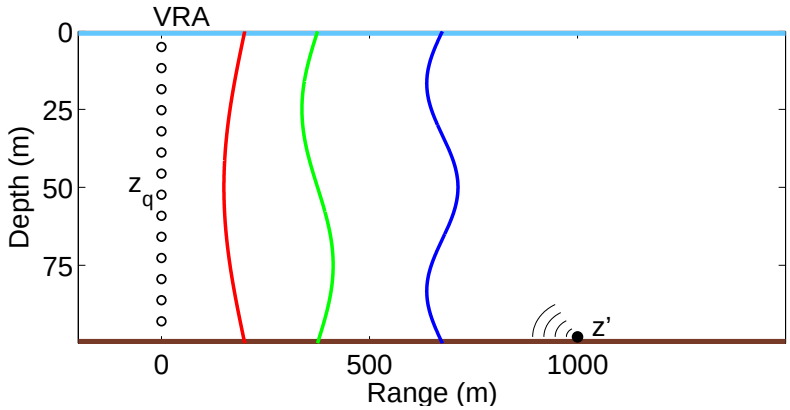

(b)

Figure 6.4: Broadband mode 1 shaded broadside-source schematic. (a) Mode 1 (gray curve) generated by the full array propagates outward coherently, illuminating each scatterer (solid circle) only once. (b) As a result, the inbound field does not suffer from reverberant mode coupling. The VLA is represent as VRA.

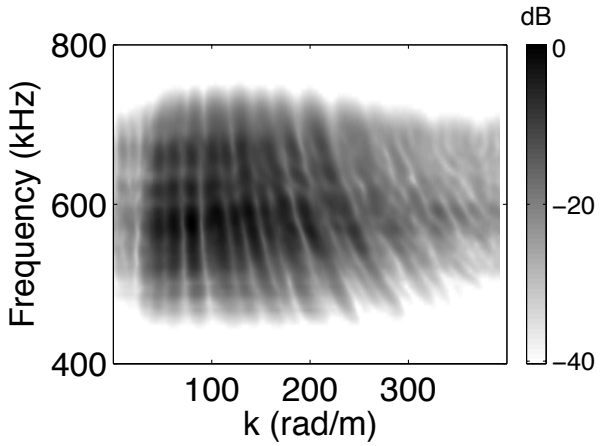

(a)

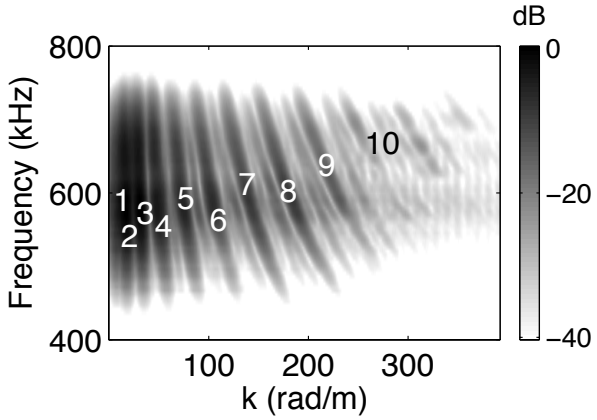

(b)

Figure 6.5: Comparison of experimental depth averaged modulus f-k responses. (a) The f-k response of the point-source reverberant field from down range scatterers exhibits inter-modal structure consistent with coupling between the outbound and inbound fields. (b) For comparison, the f-k response synthesized from unscattered pressure fields sampled from down range sources exhibits the desired uncoupled modal dispersion. The dark curved regions are the modal components. The modal components are enumerated for clarity. Both experiments were conducted in similar propagation media.

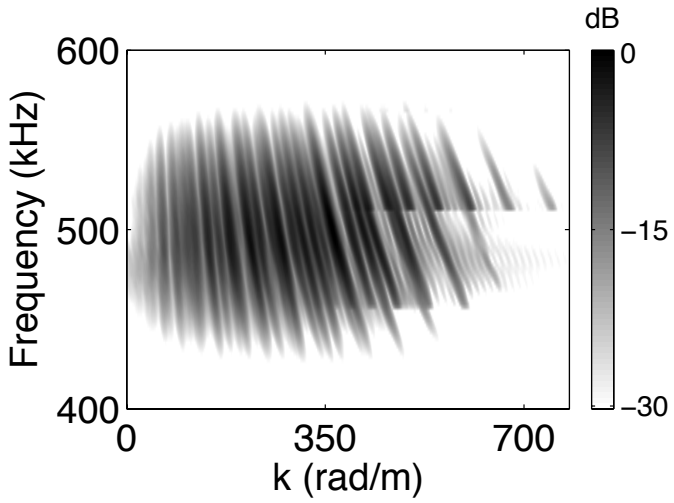

(a)

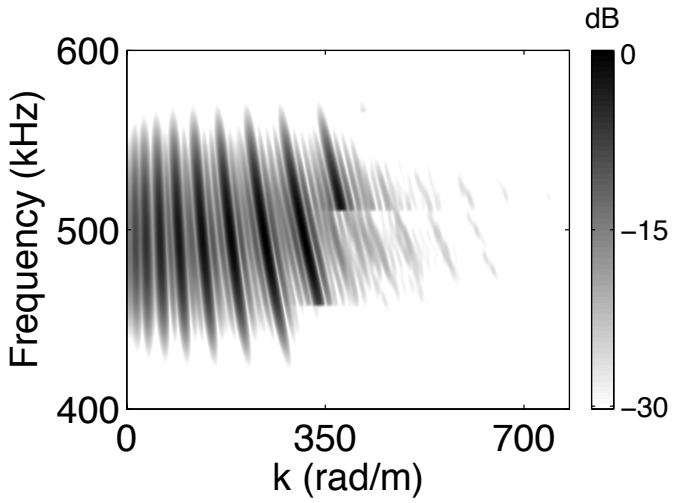

(b)

Figure 6.6: Comparison of simulated depth averaged modulus f-k responses. (a) The f-k response of the reverberant field due to a point-source excitation at the VLA exhibits reverberant mode coupling. (b) By comparison, the f-k response of the reverberant field due to a shaded broadside-source excitation at the VLA exhibits suppressed reverberant mode coupling. The broadside excitation was shaded with an approximation to mode 1.

Appendix A

Laboratory experimental set up

A.1 Introduction

All laboratory experiments referenced in this thesis were conducted in the the Ultrasonic Waveguide Laboratory of the Marine Physical Laboratories at the Scripps Institution of Oceanography in La Jolla, CA. This section describes the basic laboratory set up and implementation that are the foundation of the referenced laboratory experiments.

A.2 Experimental set up

In the laboratory set up, ultrasonic piezo-electric transducer devices are used to generate and sample coherent acoustic fields in a tri-layer (air, water, sediment) waveguide assembled in a plexi-glass water tank (Fig. A.1). The transducer devices or elements are affixed to precision controlled motors capable of moving the elements along 3 axes. The motors are supported by aluminum scaffolding. Depending on whether they are transmitting or receiveing, the transducer elements are connected to either a function generator (for generating signals) or an oscilloscope (for sampling signals). The function generator, the oscilloscope, and the motors are controlled remotely by a computer. The waveform, motor movement,

and firing commands, generated in Matlab®, are relayed to the the devices via a general purpose instrument bus (GPIB) protocol interface allowing automation of the experiments. Because the experiments typically involve intensive sampling of the medium, the ability to automate is indispensable.

The experimental set up is designed to model shallow ocean acoustic propagation at small scales under controlled conditions. The experimental dimensions are scaled to maintain the ratios between relevant extensive properties of working range (R), water depth (D), and the acoustic wavelength in the water (λ_w) that typify far-field shallow ocean applications,

$$\left(\frac{D}{\lambda_w}, \quad \frac{R}{D}\right)_{lab} \approx \left(\frac{D}{\lambda_w}, \quad \frac{R}{D}\right)_{ocean}, \tag{A.1}$$

where the working range is generally much greater than the water depth which in turn is much greater than the acoustic wavelength, $R \gg D \gg \lambda_w$. The shallow ocean application regime of interest is characterized by acoustic propagation in hundreds of meters of water over a working range of several kilometers at sub-kHz and kHz frequencies,

$$\left(\frac{R}{D}\right)_{ocean} > 10, \quad \left(\frac{D}{\lambda_w}\right)_{ocean} > 5. \tag{A.2}$$

Due to the dimensions of the tank, the working range of the waveguide is limited to $R = 1\ m$, constraining the working water depth to a few centimeters or less and the acoustic wavelength to a few millimeters or less.

A.2.1 The water tank

The water tank, constructed of 1/2 inch thick reinforced plexi-glass, is designed to contain up to 1 m^3 of fresh water. To facilitate manipulation of the instruments, the tank is open at the top, exposing a large surface area of the water to the ambient air. One drawback of this design is that it does not prevent evaporation, which can be a problem over long duration experiments ($12 - 24\ hrs$). Evaporative water level changes of over 1 mm have been observed over a period of 24 hrs. Such high evaporation rates are not negligible for experiments where the acoustic wavelength

is a few millimeters or less and the water depth is a few centimeters. To overcome evaporative losses, water is continually added to the tank at a rate exceeding the evaporation rate. The the tank is equipped with an adjustable water outlet set at the desired water level to remove the excess water. As a result, the water level can be maintained at a stable depth for as long as necessary. The water is gently circulated and filtered. The circulation provides a mechanism for mixing the water well enough to dissipate thermal inhomogeneities which affect the sound speed profile of the water.

A.2.2 Waveguide properties

After setting the water depth of the tank, the sediment is placed at the desired working depth. The laboratory is equipped to use various types of sediments: hardened steel, plexi-glass, sand, clay, glass beads, etc. The steel and plexi-glass are in the form of rectangular rods, while the sand, clay, and beads are contained in an elongated, open rectangular box. It is assumed that the rods and the box are thick enough that any acoustic reflections from the bottom edge is negligible (the top edge being the water/sediment interface). At the ultrasonic frequencies used in the experiment, the rods are about 30 $S\lambda_b$ in thickness whereas the sediment containing box is about 50 λ_b deep.

The sediment rests, at either end, atop a pair of finely-threaded adjustable stands. For experiments requiring a range-independent waveguide medium, the stands are adjusted so as to render the top surface of the sediment parallel to the surface of the water. The apparatus is situated in the center of the water tank to minimize the effect of reflections from the edges of the tank. Due to the dispersion of the waveguide, it is possible for the edge reflection to arrive simultaneously with the later arrivals at the extremities of range separation. The tank is wide enough and long enough that this is not an issue.

Due to the large impedance mismatch at the air/water interface and the homogeneity of the water and sediment layers, the waveguide is well modeled as a Pekeris

waveguide. A Pekeris waveguide is an idelized waveguide in which the bottom is represented as an infinite fluid half-space of finite impedance and a pressure reslease condition at the air/water interface. The Pekeris waveguide idealization is useful because it leads to an analytic model for acoustic propagation. However, it must be noted that the impedances of the various sediments are only approximately known, so it is not possible to forward model the acoustic field in the tank. On the other hand, applying the Pekeris waveguide assumption, it is possible to use the sampled fields to invert for the impedances of the various sediments, an experiment that is currently under way.

A.2.3 Source signal, transducers, and hydrophone

As mentioned, the small scales of the laboratory waveguide require an acoustic wavelength of a few millimeters or less. For a water sound speed, $c_w = 1500\ m/s$, the acoustic wavelength of a $f = 1.5\ MHz$ signal is $\lambda_w \equiv c_w/f = 1\ mm$. The laboratory is equipped with various ultrasonic piezo-electric transducers each rated to perform optimally over various frequency spectrum regions. The lab is equipped to perform experiments at frequencies ranging from 200 kHz to $3.5MHz$. The transducer elements are embedded in an epoxy material and packaged in dual element devices. Figure A.2 shows an example of such a device (left-most device).

Each element, being much longer in horizontal dimension than vertical dimension, is designed to transmit a broadband acoustic beam, thereby reducing the radial loss due to cylindrical spreading. Due to their directionality, the transducer package must be oriented in a specific manner with respect to the waveguide. In Fig. A.2 the elements are at opposite ends (top and bottom) of the white face of the transducer package oriented parallel to the top and bottom edges of the device. Although the transducers are capable of both emission and reception, due to their directionality, they are generally not used for reception. Instead, the more sensitive omni-directional hydrophone receiver, pictured on the right in Fig. A.2, is used. It is a dedicated piezo-electric listening device. Because of its small size, it is also more

maneuverable.

All laboratory experiments discussed in this thesis involve both range and depth sampling of the waveguide. To accomplish this, the transducer and hydrophone are affixed, via fiberglass rods, to remotely controlled motors. Supported by aluminum scaffolding, two of the motors are oriented to move vertically and one horizontally. Typically, the transducer package is fixed in range and moved vertically at one end of the waveguide. The hydrophone is moved both vertically and horizontally along the waveguide. The experimental geometry is displayed in Figs. A.1 and A.3. The motors are designed to translate to within micrometer precision, easily meeting the $\lambda_w/2$ sampling requirements discussed in 2.2.2. Both the oscilloscope and function generator are capable of Gb/s sampling rates.

A.2.4 Experimental limitations

While the relative range positions of samples are known to micrometer accuracy, due to the ambiguity involved with measuring the distance between the motor and the transducer package, the absolute range is ambiguous to $1 - 2\ mm$. More crucially, water meniscus effects complicate the determination of absolute depth of the elements. Indeed, the meniscus at the air/water interface along surface of the flat-edged transducer package can measure $3\ mm$. Additionally, the location of the elements in the packages themselves are also not precisely known. As a result, the absolute depths of the transducer elements is always considered unknown, with only their relative spacings taken as known quantities. Whatsmore, the sound speed profile of the water and the impedance of the sediment are also considered unknown. This situation is not unlike that encountered in at sea applications. The fact that such a high level of experimental progress can be made in the tank is a testament to the utility and power of the self adaptive methods developed in this work.

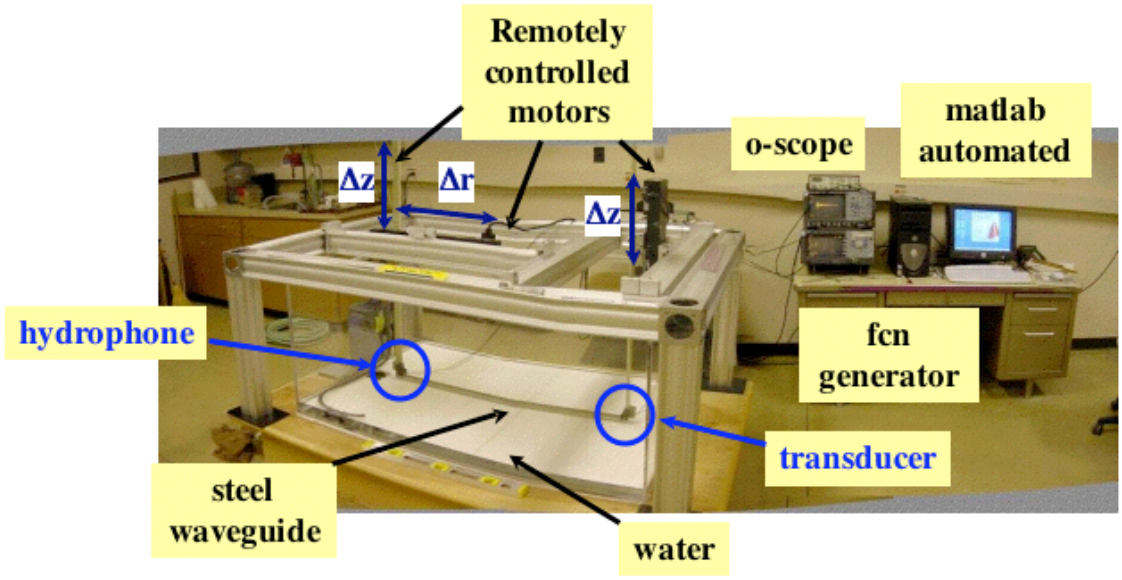

Figure A.1: Experimental set up. A tri-layer waveguide comprising air, water, and a sediment material is contained in a plexi-glass tank. Acoustic transducers, manipulated by remotely controlled motors, ensonify the waveguide and measure its acoustic properties. The length and water depth of the waveguide are variable. The acoustic signals are generated by a programmable electronic waveform generator and recorded with an oscilloscope. The process is automated by computer.

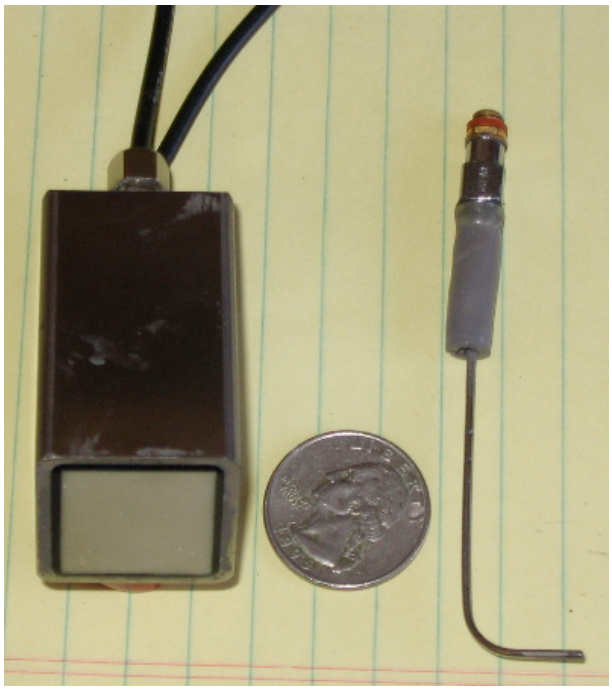

Figure A.2: Close up of experimental ultrasonic tranducer package and hydrophone. On the left is a piezo-electric acoustic transducer package. The package contains a pair of directional transducer elements. On the right is a dedicated omni-directional piezo-electric hydrophone.

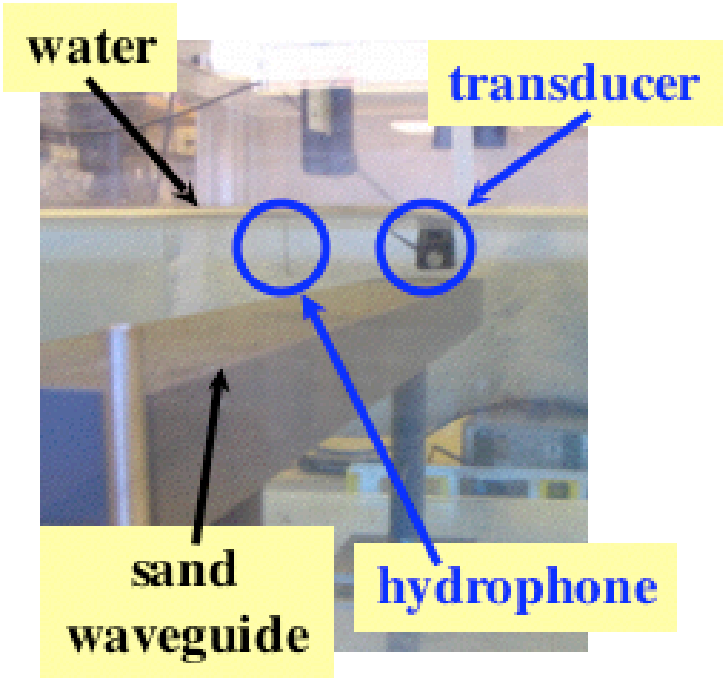

Figure A.3: Close up of waveguide. The transducer package and hydrophone, suspended by rods from motors, can be seen over a sand substrate. The sand is contained in a rectangular box atop adjustable stands.